THE MEGAMASER COSMOLOGY PROJECT: GEOMETRIC DISTANCES TO MEGAMASER GALAXIES AND ACCURATE MASSES OF SUPERMASSIVE BLACK HOLES AT THEIR CENTERS

Cheng-Yu Kuo
Charlottesville, Virginia

B.S., Physics, National Taiwan University, 2000
M.S., Astronomy, University of Virginia, 2007

A Dissertation Presented to the Graduate Faculty
of the University of Virginia in Candidacy for the Degree of
Doctor of Philosophy

Department of Astronomy

University of Virginia
August, 2011

James A. Braatz

Fred K. Y. Lo

Mark Whittle

Phil Arras

E. Craig Dukes

Mark J. Reid

Abstract

To constrain models of dark energy, the best complement to observations of the Cosmic Microwave Background is a precise measurement of the Hubble constant. The H_2O megamaser method can measure direct angular-diameter distances to galaxies in the Hubble flow, and thereby provides an opportunity to determine the Hubble constant independent of the Extragalactic Distance Ladder. In this thesis we present sensitive VLBI and single-dish observations of the megamasers in NGC 6264 and NGC 6323 and measure their distances using the megamaser method. This is the first time the method has been applied to galaxies beyond 100 Mpc. For NGC 6264 we developed an ensemble approach that fits the systemic masers with a multi-ring model, and we determine a distance of 150.5±33.6 Mpc (22% accuracy). We also apply a Bayesian technique that models the maser distribution as a warped disk and allows for eccentric orbits, and obtain a distance of 152.3±16.2 Mpc (10.6%). The corresponding H_0 is 65.8±7.2 km s^{-1} Mpc^{-1}. The best fit model from the Bayesian technique has a slight warp and a small eccentricity ($e \sim 0.06$), but this substructure has only a minor effect on the distance determination. For NGC 6323, although we made the most sensitive maser map ever observed, we do not obtain a comparably precise distance measurement because of the extremely low flux densities of the systemic masers. Nonetheless, the work on this galaxy helped develop a new self-calibration technique that enables efficient imaging of distant megamaser disks. In addition to the observations of these two galaxies, we also present sensitive VLBI images of four other megamaser galaxies, plus a seventh previously published, from which we determine accurate masses of the supermassive BHs at their nuclei. The BH masses are all within a factor of 3 of $2.2 \times 10^7 M_\odot$ and the accuracy of each is primarily limited by the uncertainty in the Hubble constant. These accurate BH masses contribute to the observational basis for testing the $M - \sigma_\star$ relation at the low-mass end.

Acknowledgements

I feel deeply grateful to the University of Virginia for providing the wonderful learning environment and abundant resources. The learning and life experiences here are unforgetable and had a profound impact on my thoughts, life, and mind. With all the great people and environment in Charlottesville, I think I have had significant growths in many aspect of my life, including science and spirituality, in the past six years. These six years have been my richest and happiest time in my life.

I first want to thank all the faculty members and my fellow graduate students in the astronomy department. The warm atmosphere in the department let me feel that the astronomy department is just like a big family, even though I am an international student coming from a different country. I often viewed my fellow graduate students just as my brothers and sisters, especially those who are close in entrance years. I learned greatly from them and I will never forget their warmness and kindness.

In the aspect of scientific research, I thank Dr. Fred Lo greatly for introducing me to work on the Megamaser Cosmology Project (MCP). Although this project is quite challenging to me, this is the best scientific project I have ever worked on so far. The richness and depths of this project have trained me to become a real scientist who can start to do independent research with all the great tools and knowledge learned from this project. I couldn't benefit so much without all the great scientists in the MCP team and at the NRAO, including my primary advisor Jim Braatz, Dr. Fred Lo, Jim Condon, Mark Reid, Christian Henkel, Violetta Impellizzeri, and Edward Fomalont. I want to thank my primary advisor Jim Braatz for his kindness and openness in the past few years in addition to teaching me many things in this project. Although my ideas were not always right, Jim always allowed me to explore my own ideas with great freedom. I benefit a lot from this open attitude because as a student who in

the past mostly followed the traditional eastern education system, which emphasizes too much on getting the standard answers and doing well in the exams, there were few chances we can learn to think out of box and explore/express our own ideas. It is the training in the MCP that help me enhance my creativity and taught me what good science really is.

I thank Mark Reid for providing two essntial programs for this project and my thesis work. Without his powerful programs, I wouldn't be able to make reliable measurements and modeling needed for the distance determinations for the two primary galaxies in this thesis. In addition, I learned many important things and techniques by using his programs. I thank Jim Condon for his great contributions and help to my thesis work. His encyclopedia-like knowledge in radio astronomy and deep insights have not only benefit myself, but also benefit all people in the MCP team. I also thank Christian Henkel for his frequent help for assisting our VLBI observations from the Effelsberg site.

My Chinese friends have been an important part of my life in the past six years. While there is still political tension and a gap between Taiwan and the Mainland China, I have made many good Chinese friends at UVa. These friendships not only help shorten the gap between both sides of the Taiwan straight, we also develop deep mutual respect and appreciation, and learn greatly from each other. I thank all of my dear Chinese friends here.

I thank deeply my parents for sending me to study in the US. While numerous families in Taiwan do not have sufficient economic power to send their children to study abroad and their children need to stay close to take care of their families and parents, my parents have kept themselves so healthy and have been working so hard (364 days per year) that I can concentrate on my study at UVa without any worry about their health and the economy of the family.

Finally, I need to thank immensely my primary Buddhist teachers Master Shinyin and my root guru His Holiness the 14th Dalai Lama Tenzin Gyatso. I thank Master Shinyin's great compassion and encouragement to me to study in US. Coming to the US has greatly opened my world view and allowed me to encounter the most important figure in my life, His Holiness the 14th Dalai Lama Tenzin Gyatso. His Holiness's teachings not only significantly help increase the degree of peace and compassion in my mind, His interests and insights in science also help me rid of conflicts between science and spirituality, both of which are critical parts of my life. This enables me to study both side by side, and use the knowledge and techniques from both disciplines to help each other. The only way I can reply the kindness of my glorious spiritual teachers is to continue to cultivate wisdom and compassion, and to help the sentient beings in the world as much as I can as a simple scientist.

Table of contents

List of Figures

List of Tables

Chapter 1

Introduction and Overview of the Megamaser Cosmology Project

We are in a golden age of cosmology. After Hubble's ground-breaking discovery of the expansion of the Universe, the field of cosmology has advanced extraordinarily over the past few decades. In addition to important discoveries such as the Cosmic Microwave Background (CMB) Radiation and large scale structure, observations of Type Ia supernovae in the late 1990's led to one of the most exciting and puzzling discoveries – the acceleration of the Universe (Riess et al 1998; Perlmutter et al. 1999).

Observational cosmology was once thought to be a search for two numbers: the Hubble constant H_0 and the deceleration parameter q_0 (Sandage 1970). Of these two, q_0 was considered to be particularly important for distinguishing different models of the Universe (Sandage et al. 1961). This simple picture of the cosmos changed dramatically after the cosmic acceleration was discovered, and this discovery opened a new era of cosmology research. "Dark Energy", which has negative pressure and accounts for 73% of the total energy density of the Universe, is currently the best candidate to explain the acceleration of the Universe. Since the cosmic acceleration was discovered, understanding the nature of dark energy has become one of the most important problems in modern astronomy and astrophysics.

There have been several very promising methods proposed to explore dark energy with high accuracy. Some methods use the Type Ia supernovae, the Baryon Acoustic Oscillation, galaxy clusters, or weak gravitational lensing as tools to probe dark energy (see Frieman, Turner, Huterer 2008) whereas there are also methods that constrain the equation-of-state parameter w by measuring an accurate Hubble constant H_0. In the *Megamaser Cosmology Project* (MCP; Reid et al. 2009a; Braatz et al. 2010), we take the latter approach and aim to determine the Hubble constant H_0 to 3% accuracy in order to measure w to 10%.

The key to a precise Hubble constant is to measure accurate distances to galaxies well into the Hubble flow (i.e. ≥ 50 Mpc). The galaxies must be distant to reduce the contribution of the uncertainty coming from peculiar velocities. While measuring precise distances to astronomical objects has always been important, direct distance measurements to galaxies in the Hubble flow has been challenging. In the past only indirect distance measurements through the *Extragalactic Distance Ladder* were obtained. Such an approach requires several calibration steps in the distance measurement, and since each step can have its own complexity, the final result from such an approach may be more susceptible to hidden systematic errors. A recent example is the different Hubble constants measured by Sandage et al. (2006; $H_0 = 62.3 \pm 5.2$ km s^{-1} Mpc^{-1}) and Freeman et al. (2001; $H_0 = 72 \pm 8$ km s^{-1} Mpc^{-1}).

Among all the approaches to measure precise distances, the megamaser method pioneered by the study of NGC 4258 (Herrnstein et al. 1999) has proven to be the most effective to make precise and direct distance measurements to galaxies beyond our Local Group. In the Megamaser Cosmology Project, we bypass the extragalactic distance ladder and apply the megamaser technique to galaxies in the Hubble flow, obtaining direct angular-diameter distances without any local calibration. Such an experiment was not possible in the past because of insufficient sensitivity to detect H_2O megamasers at sufficiently large distances. In the past decade, the advent of the 100-m Green Bank Telescope has made this project possible.

In this thesis, I will present the first results of applying the H_2O megamaser method to two galaxies beyond 100 Mpc and determine the Hubble constant directly without any local calibration. In addition, I will also present six new, accurate ($\sim$5%) black hole masses measured from precise rotation curves of sub-parsec megamaser disks, and discuss their implication for the nature of the famous $M_{\rm BH}-\sigma$ relation. In the remainder of this chapter, I will discuss the scientific background for dark energy, current status of H_0 measurements, and the methodology of the MCP.

1.1 Scientific Background: Dark Energy and its Relationship to the Hubble Constant

1.1.1 Introduction to dark energy

Within the framework of Einstein's theory of general relativity and assuming that the matter distribution is homogeneous on large scales, the Universe is expected to decelerate with time if the Universe is made of photons, dark matter, and baryonic matter. One can see this point from the Friedmann equations:

$$\left(\frac{\dot{a}}{a}\right) = \frac{8\pi G}{3c^2}\rho - k\frac{c^2}{a^2} \tag{1.1}$$

$$\frac{\ddot{a}}{a} = -\frac{4\pi G}{3c^2}\Big(\rho + 3p\Big), \tag{1.2}$$

where $a \equiv (1+z)^{-1}$ is a scale factor of the Universe, ρ is the total energy density (the sum of matter, radiation, dark energy), p is the total pressure, and k is the curvature parameter (k=0 for a flat Universe). Since for photons $\rho = 1/3p$, and for baryonic matter and cold dark matter $p << \rho$, the acceleration $\ddot{a}$ must be negative, according to Equation 1.2.

To explain the acceleration of the Universe while keeping the homogeneity assumption, the Einstein field equations must be modified. There are in general two ways to modify the field equations: either change the Einstein tensor on the left-hand side of the equations, or change the energy-stress tensor on the right-hand side:

$$R^{\mu\nu} - \frac{1}{2}g^{\mu\nu}R = -\frac{8\pi G}{c^4}T^{\mu\nu}, \tag{1.3}$$

where $R^{\mu\nu}$ is the Ricci curvature tensor, R the scalar curvature, and $\mathrm{g}^{\mu\nu}$ the metric tensor (the Einstein tensor $\mathrm{G}^{\mu\nu}$ is defined as $R^{\mu\nu} - \frac{1}{2}g^{\mu\nu}R$).

Changing the Einstein tensor of the field equations gives a modified theory of gravity. In this case, cosmic acceleration is a manifestation of new gravitational physics rather than the effect of a new form of energy or particle. A number of ideas have been explored along this line (Frieman, Turner, & Huterer 2008), from models motivated by higher-dimensional theories and string theory (Deffayet 2001; Dvali, Gabadadze, & Porrati 2000) to phenomenological modification of the Einstein-Hilbert Lagrangian of general relativity (Carrol et al. 2004; Song, Hu, & Sawicki 2007).

Compared to changing the Einstein tensor, modifying the stress-energy tensor part of the field equations has received much more attention from the astronomical community. While the physical meaning of the modification term is still obscure (i.e. the anti-gravity nature), one can easily explain the cosmic acceleration and a number of cosmological observations (see Frieman, Turner, Huterer 2008) by introducing a new energy-stress component called "dark energy" on the right-hand side of the field equations. The defining characteristic of dark energy is that it has an equation-of-state parameter, $w \equiv p/\rho$, less than -1/3. Such equation-of-state parameter is required by the Friedmann equations in order to generate positive acceleration $\ddot{a}$. However, the counterintuitive anti-gravity nature of dark energy implied by a negative equation of state still needs to be further studied in order to understand its physical meaning in depth.

The two current leading models for dark energy are the vacuum energy and quintessence. The vacuum energy is the simplest but at the same time most puzzling form of dark energy. In the Einstein field equations, it has a simple form on the right-hand side of the equations:

$$R^{\mu\nu} - \frac{1}{2}g^{\mu\nu}R = \frac{8\pi G}{c^4}T^{\mu\nu} - \Lambda g^{\mu\nu}, \tag{1.4}$$

where Λ is the cosmological constant first proposed by Einstein. This equation requires the pressure of the dark energy $\mathrm{p_{DE}} = -\rho_{\mathrm{vac}}$, where $\rho_{vac} \equiv \Lambda/8\pi c^4$ is the energy density of the quantum vacuum, and this relation implies that the equation-of-state parameter w=-1. Quantum vacuum has been a great puzzle for physicists because the observed value for dark energy is some 120 orders of magnitude lower than that predicted by quantum field theory. This is probably the worst theoretical prediction in the history of physics, and has been called the "cosmological constant problem". Some ideas, including the "anthropic principle" (Weinberg 1987), have been proposed to explain the low, but non-zero cosmological constant. More detailed discussion on possible solutions can been found in Frieman, Turner, & Huterer (2008).

Quintessence is another important candidate for dark energy. It literally means the "fifth element" and is a new scalar field ϕ in the Universe. For a scalar field ϕ with Lagrangian density $L = \partial^\mu \partial_\mu \phi - V(\phi)$, the stress-energy tensor takes the form of a perfect fluid (Frieman, Turner, Huterer 2008), with $\rho = \dot{\phi}^2/2 + V(\phi)$ and $p = \dot{\phi}^2/2 - V(\phi)$, where $\dot{\phi}^2/2$ is the kinetic energy and $V(\phi)$ is the potential energy. One of the major differences between quintessence and vacuum energy is that for various quintessence models the equation-of-state parameter w can take values between -1 and -1/3. In addition, rather than being constant in time and homogeneous in space, quintessence can in principle clump in space and its energy density and equation-of-state parameter can change with time. There have been ideas to adopt more complicated scalar fields to allow w to be less than -1 by modifying the kinetic term of the Lagrangian. Such examples include the phantom dark energy model.

No matter whether the cosmic acceleration is best explained by a modified theory of gravity or vacuum energy/quintessence, it will have deep implications and impact on our understanding of fundamental physics. Each possibility points us to a deeper level of reality. In the case of dark energy, one can perhaps appreciate the importance of understanding its nature best through Steven Weinberg's remark:

It is difficult for physicists to attack this problem (i.e. the nature of dark energy) without knowing just what it is that needs to be explained, a cosmological constant or a dark energy that changes with time as the universe evolves; and for this they must rely on new observations by astronomers. Until it is solved, the problem of dark energy will be a roadblock on our path to a comprehensive fundamental physical theory.

1.1.2 How to constrain the equation of state of DE

Dark energy affects the Universe in two distinct ways: (1) through the Friedman equations (Eq. 1.1 & 1.2), it alters the rate of expansion of the Universe, $H(z)$ and; (2) through the perturbation equation (e.g. Hu 2005), it affects the rate of growth of large-scale structures:

$$\frac{d^2\delta_m}{dt^2} + 2H(a)\frac{d\delta}{dt} = 4\pi G\rho_m\delta_m, \tag{1.5}$$

where $\delta_m \equiv \delta\rho_m/\rho_m$ is the density perturbation of non-relativistic matter. Therefore, to understand the nature of dark energy, one must measure the observables that are functions of either $H(z)$,or δ_m, or both. In particular, the primary observable for $H(z)$ is the distance to a cosmological object:

$$D(z) = c\int_0^z \frac{dz'}{H(z')}. \tag{1.6}$$

Note that the distance here is the *comoving* distance. The luminosity and angular-diameter distances can be calculated by dividing and multiplying the comoving distance by the scale factor $a(t) \equiv 1/(1+z)$.

Among the four most promising dark energy probes that do not involve the CMB, the Type Ia supernovae technique and the Baryon Acoustic Oscillation method constrain the DE properties mainly through $D(z)$; the technique involving measuring number density of galaxy clusters is sensitive to both $D(z)$ and $\delta\rho(z)$; and the weak gravitational lensing method that measures the spatial distribution and time evolution of dark matter probes DE purely through the growth rate of structure $\delta\rho(z)$.

In the Megamaser Cosmology Project, we aim to constrain the equation-of-state parameter of DE by measuring the Hubble constant to a few percent accuracy. An accurate Hubble constant has the power to constrain DE because the *angular-diameter* distance to the last scattering surface (LSS) of CMB photons, $D_* \equiv a(z_*)D(z_*)$, is a function of cosmological parameters including w and H_0. By determining D_* and the relevant cosmological parameters with the observables from the CMB anisotropy power spectrum, one can obtain a relationship between w and H_0. With this relation, the determination of the Hubble constant directly leads to a measurement of w. We explain the details as follows.

The acoustic features in the CMB anisotropy power spectrum (Figure 1.1) provide standard rulers for dark energy probes (Hu 2005). These features are the imprint of acoustic waves in the photon-baryon fluid when they were frozen at the epoch of recombination. The distance that these acoustic waves have traveled since the Big Bang to the time of recombination, s_*, is the most essential CMB standard ruler for probing dark energy here, and is the key to making an independent determination of D_*:

$$s_* = \int_0^{a_*} \frac{da}{a^2 H(a)} c_s(a) \tag{1.7}$$

where $c_s(a)$, the speed of the acoustic waves, only depends on the photon-baryon energy density ratio, and can be well determined by full analysis of the relative amplitudes of acoustic peaks in the power spectrum.

The values of s_* and D_* are related by the characteristic angular scale of the acoustic peaks in the power spectrum

$$l_A = \frac{\pi D_*}{s_*}. \tag{1.8}$$

Note that one cannot directly infer l_A from the multipole space positions of the acoustic peaks in the power spectrum. Rather, a phase correction (Hu et al. 2001) is needed through the following equation:

$$l_m = l_A(m - \phi_m), \tag{1.9}$$

where m labels the peak number, l_m is the position of the m-th peak, and ϕ_m is the phase correction that can be determined with full analysis of the CMB power spectrum. With the absolute calibration of s_*, the CMB then measures the angular diameter distance D_* to the LSS in absolute units. Based on the first year WMAP

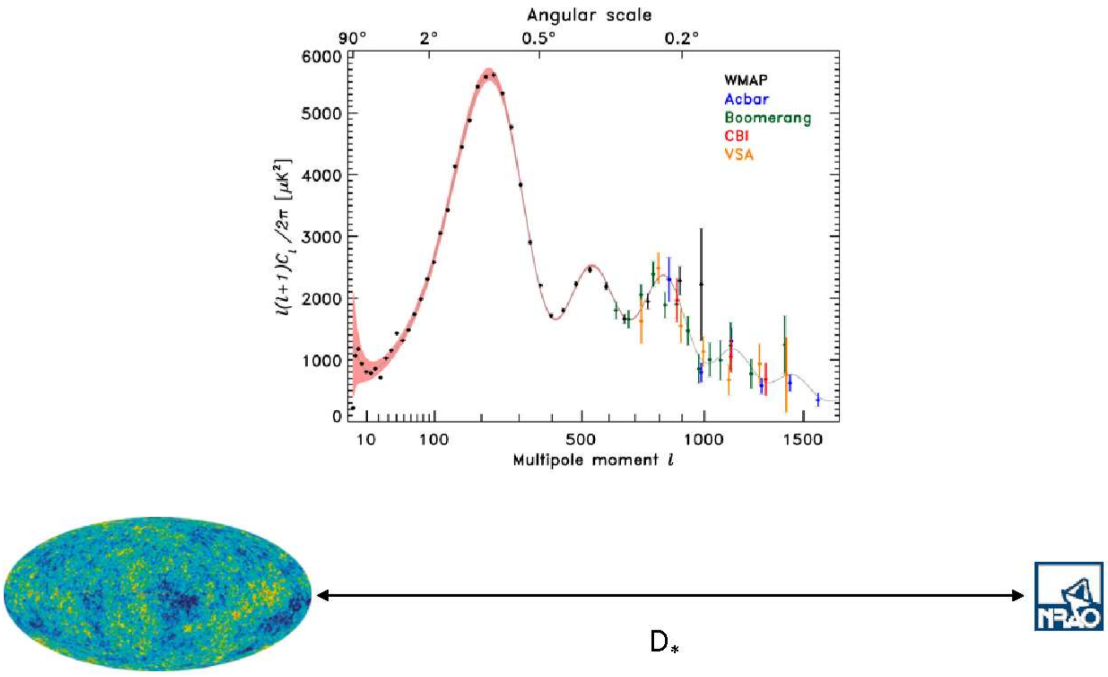

Fig. 1.1.— The top plot shows the CMB anisotropy power spectrum. These features seen in the spectrum are the results of the imprint of acoustic waves in the photon-baryon fluid when they are frozen at the epoch of recombination. The bottom plot shows the distance D_* to the last scattering surface of the CMB, which can be fully determined with the information in the power spectrum.

While D_* can be determined precisely with s_* and l_A, one can also express D_* as a function of cosmological parameters based on the standard cosmology[1]:

$$D(z_*) = \frac{1}{(1+z_*)} \int_0^{z_*} \frac{cH_0^{-1} dz}{\sqrt{((1+z)^3\Omega_m + (1+z)^4\Omega_r + (1+z)^{3(1+w)}\Omega_{DE}}} \, , \tag{1.10}$$

where Ω_m is the matter density, Ω_r is the radiation density, and Ω_{DE} is the dark energy density. For a flat Universe, Ω_{DE} is simply $1 - \Omega_r - \Omega_m$. In addition, $\Omega_m h^2$ and $\Omega_r h^2$ can be measured precisely from analyzing the CMB power spectrum (Page et al. 2003). So, with these measurable quantities, $D(z_*)$ is now only dependent upon two unknown parameters, w and H_0. Therefore, if one can constrain either of these two parameters, the other can be known. The better we constrain one parameter, the better we determine the other. In fact, as pointed out by Hu (2005), among all observables for probing DE *in light of the CMB*, w is most sensitive to variations in H_0. Hu (2005) concluded that *the single most important complement to the CMB for measuring the DE equation-of-state parameter w at $z\sim0.5$ is a determination of the Hubble constant to better than a few percent.* This insight forms the fundamental motivation for the Megamaser Cosmology project.

To see more intuitively how the accuracy of w and our ability to distinguish among DE models depend on the accuracy of the H_0 measurement, we use a figure from Braatz et al. (2006) for demonstration. In Figure 1.2, we compare w constrained from two different H_0 measurements (H_0 = 72 km s^{-1} from Freedman et al. 2001 and H_0=62 km s^{-1} from Sandage et al. 2006). As shown by the two plots on the left side of the figure, one cannot confidently distinguish quintessence models from vacuum energy if the Hubble constant measurement is only accurate to 10%. Both

---

[1] The flat geometry and constant w are assumed in the equation here for the purpose of explaining how to constrain w from a precise H_0 in a simpler way. The argument can be generalized to include the effect of curvature.

show results that are consistent with the vacuum energy model. However, if H_0 can be determined to 3% accuracy (say if H_0 is 62 km s^{-1} Mpc^{-1}), as shown by the two plots on the right, one can rule out the vacuum energy model with a confidence level $> 96\%$. These plots demonstrate that a precise Hubble constant is crucial to distinguish among different DE models.

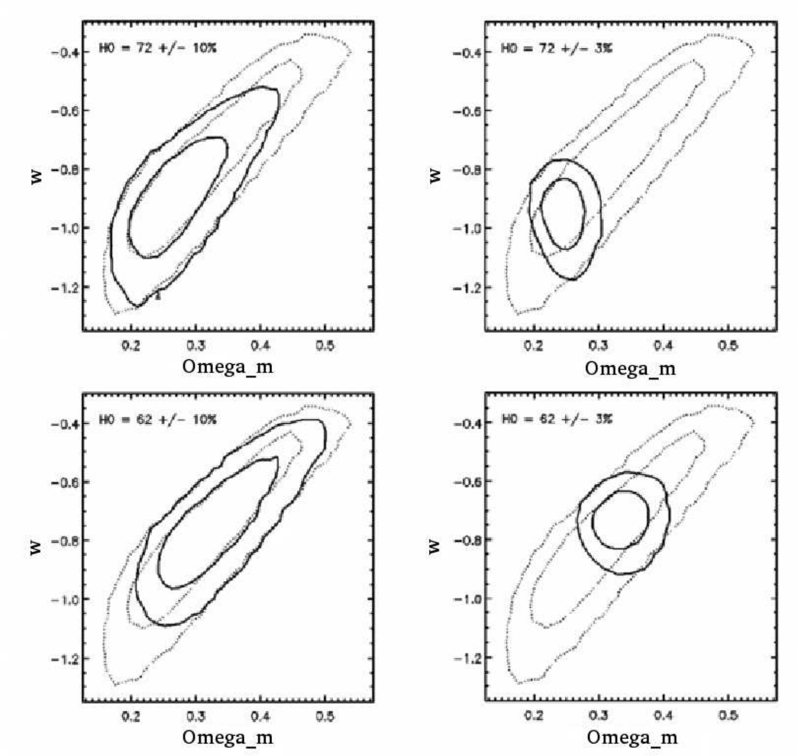

Fig. 1.2.— WMAP 1 σ and 2 σ (the inner and outer dotted lines) likelihood surfaces for w vs. Ω_m given priors on H_0. The solid lines show the improvements given by independent values of H_0=72 km s^{-1} Mpc^{-1} (top) and H_0=62 km s^{-1} Mpc^{-1} (bottom) with 10% (left) and 3% (right) errors.

1.2 Current Status of Hubble Constant

There has been considerable progress in determining the Hubble constant H_0 over the past two decades. After Hubble's fundamental discovery of the Hubble law in 1929 (Hubble 1929a), the most important milestone for precise H_0 determination was achieved by Freedman et al. (2001) who calibrated the secondary distance indicators (e.g. Type 1a supernovae) based on Cepheid Period-Luminosity (PL) relation using the Hubble Space Telescope (HST). They obtained an H_0 of 72±8 km s^{-1}Mpc^{-1}, the most widely accepted Hubble constant at the start of the Megamaser Cosmology Project.

The error in H_0 from Freedman et al. (2001) is dominated by systematic uncertainty. The primary sources of systematics consist of (1) the zero-point of the Cepheid PL relation, which was tied directly to the (independently adopted) distance to the Large Magellanic Cloud (LMC), the anchoring galaxy for the HST Key project (Freedman et al. 2001); and (2) the differential metallicity corrections to the PL zero point in going from the relatively low-metallicity (LMC) correction to target galaxies of different (and often higher) metallicities. Among these two systematics, the metallicity correction has been the most controversial.

It is known that the colors and magnitudes of Cepheid variables are affected by the metal abundances in their atmospheres (e.g. Freedman & Madore 2010). Therefore, their PL relations should be a function of metallicity. However, predicting the magnitude and the sign of the metallicity effect from a theoretical perspective has proven to be difficult (see references in Freedman & Madore 2010). Therefore, the metallicity corrections have usually been made empirically. With a different way to treat the metallicity effect, Sandage et al. (2006) obtained an H_0 of 62±5 km s^{-1}Mpc^{-1}. It was therefore thought by some people that the bulk of the difference in the Hubble constant between Sandage et al. (2006) and Freedman et al. (2001) comes from different metallicity corrections. However, after detailed analysis by Riess et al. (2009b), it has been shown that the bulk of the difference between Sandage et al. and Freedman et al. originates from inaccurate non-geometric distances to the Galactic Cepheids used in Sandage et al. (2006), their lack of sufficient number of long-period (P $>$ 30 days) Cepheids in the calibration, and error in the reddening correction. The error in the metallicity correction contributes less.

The most important progress in improving the systematic uncertainty of H_0 in the past decade has been made through improving the zero-point calibration and bypassing the controversial metallicity correction by basing the calibrations of the Cepheid PL relations on either new, accurate parallax distances of Galactic Cepheids (Freedman & Madore 2010) or Cepheids in the inner field of NGC 4258 (Riess et al. 2009, 2011). This approach not only has a stronger basis for accurate zero-point calibration of the PL relations, but most importantly it avoids the need for a significant metallicity correction because the Cepheids in the Galaxy and NGC 4258 have a comparable metal abundance to the galaxies from which the peak absolute magnitude of Type Ia supernovae is calibrated. The character of the metallicity uncertainty has changed from being a systematic to a random uncertainty. In addition to the aforementioned approach, the metallicity effect has been further reduced by measuring Cepheids in the near-infrared, where the metallicity dependence is diminished (see Riess et al. 2009).

With the new approaches to reduce systematic errors, Freedman & Madore (2010) give an H_0 of 73±5 km $\mathrm{s}^{-1}\mathrm{Mpc}^{-1}$, and Riess et al (2009) & (2011) give an H_0 of 74±4 km $\mathrm{s}^{-1}\mathrm{Mpc}^{-1}$ and 74±2 km $\mathrm{s}^{-1}\mathrm{Mpc}^{-1}$, respectively. These new H_0 measurements lead to a new constraint on the equation-of-state parameter of dark energy with $\sim$10%

accuracy. The authors aim to improve H_0 to 1-2% accuracy in the coming decades with more accurate parallax distances of Galactic Cepheids from GAIA (and perhaps SIM) for accurate zero-point calibration of the PL relations, and with observations of Cepheids at mid-IR with JWST to reduce the metallicity effect and scatter in the PL relations. While these authors have claimed obtaining a percentage level Hubble constant, we have to caution the reader that part of the calibrations in Riess et al. (2009) and (2011) are based on an assumed 3% maser distance to NGC 4258. One should note that a 3% distance to NGC 4258 has not yet been achieved by any group, and the 3% is just the anticipated goal with all the new observations on NGC 4258 (Argon et al. 2007; Humphreys et al 2008), which are still being analyzed (Ried; private communication). Therefore, the actual uncertainties from the work of Riess et al. should actually be higher than what they have claimed.

While there has been significant improvement in the Hubble constant measurement in the optical, given the complexity and multiple steps involved in the calibration process, there could be still hidden systematic errors. Therefore, an independent measurement of the Hubble constant without appealing to the Extragalactic Distance Ladder would be highly valuable. The most promising approach that can measure H_0 without the need to resort to other cosmological parameters is the H_2O Megamaser technique (e.g. Herrnstein et al. 1999; Braatz et al. 2010). With precise astrometry observations with VLBI, the H_2O Megamaser technique can potentially be used to measure distances to galaxies out to ~200 Mpc. Since these galaxies are already in the Hubble flow, a direct measurement of H_0 with megamaser galaxies can be done without the Extragalactic Distance Ladder and any local calibration. Such a measurement would be unprecedented. Finally, even when the maser galaxies are too close to be in the Hubble flow, more accurate maser distances to these galaxies can also be used as the anchors for calibrating the Extragalactic Distance Ladder and be used to check the accuracy of the previous calibrations based on Cepheids in the LMC, Milky Way and NGC 4258.

1.3 Direct Angular Diameter Distance Measurement with the H_2O Megamaser Method

The H_2O megamaser method involves sub-milliarcsecond resolution imaging and single-dish monitoring of H_2O maser emission from sub-parsec circumnuclear disks at the center of active galaxies, a technique first established by the study of NGC 4258 with VLBI (Herrnstein et al. 1999). In this technique, one determines the distance to a maser galaxy by measuring four orbital parameters (i.e. the radius, velocity, acceleration, and inclination of an orbit) with precise maser positions, velocities, and accelerations. Here, we use the example of NGC 4258 (Herrnstein et al. 1999), UGC 3789 (Braatz et al. 2010) and a cartoon plot to explain the principle behind this technique.

Figure 1.3 shows a cartoon plot of masing gas orbiting around a supermassive black hole in a circular orbit at the center of a galaxy. D is the distance from the observer to the galaxy, r is the physical radius of the orbit, and $\Delta\theta$ is apparent angular radius seen by the observer. Based on simple geometry, we can express the distance as

$$D = \frac{r}{\Delta\theta} \ . \tag{1.11}$$

According to Newton's second law, the gravitational acceleration a of the masing gas

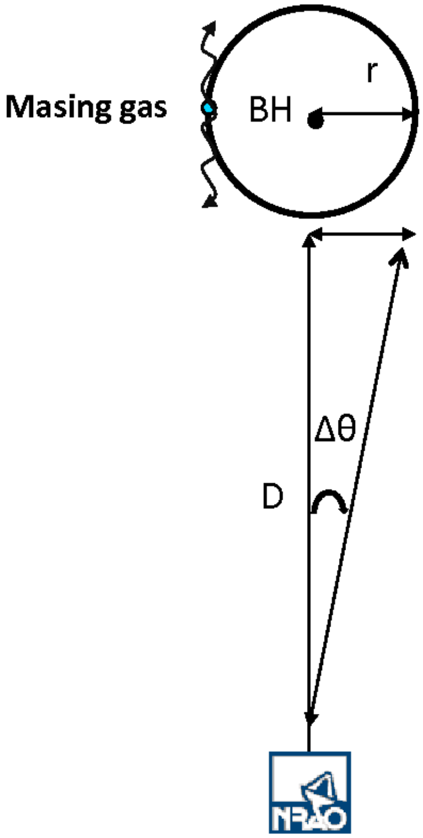

Fig. 1.3.— A model to illustrate how we determine the distance a galaxy with a H_2O maser disk

in the circular orbit is related to the orbital velocity v_0 and physical radius r with

$$a = \frac{v_0^2}{r} \ . \tag{1.12}$$

For convenience, the above equation can be re-written as

$$r = \frac{v_0^2}{a} \ . \tag{1.13}$$

By combining Equations 1.11 & 1.13, and correcting the maser velocity and acceleration for the inclination of the orbit, the distance D can be expressed as

$$D = \frac{v_0^2}{a\ \Delta\theta}\ sin\ i\ . \tag{1.14}$$

Therefore, one can determine an accurate distance to a megamaser galaxy if the four parameters in Equation 1.14 can be determined precisely. Now, let's use the real data from NGC 4258 and UGC 3789 to illustrate how to measure these parameters.

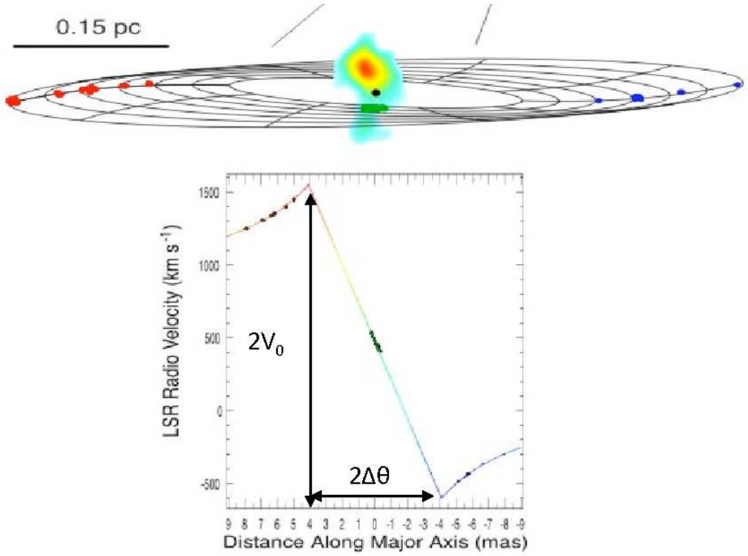

Fig. 1.4.—

Figure 1.4 shows the the maser distribution and the position-velocity (PV) diagram of the H_2O maser disk at the center of NGC 4258. The black hole is sitting at the center of the disk with a jet ejected toward the top and bottom side of the disk. The data points in the VLBI maps and rotation curves are color-coded to indicate redshifted, blueshifted (the redshifted/blueshifted masers are also called "high velocity" masers throughout the thesis), and systemic masers, where the "systemic" masers refer to the maser spectral components having velocities close to the systemic velocity of the galaxy. Note that the redshifted and blueshifted masers are located very close to the mid-line (the intersection of the plane of the sky and the disk) of the disk and can be traced nearly perfectly with a Keplerian rotation curve in the PV diagram. The systemic masers are located in front of the black hole[2], and in the PV diagram they can be beautifully fit with a straight line, a feature that indicates that these masers lie in a single narrow ring in the disk.

As shown in Figure 1.4, the intersection between the straight line and the Keplerian rotation curve that fit the systematic and high velocity masers directly give the orbital velocity V_0 and angular size $\Delta\theta$ of the ring in which the systemic masers reside. In addition, with the angular offset y of the systemic masers from the black hole in the vertical direction, one can obtain the inclination i of the orbit for systemic masers

$$i = cos^{-1}(\frac{y}{\Delta\theta}) \ . \tag{1.15}$$

Therefore, one can obtain three parameters for the distance measurement from VLBI observation. The remaining parameter, a, has to be measured from multi-epoch monitoring of maser spectra. Here, we use UGC 3789 from Braatz et al. (2010) to illustrate how to measure the centripetal acceleration of H_2O masers.

It is believed that the origin of the accelerations of H_2O masers that we observe is the centripetal acceleration due to the gravity of the black hole at the center of maser disk. That the maser is accelerating does not mean that the masing gas is spiraling toward the black hole. Rather, they stay in a circular orbit because the acceleration

---

[2] The mid-line of the disk and places in front of the black hole are particularly favorable for maser emission because in these locations the path lengths for maser amplification reach maximum values (Lo 2005).

due to gravity is balanced by the centrifugal acceleration that keeps the object in orbit. While the orbital speed remains the same, the centripetal force causes the masing gas to keep changing directions in order to maintain the circular orbit, and therefore the line-of-sight velocity seen by the observer will keep changing. The rate of change in the observed maser velocity is the centripetal acceleration along the line of sight that we want to measure.

In the top-left panel of Figure 1.5 is an H_2O maser spectrum for UGC 3789 with the zoom-in spectrum for the systemic masers on the bottom. We can see several distinct lines in the spectrum. Because of the gravitational acceleration, we expect that the systemic maser lines will drift toward higher velocities (i.e. toward the right) with time, and this is indeed seen in the middle panel of Figure 1.5. Here, we plot the velocities of maser lines we can identify in the spectra from multi-epoch observations as a function of time. As we expect, we do see clear positive trends, and the slopes of the lines that fit the data directly measure the maser accelerations. For maser disks of sub-pc size with $\sim 10^7 M_\odot$ black holes, the acceleration is typically a few km $s^{-1}yr^{-1}$. On the other hand, since the maser lines are often blended and can have significant variability over timescales of a few months to years, in order to reduce systematic error caused by blending and variability, it is usually necessary to improve the acceleration measurement by detailed modeling of maser lines with a global fitting program that fits all lines in all epochs simultaneously (see the right panel of Figure 1.5 as an example).

It is possible to have substantial accelerations caused by forces other than the gravity of the black hole. The shocks due to spiral density waves in a maser disk, if they exist, can cause non-gravitational acceleration for the masing gas (Maoz & McKee 1998). In addition, the local gravity of over-dense regions of the spiral waves

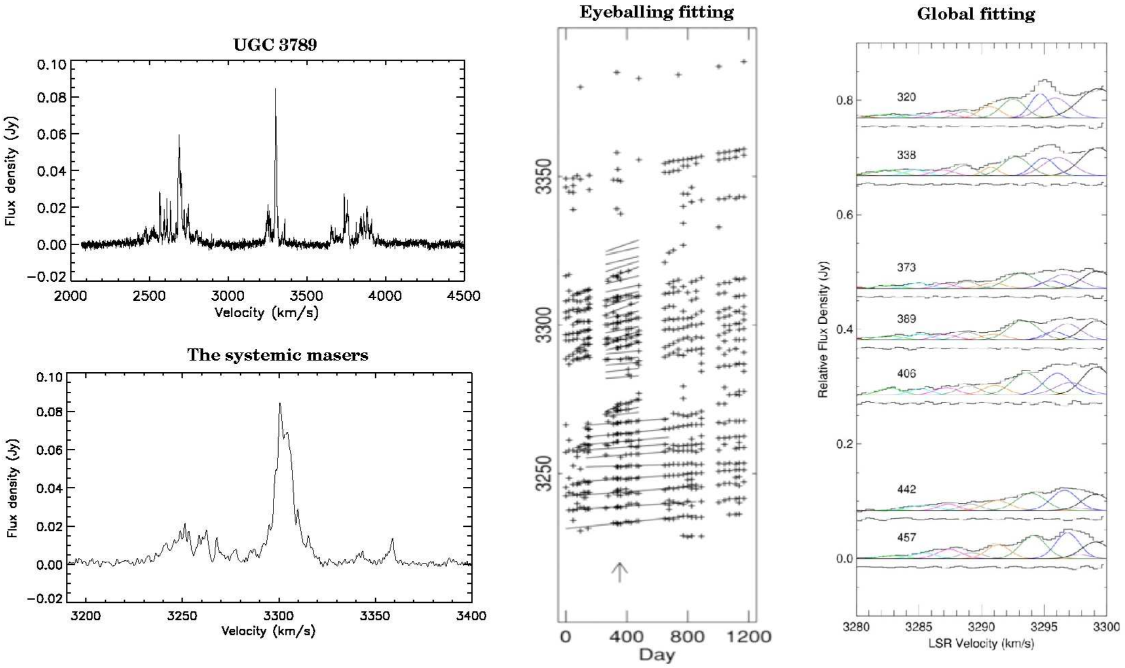

Fig. 1.5.— The top-left plot shows an H_2O maser spectrum of UGC 3789, with the spectrum for the systemic masers at the bottom. In the middle panel we plot the velocities of the systemic maser lines as a function of time. The slopes of the fitted straight lines (the solid lines) directly give the accelerations of the masers. In the right panel, we fit a part of the systemic maser spectrum with a program (Reid, M.; private communication) that fits multiple lines at multiple epochs simultaneously in order to remove the systematic effects of line blending and variability. Illustrations and figures are from Braatz et al. (2010).

can also introduce additional acceleration for masing gas in the disk (Humphreys et al. 2008). If these extra accelerations do exist and are not accounted for in the distance determination, there will be additional systematic errors. Therefore, one may need a good theoretical model for the density waves in the maser disk to estimate the magnitude of the non-gravitational acceleration and understand its impact on the distance measurement.

1.4 Strategy of the MCP

In order to determine the Hubble constant to 3% accuracy, we aim to measure accurate (i.e. $\leq$10%) distances to about 10 maser galaxies in the Hubble flow (i.e. $\geq$50 Mpc). To achieve this goal, in addition to precise VLBI astrometry for these galaxies, we also need sensitive large surveys to find more megamaser galaxies similar to NGC 4258. In the MPC, we follow a four step approach:

1. Survey with the Green Bank Telescope (GBT) to identify additional high-quality disk masers in the Hubble flow for $\sim$10% distance measurements.

2. Image the sub-pc megamaser disks to obtain their rotation curves with the High Sensitivity Array (VLBA+GBT+EB)[3]

3. Measure accelerations of masers accurate to $<<$ 10% by monitoring their spectra over a timescale of a few years.

4. Determine the distance to maser host galaxies by modeling the maser disk kinematics. Along with the best fit recession velocity of maser galaxies, we use the maser distance to measure the Hubble constant.

As the MCP continues to discover and image megamaser disks, an important result, in addition to the distance determination, is the accurate measurement of the masses of black holes at the centers of these megamaser galaxies. These accurate black hole masses provide an important basis for testing and understanding the nature of the famous correlation between black hole mass and stellar velocity dispersion of a galactic bulge, the $M_{\rm BH}-\sigma$ relation.

---

[3] The VLBA is a facility of the National Radio Astronomy Observatory, which is operated by the Associated Universities, Inc. under a cooperative agreement with the National Science Foundation (NSF). The Effelsberg 100-m telescope is a facility of the Max-Planck-Institut für Radioastronomie

1.5 Thesis Overview

As a part of the Megamaser Cosmology Project, the observational aspect of this thesis focuses primarily on the Very Long Baseline Interferometry (VLBI) imaging of the current best megamaser disks. The surveys were mainly conducted by Braatz et al. (in prep), Braatz & Gugliucci (2009), and previous work. In Chapter 2, I will first give a brief summary of the current status of our survey, followed by the presentation of the sample of maser galaxies, VLBI observations and data reduction. The full detailed data reduction procedure for the VLBI observations in the MCP will be presented in the appendix. In Chapter 3, I will show the VLBI results of the current best seven megamaser disks in MCP, present the analysis of BH masses based on the VLBI results, investigate the validity of our assumption that we are truly measuring the masses of black holes and finally discuss the implication of these black hole masses for the $M_{\rm BH}{-}\sigma$ relation.

In Chapter 4, I present the analysis of the acceleration measurements for two of the maser galaxies (NGC 6323 and NGC 6264) that we target for geometric distances with the megamaser technique. The actual distance determinations for these two galaxies will be discussed in Chapter 5, along with the discussion of the possible systematic uncertainties for the megamaser technique. In Chapter 6, I summarize the whole thesis.

Chapter 2

The Survey, Sample, Imaging, and Data Reduction

2.1 Qualified Maser Disks for the MCP

Accurate distance measurement with the H_2O megamaser technique requires maser disks to satisfy a few criteria to minimize both statistical and systematic errors: (1) The system must be rich in bright features at both systemic and high velocities; (2) The maser lines need to be bright enough (i.e. ≥ 30 mJy) for self-calibration; (3) The systemic masers should show clear accelerations; and (4) The high velocity features must obey Keplerian rotation. While the last two requirements are self-evident and indispensible for distance measurement, the first two points deserve more elaboration.

Rich maser features with high flux densities are critical in many aspects of the MCP. In the initial stage of the MCP, the peak flux of a maser system usually needs to be higher than 100 mJy in order to make self-calibration possible. Otherwise, we have to observe the maser galaxies in phase-referencing mode, and this has proven to be too inefficient to obtain sufficient sensitivity in a reasonable amount of time. Since it is rare for maser galaxies beyond 50 Mpc to have fluxes higher than 100 mJy, over the past few years, we have developed a new technique that makes self-calibration feasible with masers of only $\sim$ 30 mJy. However, multiple such maser lines are necessary for applying this new technique (see section 2.4 for a brief description).

High maser flux density is also important for VLBI astrometry and accurate acceleration measurements of masers. The relative position accuracy $\delta\theta$ of a maser spot (presumably a point source) in the VLBI imaging is

$$\delta\theta = \frac{\theta_{beam}}{2\ SNR}\ , \tag{2.1}$$

where θ_{beam} is the synthesized beam size and SNR is the signal-to-noise ratio of the maser spot in the map. Since $\sim$5 μarcsec position accuracy is usually necessary to measure distance precisely, the optimal flux density of the systemic masers would be $\geq$ 30 mJy for an average beam of 0.5 mas and a 12-hour VLBI observation that includes the Very Long Baseline Array (VLBA)[1], the 100-m Green Bank Telescope (GBT) and the Effelsberg 100-m telescope[2]. In addition to the position accuracy of masers, the precision of acceleration measurements also depends on SNR. While there are many factors that can affect the accuracy of acceleration measurements (e.g. blending, variability, time baseline), in general higher SNR is necessary for accurate acceleration determination. Based on current experience, multiple lines with flux density $>$ 10 mJy are required for a $\approx$10% measurement if the acceleration is relatively high (e.g. 4 km s^{-1} yr^{-1}). For masers with low accelerations (e.g. $<$ 1 km s^{-1} yr^{-1}), flux densities above $\sim$40 mJy would be needed. For megamaser galaxies well in the

---

[1] The VLBA is a facility of the National Radio Astronomy Observatory, which is operated by the Associated Universities, Inc. under a cooperative agreement with the National Science Foundation (NSF).

[2] The Effelsberg 100-m telescope is a facility of the Max-Planck-Institut für Radioastronomie

Hubble flow ($\geq$ 70 Mpc), these requirements mean that the maser galaxies needed for the MCP must be intrinsically brighter than NGC 4258 (Distance = 7.2 Mpc).

Based on how well H_2O maser disks satisfy the above requirements, we divide the discovered maser disks into three classes:(1) "Class A" disks satisfy all these requirements well and can be used to measure distances; (2) "Class B" disks do not satisfy the requirements for distance measurement, but have multiple, detectable high velocity spots that enable measurement of the black hole mass; and (3) "Class C" disks are currently too faint for either distance or black hole mass measurement, but are monitored once or twice per year in search of flares that would elevate them to Class A or B.

In order to find additional maser galaxies for distance and black hole mass measurement, surveys are very important. In this thesis, I will only briefly mention the result of the surveys. Details of the MCP surveys are forthcoming in Braatz et al. (2011).

2.2 The Megamaser Disk Sample

In the MCP, we used the 100-m Green Bank Telescope (GBT) to search for H_2O megamasers in narrow-line AGNs, primarily drawn from the Sloan Digital Sky Survey and the all-sky 2MASS Redshift Survey, plus a smaller number of X-ray selected AGN and "apparently normal" galaxies (cf. Braatz & Gugliucci 2008). We mainly look for H_2O megamasers in narrow-line AGNs because based on the standard AGN model these galaxies are more likely to host edge-on accretion disks, which are preferable for megamasers to occur.

Most megamasers discovered in the past decade were found with the GBT, mainly by surveys associated with the MCP in which the overall detection rate is $\sim$3%.

Altogether, there are 146 galaxies detected as sources of H_2O maser emission[3]. Most of the H_2O maser emitters originate in AGN (Lo 2005). Based on the post-detection statistics, about 20% of them show spectra suggestive of emission from sub-parsec scale, edge-on, circumnuclear disks. The rest of the H_2O maser sources among the 146 galaxies are most likely associated with starburst activity in the nuclear regions of these galaxies.

In the MCP, we have been conducting VLBI observations of four "Class A" megamaser disks (UGC 3789, MRK 1419, NGC 6323, and NGC 6264) to determine their angular diameter distances and black hole masses. The distance measurements for NGC 6264 and NGC 6323 will be the focus of this thesis. In addition to these Class A objects, we also have VLBI data on three "Class B" megamaser disks (NGC 4388, NGC 1194, and NGC 2273) for which we would not determine accurate distances but can still make precise black hole mass measurements (Chapter 3). Table 2.1 lists coordinates, recession velocities, spectral types, and morphological types for these seven galaxies.

---

[3] https://safe.nrao.edu/wiki/bin/view/Main/MegamaserCosmologyProject

Table 2.1. The Megamaser Sample

Name	R.A. (J2000)	Decl. (J2000)	δRA (mas)	δDEC (mas)	V_{sys} (km s^{-1})	δV_{sys} (km s^{-1})	Spectral Type	Hubble Type
NGC 1194	03:03:49.10864[a]	−01:06:13.4743[a]	0.2	0.4	4051	15	Sy 1.9	SA0+
NGC 2273	06:50:08.65620[b]	60:50:44.8979[b]	10[h]	10[h]	1832	15	Sy 2	SB(r)a
UGC 3789	07:19:30.9490[c]	59:21:18.3150[c]	10[h]	10[h]	3262	15	Sy 2	(R)SA(r)ab
NGC 2960	09:40:36.38370[d]	03:34:37.2915[d]	10[h]	10[h]	4945	15	Liner	Sa?
NGC 4388	12:25:46.77914[e]	12:39:43.7516[e]	0.4	0.3	2527	1	Sy 2	SA(s)b
NGC 6264	16:57:16.12780[f]	27:50:58.5774[f]	0.3	0.5	10213	15	Sy 2	S ?
NGC 6323	17:13:18.03991[g]	43:46:56.7465[g]	0.2	0.4	7848	10	Sy 2	Sab

Note. — (1)The systemic (recessional) velocities of the galaxies, V_{sys}, listed here are based on the “optical” velocity convention (i.e. no relativistic corrections are made) , measured with respect to the Local Standard of Rest (LSR). Except NGC 4388, the systemic velocities V_{sys} are obtained from fitting a Keplerian rotation curve to the observed data as described in section 3. The uncertainties δV_{sys} given here include both the fitting error and a conservative estimate of the systematic error. The fitting error is typically only about 5 km s^{-1} and the systematic error is from possible deviation of the position of the BH from $(\theta_x, \theta_y) = (0, 0)$ (see section 3), which is assumed in our rotation curve fitting. For NGC 4388, we adopt the observed HI velocity from Lu et al. (2003), which has a small but perhaps unrealistic error. (2) The positions of UGC 3789, NGC 1194, NGC 6323, and NGC 4388 refer to the location of maser emission determined from our VLBI phase-referencing observations. The positions of NGC 2273 and NGC 2960 are determined from K-band VLA A-array observations of continuum emission from program AB1230 and maser emission from AB1090, respectively. The maser position for NGC 6264 is derived from a phase-referencing observation in the VLBA archival data (project BK114A). (3) The Seyfert types and morphological classifications are from the NASA/IPAC Extragalactic Database (NED).

[a] The position of the maser spot at $V_{op} = 4684$ kms^{-1}, where V_{op} is the “optical” velocity of the maser spot relative to the LSR.

[b] The position of the radio continuum emission observed at 21867.7 MHz and 21898.9 MHz.

[c] The position of the maser spot at $V_{op} = 2689$ kms^{-1}.

[d] The position of the maser spot at $V_{op} = 4476$ kms^{-1}.

[e] The position of the maser spot at $V_{op} = 2892$ kms^{-1}.

[f] The average position of the masers with velocities from $V_{op} = 10180$ kms^{-1} to $V_{op} = 10214$ kms^{-1}

[g] The position of the maser spot at $V_{op} = 7861$ kms^{-1}.

[h] For all positions derived from VLA observations, we use 10 mas as the actual position error, rather than the fitted errors from the VLA data, which are only a few mas for these galaxies. The reason is that the systematic error caused by the imperfect tropospheric model of the VLA correlator can be as large as a few to 10s mas. A 10 mas position error usually leads to a $\approx 3 - 5\,\%$ error in the BH mass for the megamasers presented here. Note that although the position for UGC 3789 is derived from a VLBI phase-referencing observation with a phase calibrator 2.1° away, the position of this calibrator is derived from a VLA observation. So, we also use 10 mas as the actual position accuracy for UGC 3789.

2.3 VLBI Observations

The megamaser galaxies in our sample were observed between 2005 and 2010 with the VLBA, augmented by the GBT and in most cases the Effelsberg 100-m telescope. Table 2.2 shows the basic observing information including experiment code, date observed, antennas used, and sensitivity.

We observed the megamasers either in a phase-referencing or self-calibration mode. With phase-referencing we perform rapid switching of the telescope pointing between the target source and a nearby ($< 1^\circ$) phase calibrator (every ~ 50 seconds) to correct phase variations caused by the atmosphere. In a self-calibration observation, we use the brightest maser line(s) to calibrate the atmospheric phase. In both types of observations, we placed "geodetic" blocks at the beginning and end of the observations to solve for atmosphere and clock delay residuals for each antenna (Reid et al. 2009b). For NGC 6323 and NGC 6264, we also placed a geodetic block in the middle of the observations to avoid the zenith transit problem at the GBT and to obtain better calibration. In each geodetic block, we observed 12 to 15 compact radio quasars that cover a wide range of zenith angles, and we measured the antenna zenith delay residuals to ~ 1 cm accuracy. These geodetic data were taken in left circular polarization with eight 16-MHz bands that spanned ~ 370 - 490 MHz bandwidth centered at a frequency around 22 GHz; the bands were spaced in a "minimum redundancy" manner to sample, as uniformly as possible, all frequency differences between IF bands in order to minimize ambiguity in the delay solution (Mioduszewski & Kogan 2009). We also observed strong compact radio quasars every ~ 20 minutes to 2 hours in order to monitor the single-band delays and electronic phase differences among and across the IF bands. The errors of the single-band delays are < 1 nanosecond.

Table 2.2. Observing Parameters

Experiment Code	Date	Galaxy	Antennas[a]	Synthesized Beam (mas x mas,deg)[b]	Sensitivity (mJy)	Observing Mode[c]
BB261[d]	2005 Mar 06	UGC 3789	VLBA, GB, EB	0.55×0.55, 39.0	1.0	Self-cal.
BB242B[e]	2007 Nov 13	NGC 1194	VLBA, GB	2.45×0.36,−7.5	∼ 1.5	Self-cal.
BB242D[e]	2008 Jan 21	NGC 1194	VLBA, GB	1.83×0.44, −10.5	2.1	Phase-ref.
BB261B	2009 Feb 28	NGC 2273	VLBA, GB	0.69×0.39, −22.4	0.5	Self-cal.
BB261F	2009 Apr 06	NGC 6264	VLBA, GB, EB	0.93×0.38,−24.8	0.5	Self-cal.
BB261H	2009 Apr 18	NGC 6264	VLBA, GB, EB	1.02×0.29,−14.7	0.3	Self-cal.
BB261K	2009 Nov 25	NGC 6264	VLBA, GB, EB, VLA	1.10×0.30,−9.7	0.5	Self-cal.
BB261Q	2010 Jan 15	NGC 6264	VLBA, GB, EB	0.80×0.24,−11.8	0.5	Self-cal.
BB231E	2007 Apr 07	NGC 6323	VLBA, GB, EB	0.58×0.24,−13.6	0.8	Phase-ref.
BB231F	2007 Apr 08	NGC 6323	VLBA, GB, EB	0.58×0.27,−14.8	0.8	Phase-ref.
BB231G	2007 Apr 09	NGC 6323	VLBA, GB, EB	0.92×0.32,−5.8	0.8	Phase-ref.
BB231H	2007 Apr 29	NGC 6323	VLBA, GB, EB	0.90×0.28,−13.5	1.3	Phase-ref.
BB242F	2008 Apr 13	NGC 6323	VLBA, GB	0.95×0.44,−9.4	0.8	Phase-ref.
BB242E	2008 Apr 14	NGC 6323	VLBA, GB	0.90×0.49,−9.2	0.8	Phase-ref.
BB242G	2008 Apr 16	NGC 6323	VLBA, GB	0.79×0.45,−10.2	1.0	Phase-ref.
BB242H	2008 Apr 19	NGC 6323	VLBA, GB	0.80×0.45,−4.2	0.3	Self-cal.
BB242J	2008 May 23	NGC 6323	VLBA, GB, EB	0.58×0.21,−8.1	1.7	Phase-ref.
BB242M	2009 Jan 11	NGC 6323	VLBA, GB, EB	0.52×0.29,−17.8	0.4	Self-cal.
BB242R	2009 Apr 17	NGC 6323	VLBA, GB, EB	0.87×0.45,12.2	0.5	Self-cal.
BB242S	2009 Apr 19	NGC 6323	VLBA, GB, EB	0.57×0.26,−21.2	0.4	Self-cal.
BB242T	2009 Apr 25	NGC 6323	VLBA, GB, EB	0.75×0.23,−19.0	0.8	Self-cal.
BB248[f]	2009 Mar 07	NGC 2960	VLBA, GB, EB	0.97×0.45, 5.3	2.5	Self-cal.
BB261C[f]	2009 Mar 20	NGC 2960	VLBA, GB, EB	1.11×0.48,2.6	1.1	Self-cal.
BB261D[f]	2009 Mar 23	NGC 2960	VLBA, GB, EB	1.26×0.44, −2.1	1.3	Self-cal.
BB184C	2006 Mar 26	NGC 4388	VLBA, GB, EB	1.23×0.32, −9.27	1.8	Phase-ref.

[a] VLBA: Very Long Baseline Array; GB: The Green Bank Telescope of NRAO; EB: Max-Planck-Institut für Radioastronomie 100 m antenna in Effelsberg, Germany; VLA: The Very Large Array of NRAO.

[b] Except for program BB184C, this column shows the average FWHM beam size and position angle (PA; measured east of north) at the frequency of systemic masers. For BB184C, the FWHM and PA is measured at the frequency of red-shifted masers because no systemic maser is detected (FWHM and PA differ slightly at different frequencies).

[c] "Self-cal." means that the observation was conducted in the "self-calibration" mode and "Phase-ref." means that we used the "phase-referencing" mode of observation.

[d] The data reduction of this dataset was done by Mark Reid from the Harvard Smithsonian Center for Astrophysics.

[e] The data reduction of this dataset was done by Ingyin Zaw from New York University in Abu Dhabi.

[f] The data reduction of this dataset was done by Violetta Impellizzeri from NRAO.

2.4 VLBI Data Reduction

The VLBI data reduction in the MCP is intrinsically more complicated than usual VLBA data. The main reason is that each dataset often has its own personality and problems, and we usually need to take different approaches to deal with issues we encounter. Therefore, creating a universal pipeline for the VLBI data reduction in the MCP has been very difficult, and we can only resort to dividing the data reduction procedure into several parts and writing a smaller pipeline in the form of an AIPS RUN file for each part in order to optimize the efficiency for data reduction. Moreover, the whole data reduction procedure is relatively long, and it is easy to make mistakes. Therefore, a careful and patient attitude for data reduction in the MCP is also important to reduce the possibility of errors. In this section, I will discuss the general procedure for the VLBI data reduction in the MCP, and defer the step-by-step procedure of data reduction to the appendix.

We calibrated all the data using the NRAO Astronomical Image Processing System (AIPS). Since the geodetic data and the maser data used different frequency settings, we reduced them separately. For the geodetic data, we first calibrated the ionospheric delays using total electron content measurements (Walker & Chatterjee 2000) and the Earth Orientation Parameters (EOPs) in the VLBA correlators with the EOP estimates from the US Naval Observatory[4]. We then perform "fringe fitting" on one or two scans of the delay calibrators to calibrate the electronic phase offsets among and across IF bands. After the electronic phase offsets were removed, we performed fringe fitting again to determine the atmospheric phases, single-band delays, and fringe rates of IF bands of each antenna for every geodetic source. The multi-band delay of each antenna was determined from these solutions afterward. Fi-

---

[4] http://gemini.gsfc.nasa.gov/solve_save/usno_finals.erp

nally, we determined the residual tropospheric delay and clock errors for all antennas using the multi-band delays. We applied these corrections to the maser data as described in the next paragraph. In five datasets for NGC 6323, we also made antenna position corrections before the fringe-fitting process when the positions used in the observation deviated from the latest USNO[5] solutions by more than ~ 2 cm.

For the maser data, after the initial editing of bad data, we corrected for ionospheric delay and the EOPs in the same way as for the geodetic dataset. We then corrected the sampler bias in the 2-bit correlator. The amplitude calibration was done with the information in the gain table and the system temperature table. We corrected the interferometer delays and phases caused by the effects of diurnal feed rotation (parallactic angle), and applied the tropospheric delay and clock corrections obtained from the geodetic data afterward. The next step was to perform fringe fitting on one or two scans of the delay calibrators to calibrate the electronic phase offsets among and across IF bands. The frequency axes of the maser interferometer spectra were then shifted to compensate for the changes in source Doppler shifts over the observing tracks.

The final step in calibration was to solve for the atmospheric phase variation by using either phase-referencing or self-calibration. In the phase-referencing mode, we ran the AIPS task CALIB on the phase calibrator to determine the phase correction as a function of time for each individual IF band. In the self-calibration mode, we either selected a single strong maser line or averaged multiple maser lines in narrow ranges of both velocity (within a single IF band) and space to perform phase calibration, and then copied the solution table to all the other IF bands. The typical solution interval for self-calibration was 100 seconds. In the dataset BB261K and BB261Q for NGC 6264, no maser line(s) within a single IF band is(are) strong enough to perform

---

[5] http://rorf.usno.navy.mil/solutions/

good calibration and the scatter of the phase solutions were relatively large. In order to increase the signal-to-noise ratio, we combined all strong maser lines from all IF bands by shifting these maser lines to the same position with the task UVSUB, and then combined them with the task VBGLU before running CALIB to get the phase solutions.

After the above calibrations, we discarded the phase solutions and the maser data in the time intervals within which the solutions appeared to be randomly scattered in time or had adjacent reference phases exceeding $\sim 50^\circ$. The phase solutions were then interpolated and applied to all the maser data. In all phase-referencing observations for NGC 6323, we performed an extra step of self-calibration after the initial phase-referencing calibration, because the phase-referencing calibration alone did not give adequate phase calibration, and significant sidelobes were still visible after CLEAN deconvolution.

We combined the calibrated data from multiple tracks of a single source differently before imaging according to whether we are measuring black hole (BH) mass or maser distance. For measuring black hole masses (Chapter 3), we simply combined and averaged all the datasets we have for each source before making the image because BH mass only depends on the positions and velocities of high velocity masers if the disk is nearly edge-on and HV masers reside very close to the midline of the disk. Errors from combining masers with different accelerations are negligible in the BH mass measurement. On the other hand, for distance measurements of NGC 6264 and NGC 6323 (Chapter 4 & 5), we only combined the datasets in the u-v space if they were observed within a relatively short interval (e.g. 1−6 months) and if there was evidence that the masers in these datasets have the same accelerations. We did this because distance measurement is very sensitive to the actual accelerations of systemic masers, and if we combine maser lines that have different accelerations and come from different regions of the maser disk, we will very likely have a systematic offset in the distance measurement that is hard to correct. In addition, due to the variability of the systemic masers, combining datasets in the u-v plane may not give the best sensitivity for distance measurement. While we did not combine all datasets for distance measurement at once in the u-v space, we did use all the maser spots with accurate accelerations in the distance determination to minimisze the statistical error.

After combining data in the u-v space, we Fourier transformed the gridded (u, v) data to make images of the masers in all spectral channels of the IF bands that showed maser lines, and we deconvolved the images using CLEAN with a weighting scheme that optimized the position accuracy (e.g. ROBUST = 0 in the task IMAGR). We fitted the detected maser spots with elliptical Gaussians to obtain the positions and flux densities of individual maser components. In Table 2.3 we show a representative dataset that includes the velocities, positions, and peak intensities of the maser spots in NGC 6264. The data for all galaxies are available in the electronic version of Kuo et al. (2011). Note that all galaxies except NGC 4388 and NGC 2273 have at least 2 tracks of data. Therefore, the peak flux in Table 2.3 is the flux for the averaged dataset. The actual fluxes in an individual epoch can be higher or lower because of variability of the masers.

2.5 Relativistic Velocity Assignment

The sub-parsec megamaser disks presented in this paper are in a deep gravitational potential and the majority have recession velocities over 1% of the speed of light c. For this reason, we made both special and general relativistic corrections to the maser

Table 2.3. Sample data for NGC 6264

V_{op}[a] (km s^{-1})	RA[b] (mas)	δRA[b] (mas)	Decl.[b] (mas)	δDEC[b] (mas)	F_ν[c] (mJy/B)	σ_F[c] (mJy/B)
10918.33	0.399	0.008	−0.021	0.018	6.0	0.3
10914.71	0.407	0.010	−0.001	0.021	4.8	0.3
10911.09	0.401	0.005	0.000	0.011	10.2	0.4
10907.47	0.397	0.013	0.041	0.029	3.7	0.3
10903.85	0.395	0.011	−0.050	0.027	3.8	0.4
10900.23	0.388	0.009	0.044	0.022	4.6	0.3
10885.74	0.369	0.019	0.053	0.038	2.6	0.4
10871.26	0.400	0.018	0.061	0.037	2.9	0.3
10856.77	0.467	0.011	−0.038	0.029	3.8	0.3
10853.15	0.484	0.005	−0.038	0.011	9.7	0.4
10849.53	0.490	0.005	−0.006	0.011	9.4	0.3
10845.91	0.492	0.002	−0.016	0.006	18.3	0.4
10842.29	0.494	0.002	−0.005	0.005	24.4	0.4
10838.67	0.505	0.004	−0.010	0.009	11.7	0.4
10835.05	0.543	0.012	−0.094	0.032	3.5	0.4
10831.43	0.542	0.017	−0.039	0.031	3.1	0.3
10827.81	0.518	0.012	−0.101	0.027	3.9	0.3
10824.19	0.533	0.007	−0.040	0.016	6.9	0.4
10820.56	0.493	0.012	−0.041	0.026	3.8	0.3

Note. — Sample of data for NGC 6264. The entirety of data for all galaxies is available in the electronic version.

[a] Velocity referenced to the LSR and using the optical definition (no relativistic corrections).

[b] East-west and north-south position offsets and uncertainties measured relative to the average position of the systemic masers in the VLBI map (Figure 3.2 in Chapter 3). Position uncertainties reflect fitted random errors only. In NGC 1194 and NGC 2960, there may be additional uncertainties caused by the poorer tropospheric delay calibrations due to their low declinations (low elevations during the observations).

[c] Fitted peak intensity and its uncertainty in mJy beam^{-1}.

velocities in the data before we used the data to analyze the BH masses. We made the relativistic corrections in the following way[6]:

The observed Local Standard of Rest velocities $V_{\rm op}$ listed in Table 2.3 are based on the "optical" velocity convention

$$\frac{V_{\rm op}}{c} = \left(\frac{\nu_0 - \nu}{\nu}\right) , \tag{2.2}$$

where ν is the observed frequency and $\nu_0 = 22.23508$ GHz, the rest frequency of the H_2O $6_{16} - 5_{23}$ transition.

Because of gravitational time dilation, the emitting frequency ν_0 of a maser at distance r from a compact object of mass M and the actual observed frequency ν_∞ for an observer at $r = \infty$ differ by a factor

$$\frac{\nu_0}{\nu_\infty} = \left(1 + \frac{GM}{rc^2}\right) . \tag{2.3}$$

For a maser in a circular orbit moving at speed $\beta_{\rm m}c$, balancing the gravitational and centripetal accelerations gives $GM/r^2 = (\beta_{\rm m}c)^2/r$, so

$$\frac{\nu_0}{\nu_\infty} = 1 + \beta_{\rm m}^2 . \tag{2.4}$$

We multiplied the observed frequency ν of each maser line by $(1 + \beta_{\rm m}^2)$ to correct for gravitational time dilation.

The megamaser lines at the systemic velocities were also corrected for a transverse Doppler shift

$$\frac{\nu_0}{\nu} = 1 + \beta_{\rm m}^2/2 . \tag{2.5}$$

---

[6] The description of relativistic corrections in this section and the actual corrections in the BH mass determination are contributed by Jim Condon from the NRAO.

The relativistically correct Doppler equation for a source moving radially away with velocity $v = \beta c$ is

$$\frac{\nu}{\nu_0} = \left(\frac{1-\beta}{1+\beta}\right)^{1/2} . \tag{2.6}$$

After the observed frequency had been corrected for the gravitational time dilation and transverse Doppler shift, we used Equation 2.6 to convert the corrected frequency to its relativistically correct radial velocity $v = \beta c$. For the megamaser disks, typically $\beta_{\rm m} < 0.003$. So, for galaxies in the Hubble flow ($z > 0.01$), the general relativistic corrections are smaller than the special relativistic corrections. For example, for masers in UGC 3789, which has an optical-LSR recession velocity of 3262 km $\rm s^{-1}$, the special relativistic corrections range from 10 to 26 km $\rm s^{-1}$ whereas the general relativistic corrections range from 0 to ~ 2 km $\rm s^{-1}$.

Finally, when fitting the rotation curves, we used the relativistic formula for the addition of velocities to decompose the observed β value of each maser spot into a common $\beta_{\rm g}$ associated with the radial velocity of the center of each megamaser disk and an individual $\beta_{\rm m}$ associated with orbital motion of a specific maser spot. The redshifted maser spots have $\beta_{\rm m} > 0$ and blueshifted maser spots have $\beta_{\rm m} < 0$.

$$\beta = \frac{\beta_{\rm g} + \beta_{\rm m}}{1 + \beta_{\rm g}\beta_{\rm m}} . \tag{2.7}$$

Chapter 3

BH mass measurement and the M_{BH}-σ relation

In our endeavor to determine an accurate Hubble constant in the Megamaser Cosmology Project, we measure direct angular-diameter distances to galaxies in the Hubble flow with the H_2O megamaser technique. This technique involves sub-milliarcsecond resolution imaging and acceleration measurements of H_2O megamasers from nearly edge-on, sub-parsec gas disks at the centers of active galaxies (Chapter 1). Since the maser disk is usually significantly smaller than the "gravitational sphere of influence" (Barth 2003) of the black hole (BH) at the center, the kinematics of the water masers provide a direct probe of the gravitational potential of the BH, and the BH mass can be measured with high precision from the rotation curve of the maser disk. Measuring BH masses is therefore a second important product of this project in addition to the distance determination. While we still need acceleration measurements for H_2O masers to determine distances, the VLBI imaging alone is sufficient to measure accurate central BH masses. These BH masses will provide an important basis for testing the M_{BH}-σ relation. In section 3.1 of this chapter, we will first give a brief review on the current status and methods for BH mass determination. In section 3.2, we present the VLBI images and rotation curves of the megamasers, followed by our analysis of BH masses. In section 3.3, we will show that the central objects of the maser disks presented in this chapter can be best explained by supermassive BHs. In section 3.4, the main discussion is on how we can use the maser BH masses to test and calibrate an important BH searching technique. In section 3.5, the implications of our new maser BH masses for the M_{BH}-σ relation are presented. Finally, we summarize the main points of this Chapter in section 3.6.

3.1 Current Status and Methods for BH Mass Determination

There has been substantial progress in detecting SMBHs and constraining their masses over the past two decades. (see reviews in Kormendy & Richstone 1995; Kormendy & Gebhardt 2001; Kormendy 2004). This rapid progress was mainly facilitated by the high angular resolution provided by HST, and by gradually maturing techniques in modeling stellar dynamics of galaxies. The number of BH detections has increased to the degree that the field has shifted from confirming the existence of SMBHs to studying BH demographics, mainly BH-bulge relations. One of the most significant relations found between BHs and galactic properties at large scales is the tight correlation between BH mass and effective velocity dispersion of bulges of galaxies (The M_{BH}-σ relation; Ferrarese & Merritt 2000; Gebhardt et al. 2000; Gültekin et al. 2009 references therein). The most important implications of this relation are that supermassive black holes are ubiquitous components in all bulge-dominated galaxies and galaxy evolution may be intimately connected with the growth of supermassive black holes. While there seems to be a tight M_{BH}-σ correlation in the current limited sample, it is still important to examine the correlation critically with more accurate measurements of BH masses with small systematic errors to see if the M_{BH}-σ relation still holds.

The primary methods of determining BH masses over the past two decades include using dynamics of either bulge stars (e.g. Kormendy & Richstone 1995; Gebhardt et al. 2000a;Gebhardt et al. 2003; Siopis et al. 2009) or of a 100 pc-scale ionized gas disk (e.g. Barth et al. 2001; Sarzi et al. 2001) to trace the mass contents in a galaxy. In modeling with stellar dynamics, although the modeling techniques have improved quite significantly from the simple isotropic model (Young et al. 1978; Sargent et al. 1978; Tonry 1984; van der Marel 1994) to the two-integral model (e.g. Magorrian et al. 1998), and to the current more general axisymmetric three-integral models (e.g. Van der Marel 1998; Cretton et al. 1999; Gebhardt et al. 2000a; Siopis et al. 2009), systematic errors of a factor of a few could still remain. Gebhardt & Thomas (2009) show that dynamical models that do not include the contribution from the dark matter halo may produce a biased result for the BH mass. This poses an issue for previous work on measuring BH masses from elliptical galaxies, of which the dark matter halos are significant components. In addition, how much the BH mass can change by generalizing the model to include triaxiality still needs to be explored (van den Bosch & de Zeeuw 2010; Shen & Gebhardt 2010). In gas-dynamical modeling, the main systematic concern is the unknown nature of the large intrinsic velocity dispersion of some gas near the central region of a galaxy (Kormendy & Gebhardt 2001; Barth et al. 2001). If this orginates from pressure support, then the observed orbital velocity will be slower than the true circular velocity (the so-called "symmetric drift"), and the BH mass will be underestimated. Nonetheless, the gas-dynamical BH masses are thought to be accurate to ∼30% in the best cases (Kormendy & Gebhardt 2001; Barth et al. 2001).

Reverberation mapping (Blanford & McKee 1982; Peterson et al. 2004) and virial mass estimation (Greene & Ho 2006) are also often used to measure BH masses in type 1 AGNs. They are the only two methods that do not depend on high angular resolution, and hence can be applied to very distant objects (Peterson et al. 2004). The two methods measure the BH mass with the following equation:

$$M_{BH} = \frac{f R_{BLR} \sigma_{line}^2}{G} \ , \tag{3.1}$$

where f is a factor depending on the structure, kinematics, and orientation of the broad-line region (BLR); R_{BLR} is the size of the BLR, σ_{line} is the gas velocity dispersion of the BLR which is proportional to the linewidths of broad-line gas emissions, and G is the gravitational constant. The reverberation mapping method deduces R_{BLR} by measuring the time delays between continuum and emission-line variations whereas the virial estimation method uses the continnum luminosity $\lambda L_\lambda(5100\mathring{A})$ to estimate the size of the BLR via the $\lambda L_\lambda(5100\mathring{A}) - R_{BLR}$ correlation (e.g. Kaspi et al. 2000), which itself is based on reverberation mapping BH masses. The virial estimation method can thus be said to be a secondary reverberation mapping method.

The primary systematic concern of these two methods is the uncertain absolute scale of the BH masses, the factor f in Equation 3.1. One usually determines f by making assumptions on the structure, kinematics, and orientation of the BLR (Netzer 1990), or by normalizing the reverberation-mapping M_{BH}-σ relation to the M_{BH}-σ relation from the dynamical methods (Onken et al. 2004). In section 5, we will discuss whether it is possible to use maser BH masses to calibrate the absolute scale of BH masses obtained from the virial estimation method.

In recent years, spectral analysis of X-ray emitting, early-type galaxies was also used to measure BH masses (Humphrey et al. 2009). One can infer the mass profile of a galaxy from its gas density and temperature distribution, and the BH mass can be measured by removing mass contributions from stars and dark matter. In principle, the accuracy of the BH mass depends only on the assumption of hydrostatic equilibrium of the X-ray emitting gas. While Humprey et al. (2009) argue that the deviation from hydrostatic equilibrium is relatively small ($\lesssim 15\%$), there is a discrepancy between the BH mass and dynamical mass profile in NGC 4649, which is studied by both the X-ray method and stellar-dynamical modeling (Shen & Gebhardt 2010). Whether this implies some hidden systematic errors in either or both methods still needs further investigation.

A proven method to measure highly accurate BH masses involves sub-milliarcsecond resolution imaging of H_2O maser emission from sub-parsec circumnuclear disks at the center of active galaxies, a technique established by the study of NGC 4258 with VLBI (Miyoshi et al. 1995; Herrnstein et al. 1999). The VLBI technique plays a crucial role in measuring BH masses with high precision because its angular resolution is two orders of magnitude higher than the best optical resolution. For any given galaxy with a nearly constant central mass density of stars, $M_{\rm BH}$ is proportional to $R_{\rm inf}^3$, where $R_{\rm inf}$ is the radius of the gravitational sphere of influence of the BH (Barth 2003). So, a factor of 100 increase in resolution permits measurements of masses up to 10^6 times smaller. Similarly, the central density limits that can be set are up to 10^6 times higher, high enough to rule out extremely dense star clusters as the dominant central mass based on dynamical arguments (see section 3.3) in most megamaser disks presented here.

In addition to the high angular resolution provided by VLBI, the small size and simple dynamical structure of maser disks are also key to measuring precise BH masses. Megamaser disks, such as the archetypal one in NGC 4258, are usually found in the centers of Seyfert 2 galaxies. Because maser emission is beamed and long path lengths are required for strong maser amplification, the megamaser disks are observable only if the the disk is close to edge-on. In NGC 4258 the disk is inclined ∼82° and its rotation curve is Keplerian to better than 1% accuracy, which makes the BH mass determination robust with very few assumptions. The megamaser disks are typically smaller (r ∼0.2 pc in NGC 4258) than the gravitational sphere of influence of their supermassive black holes ($r \sim 1$ pc in NGC 4258); this guarantees that the gravitational potential is dominated by the central mass.

The megamaser disk method for estimating BH masses has some practical limitations. First, finding megamaser disks is difficult, partly because detectable disks need to be nearly edge-on. Only eight BH masses have been published based on measurements of megamasers : NGC 1068 (Greenhill et al. 1996), NGC 2960 (Mrk 1419) (Henkel et al. 2002; not based on VLBI), NGC 3079 (Kondratko et al. 2005), NGC 3393 (Kondratko et al. 2008), UGC 3789 (Reid et al. 2009a; MCP paper I), NGC 4258 (Herrnstein et al. 1999), NGC 4945 (Greenhill et al. 1997), and Circinus (Greenhill et al. 2003). Second, some rotation curves are significantly flatter than Keplerian, e.g. NGC 1068; NGC 3079; and IC 1481 (Mamyoda et al. 2009). The origin of the flatter rotation curves in these galaxies is unclear. It could be caused by self-gravity of a massive disk or the presence of a nuclear cluster, in which case the enclosed mass would be larger than the BH mass, or it could be caused by radiation pressure, in which case the enclosed mass would be smaller than the BH mass (Lodato & Bertin 2003). Without fully understanding the causes of the flatter rotation curves and correctly modeling these megamaser disks, accurate BH mass measurement would be difficult. Therefore, the key to measuring reliable BH masses is to find well-defined, edge-on megamaser disks with Keplerian rotation curves.

3.2 Results

3.2.1 VLBI Images, Rotation Curves, and BH Masses

Figure 3.1 shows GBT single-dish spectra for all megamaser galaxies presented here except for UGC 3789, which can be found in Reid et al. (2009). Figures 3.2, 3.3, and 3.4 show the VLBI maps and the position-velocity ($P - V$) diagrams along with the fitted rotation curves of the maser spectral components (spots) in UGC 3789, NGC 1194, NGC 2273, NGC 2960 (Mrk 1419), NGC 4388, NGC 6264, and NGC 6323. Reid et al. (2009) published the UGC 3789 VLBI map and the rotation curve, and we performed a new analysis of the BH mass for this galaxy based on those data. We show the VLBI map and rotation curve for this galaxy again for direct comparison with the other six megamaser disks. The data points in the VLBI maps and rotation curves are color-coded to indicate redshifted, blueshifted, and systemic masers, where the "systemic" masers refer to the maser spectral components having velocities close to the systemic velocity of the galaxy. Except for NGC 4388, the maser spot distributions are plotted relative to the average position of the systemic masers. Systemic masers are not detected in NGC 4388, so we plotted its maser distribution relative to the dynamical center determined from fitting the data in the $P - V$ diagram with a Keplerian rotation curve.

To estimate the inclination and dynamical center (i.e. the position of the BH) of each disk, we rotated the coordinate system to make the disk horizontal and used the fitted horizontal line that passes through the high velocity masers as the zero point of the y-coordinate of the dynamical center (see Figures 3.3 & 3.4). The zero point of the x-coordinate is defined to be the unweighted average $\theta_{\rm x}$ of the systemic masers.

We assumed that the systemic masers have about the same orbital radii as the high-velocity masers to estimate the maser disk inclination $\cos^{-1}(\langle\theta_{\rm y}^{(sys)}\rangle/\theta_{\rm r})$, where $\langle\theta_{\rm y}^{(sys)}\rangle$ is the average $\theta_{\rm y}$ position of the systemic masers and $\theta_{\rm r}$ is the orbital radius of the systemic masers. In principle, one can determine $\theta_{\rm r}$ exactly only when good rotation curves for both systemic and high-velocity masers can be obtained, and precise acceleration measurements for the systemic masers are available. Among our data we only have such information for UGC 3789 at this point (Braatz et al. 2010), and so we use $\langle\theta_{\rm x}\rangle$ of high velocity masers as an estimate of $\theta_{\rm r}$. We note that all our megamaser disks with systemic masers detected have inclinations larger than 80°, so assuming the disk is exactly edge-on will only cause errors less than 1% in the derived BH masses. In NGC 4388 we could not measure a disk inclination, but even if the disk were 20° from edge-on, the contribution to the error in the BH mass would be only 12%.

We determined the rotation curve for each megamaser disk as a function of the "impact parameter" defined as the projected radial offset $\theta = (\theta_{\rm x}^2 + \theta_{\rm y}^2)^{1/2}$ of the maser spots so that we can account for the warped structures in some megamaser disks. We then performed a nonlinear least-squares fit of a Keplerian rotation curve to the position-velocity diagram with the assumption that the high-velocity masers lie exactly on the mid-line of the disk. In addition, the systemic velocity of each galaxy was fitted as a free parameter, and we report the best fits of the systemic velocities of our megamaser galaxies in Table 2.1 in Chapter 2.

The fitted Keplerian rotation curves can be expressed in the following form:

$$|v_{\rm K}| = v_1 \Big(\frac{\theta}{1\ {\rm mas}}\Big)^{-1/2}, \tag{3.2}$$

where $|v_{\rm K}|$ is the orbital velocity (after relativistic corrections) of the high velocity masers and v_1 is the orbital velocity at a radius 1 mas from the dynamical center. The BH mass is

$$M_\bullet = \Big(\frac{|v_{\rm K}|^2\theta}{G}\Big) D_{\rm A} \ = \Big(\frac{\pi v_1^2}{6.48 \times 10^8 G}\Big) D_{\rm A}\ , \tag{3.3}$$

where D_A is the angular diameter distance to the galaxy. We show all the measured BH masses in Table 3.1.

3.2.2 The Error Budget For the BH Mass

There are primarily three sources of error for our BH mass calculation, and the largest comes from the distance uncertainty. Except for NGC 4388, we used the Hubble flow distances (relative to the 3K CMB) from NASA/IPAC Extragalactic Database (NED) for a cosmological model with $H_0 = 73$ km s^{-1} Mpc^{-1}, $\Omega_{\rm matter} = 0.27$ and $\Omega_\Lambda = 0.73$. These distances have an error about 6% (assuming the error from the peculiar velocity of the galaxy is negligible), caused by the uncertainty of the latest Hubble constant measurements (Freedman & Madore 2010; Riess et al. 2009). Since NGC 4388 is in the Virgo cluster and has a large peculiar velocity, the Hubble distance can have significant uncertainty. Therefore, we adopted its Tully-Fisher distance of 19 Mpc, which has an error about 11% (Russell 2002).

The second source of BH mass uncertainty comes from fitting the rotation curves of the masers. In our Keplerian fitting, the rms σ_θ of the observed position offsets from Keplerian rotation is usually larger than the rms position uncertainties of the data by a factor of 1.5 to 4. This extra scatter can lead to a systematically differ-

Table 3.1. The BH Masses and Basic Properties of the Maser Disks

Name	Dist. (Mpc)	BH mass (10^7 M$_\odot$)	Disk Size (pc)	P.A. (°)	Incl. (°)	r$_c$ (pc)	ρ_0 (M$_\odot$ pc^{-3})	$m_{\rm max}$ (M$_\odot$)	$T_{\rm age}$ (yr)	$R_{\rm inf}$ (arcsec)
NGC 1194	53.2	6.5±0.3	0.54-1.33	157	85	0.260	1.2×10^{9}	13	$>1.0\times10^{10}$	0.033
NGC 2273	25.7	0.75±0.04	0.028-0.084	153	84	0.015	6.1×10^{11}	0.05	$<2.2\times10^{6}$	0.010
UGC 3789	46.4	1.04±0.05	0.084-0.30	41	>88	0.022	2.3×10^{11}	0.1	$<1.8\times10^{7}$	0.010
NGC 2960	72.2	1.16±0.05	0.13-0.37	−131	89	0.056	1.7×10^{10}	0.48	$<1.0\times10^{9}$	0.005
NGC 4388	19.0	0.84±0.02	0.24-0.29	107	–	0.090	3.3×10^{9}	0.9	$<6.6\times10^{9}$	0.034
NGC 6264	139.4	2.91±0.04	0.24-0.80	−85	90	0.085	1.2×10^{10}	1.4	$>1.0\times10^{10}$	0.012
NGC 6323	106.0	0.94±0.01	0.13-0.30	10	89	0.046	2.3×10^{10}	0.3	$<4.7\times10^{8}$	0.003

Note. — Col(1): Galaxy name; Col(2): The Hubble flow distances we adopt from NED; Col(3): Black hole masses measured in our project. The mass uncertainty here only includes errors caused by source position uncertainty and from fitting a Keplerian rotation curve for a given distance. Except for NGC 4388, the actual BH mass uncertainty is dominated by the error of the latest H_0 measurement ($\sim$ 6%). NGC 4388 has a larger BH mass error (11%) which is limited by the uncertainty of the Tully-Fisher distance determination (see the explanation in section 3.2); Col(4): Sizes of the inner and outer edge of the maser disks; Col(5): Position angle (PA) of the disk plane measured east of north. PA equals zero when the blueshifted side of the disk plane has zero East offset and positive North offset; Col(6): Inclination of the maser disk. Note that the inclination of NGC 4388 is unconstrained because we did not detect systemic masers; Col(7): The core radius of the Plummer cluster in parsecs. For NGC 1194, NGC 2273, NGC 2960, and NGC 4388, the core radii are derived from Equation 3.7. For UGC 3789, NGC 6264, and NGC 6323, the radii are derived from the Plummer rotation curve fitting; Col(8): The central mass density of the Plummer cluster $\rho_0 = 3M_\infty/4\pi r_c^3$. Here, M_∞ is obtained from the Plummer rotation curve fitting ; Col(9): The maximum stellar mass of the Plummer cluster below which the cluster will not evaporate in less than 10 Gyr. In all cases except NGC 1194, a cluster of neutron stars can be directly ruled out because m$_{\rm max}$ is less than $\approx$ 1.4 M$_\odot$; Col(10): Lifetime ($T_{\rm age}$) of a cluster. The values shown here are limited by the collision timescale, which is the maximum lifetime of the cluster composed of either main-sequence stars, brown dwarfs, white dwarfs, or neutrons stars; Col(11) The radius of the gravitational sphere of influence for the maser BHs in arcsec. We calculate R_{inf} using Equation 1 of Barth (2003) with the bulge velocity dispersion measurements from Green et al. (2010).

ent position of the dynamical center, and hence a slightly different BH mass if we allow the dynamical center position to be a free parameter in the fit. This excess may indicate that we underestimated our observational errors or it may indicate genuine deviations from our simple model, possibly caused by peculiar motions of the masers (e.g. perturbations from spiral density waves) or high-velocity masers not lying precisely on the mid-line of the disk (Humpreys et al. 2008). If the latter is the main cause of deviation, we estimate that the majority of the maser spots fall within $\approx 7^\circ - 10^\circ$ from the midline of the disk based on Monte Carlo simulations.

In addition to the deviations of the masers from the midline of the maser disk, there is also an error in the BH mass from the uncertainty of the position of the BH in the fitting. To estimate this error, we relax our assumption on the position of the BH, and allow it to be a free parameter in the fitting. However, since the recession velocity of the galaxy (v_0) and the position of the BH are correlated in this case, we impose a constraint on the possible positions of the BH such that the fitted v_0 does not exceed v_0 determined from other methods (e.g. HI measurements) beyond their error bars. Including all possible errors mentioned above, we estimate the total fitting error in BH mass to be $1\%-5\%$ depending on the galaxy.

The third source of error is from the absolute position errors of our megamasers. Source position errors introduce an extra phase difference between maser spots having different frequencies (velocities). The relative position errors scale with velocity offset from the reference maser feature (Argon et al. 2007; Greenhill et al. 1993), which may differ from source to source. Since the BH mass is proportional to the size of the maser orbits, relative position shifts among masers introduce errors in the BH mass measurements. Among our megamasers, UGC 3789, NGC 2960, and NGC 2273 have the largest absolute position errors (10 mas; see Note (h) in Table 2.1). The resultant

BH mass errors are $3 - 5\%$, whereas this error is smaller than 0.3% in the other megamaser galaxies. Note that the error for the BH mass discussed in the following subsections does not include the distance uncertainty. Only source position errors and errors from Keplerian fitting are evaluated, which is the best approach for comparing our results with BH masses derived from other techniques, since the same distance can be used for comparison. As the distance uncertainties shrink in the future, so will the uncertainties in our BH masses.

3.2.3 Notes On Individual Galaxies

NGC 1194

NGC 1194[1] hosts a Seyfert 1.9 nucleus and has a distance of ≈ 52 Mpc. The position angle of the maser disk (Figure 3.2) is 157° and the inclination is $\approx 85°$. NGC 1194 has the largest maser disk among the megamasers presented here, with an inner and outer radius of 0.54 and 1.33 pc, respectively. The blueshifted and redshifted masers do not appear to fall exactly on a straight line on the sky, but they are consistent with a slightly bent thin disk. The rotation curve (Figure 3.3) is consistent with Keplerian rotation, and the measured BH mass is $(6.5 \pm 0.3) \times 10^7 M_\odot$, the largest among the BH masses studied here.

NGC 2273

NGC 2273 is a Seyfert 2 galaxy at a distance of ≈ 26 Mpc. The position angle of the maser disk (Figure 3.2) is 153° with an inclination of $\approx 84°$. The inner and outer radii of the disk are 0.028 and 0.084 pc, respectively. The maser distribution shows a hint

---

[1] The VLBI data reduction for this galaxy was mainly done by Ingyin Zaw from New York University in Abu Dhabi. The role of the author of this thesis for this galaxy was to assist the data reduction process.

of a warped disk. The rotation curve (Figure 3.3) is also consistent with Keplerian rotation to within the errors. The BH mass we obtain is $(7.5 \pm 0.4) \times 10^6 M_\odot$.

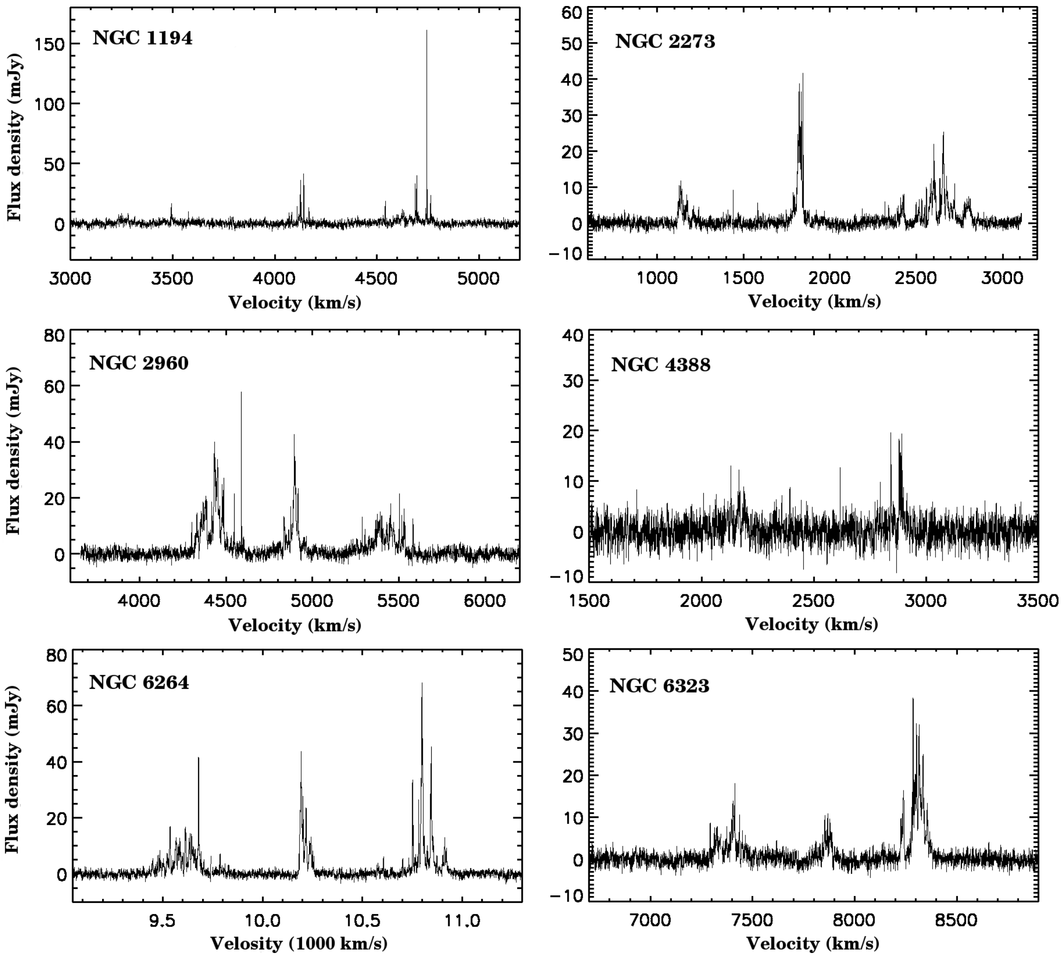

Fig. 3.1.— Characteristic H_2O maser spectra. The x-axis shows LSR velocities based on the optical definition. Flux densities of masers can vary significantly, so the spectra shown here are just representative for particular epochs: January 13 2008 for NGC 1194; February 21 2009 for NGC 2273; April 2 2009 for NGC 2960 (Mrk 1419); November 30 2005 for NGC 4388; March 31 2009 for NGC 6264; and April 6 2000 for NGC 6323.

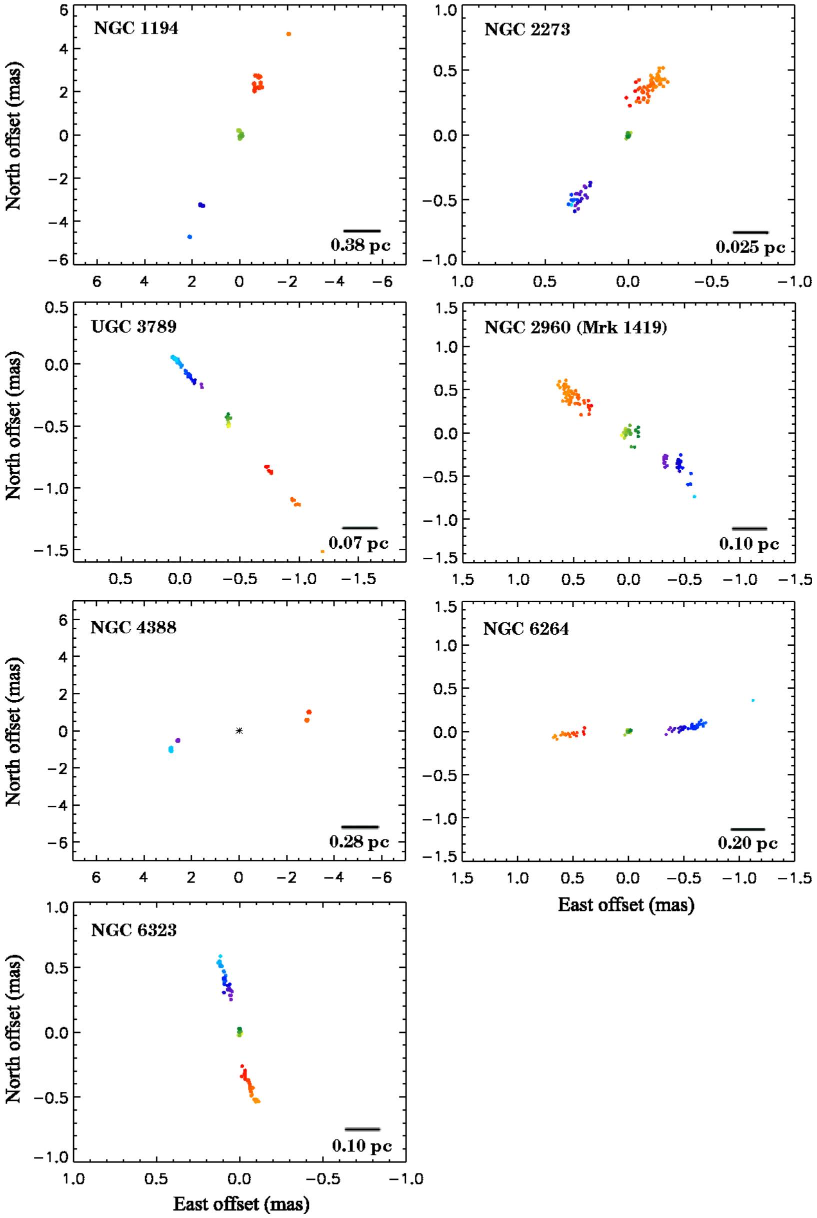

Fig. 3.2.— VLBI maps for the seven 22 GHz H_2O masers megamasers analyzed. The maps are color-coded to indicate redshifted, blueshifted, and systemic masers, where the "systemic" masers refer to the maser components having recessional velocities close to the systemic velocity of the galaxy. Except NGC 4388, maser distributions are plotted relative to the average position of the systemic masers. For NGC 4388, in which the systemic masers are not detected, we plot the maser distribution relative to the dynamical center determined by fitting the high velocity features with a Keplerian rotation curve.

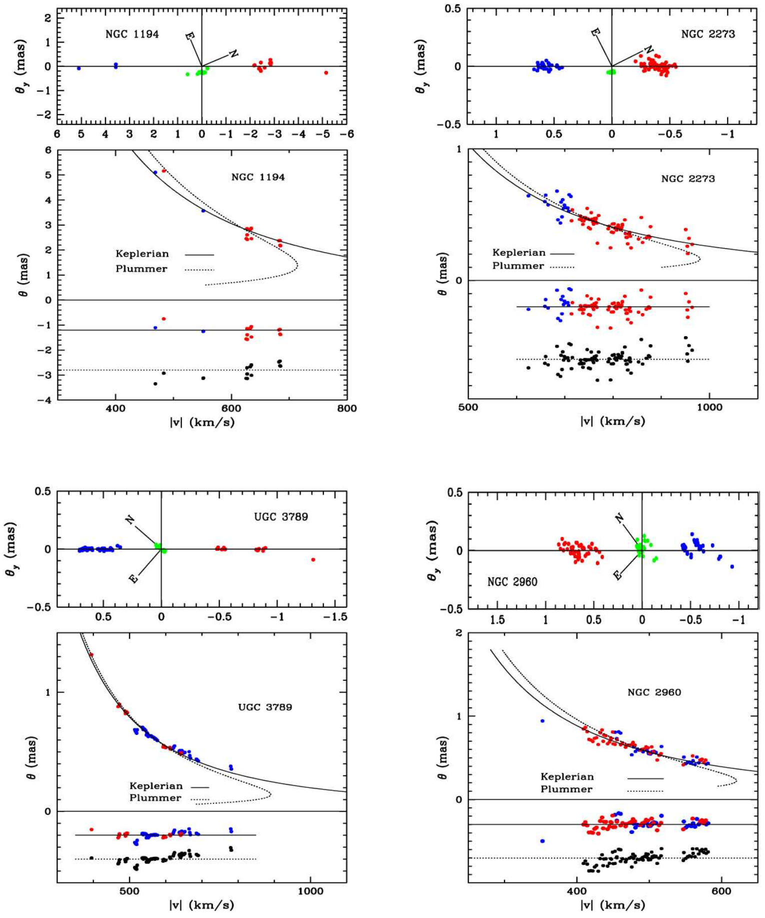

Fig. 3.3.— Maser distributions (top panels) and rotation curves (bottom panels) for NGC 1194 , NGC 2273, UGC 3789, and NGC 2960. The maser distribution has been rotated to horizontal to show the scatter in the maser positions and the offset of the systemic masers from the plane defined by high-velocity masers more clearly. The coordinate system is chosen to place the centroid of the high-velocity maser disk (blue and red points) at $\theta_{\mathrm{y}} = 0$ and the centroid of the systemic masers (green points) at $\theta_{\mathrm{x}} = 0$. The axes for the maps show relative position in milliarcseconds, and North (N) and East (E) are indicated by directional arrows on each map. The bottom panel for each galaxy shows the rotation curves of the redshifted and blueshifted masers (red and blue points on the curves) plotted with the best-fit Keplerian (solid curve) and Plummer (dotted curve) rotation curves. The velocities shown in the figure are the LSR velocities after the special and general relativistic corrections. The residuals (data minus Keplerian curve in red and blue; data minus Plummer curve in black) are in the bottom part of each figure. Note that we plot the rotation curve with the impact parameter θ (mas) as the ordinate and rotation speed $|v|$ (km s^{-1}) as the abscissa for the convenience of fitting.

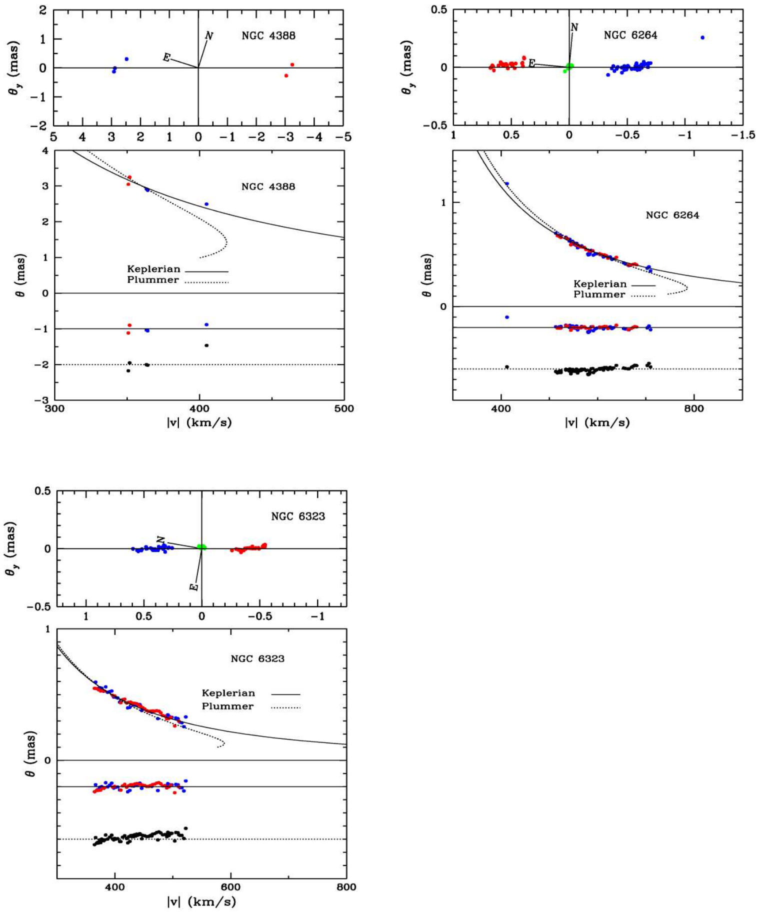

Fig. 3.4.— Maser distributions (Top panel) and rotation curves (Bottom panel) for NGC 4388 , NGC 6264, and NGC 6323. Please refer to the caption of Figure 3.3 for the description of this figure.

UGC 3789

UGC 3789 is a Seyfert 2 galaxy at a distance of ≈ 50 Mpc (Reid et al. 2009a; Braatz et al. 2010). Its edge-on maser disk lies at position angle 41° East of North (Fig. 3.2). Although the high-velocity masers appear to trace a flat disk, the misalignment of the systemic masers with respect to the disk and the fact that the systemic masers have at least two distinct centripetal accelerations (Braatz et al. 2010) suggest that the disk is probably warped along the line of sight. The inner and outer radii of the disk are 0.084 and 0.30 pc, respectively. Fitting the $P-V$ diagram (Fig. 3.3) with a Keplerian rotation curve gives a BH mass of $(1.04 \pm 0.05) \times 10^7 M_\odot$.

NGC 2960 (Mrk 1419)

NGC 2960[2] hosts a LINER nucleus at a distance of ≈ 71 Mpc. The position angle of the maser disk (Fig. 3.2) is $-131°$ and the inclination is $\approx 89°$. The outer parts of the disk show some warping. The inner and outer radii of the disk are 0.13 and 0.37 pc, respectively. The rms scatter of the high velocity masers normal to the disk is $\sigma_\perp = 71\,\mu$arcsec, which is 1.6 times larger than the rms uncertainty of the data, so it is likely that either we underestimated the observational uncertainties because of larger tropospheric delay errors for low declination sources, or the thickness of the disk may not be negligible in this megamaser. In this galaxy, we measure a BH mass of $(1.16 \pm 0.05) \times 10^7 M_\odot$.

NGC 4388

NGC 4388 is in the Virgo cluster and we adopted a Tully-Fisher distance of 19 Mpc; it is the nearest of the seven galaxies presented here. It hosts a Seyfert 2

---

[2] The VLBI data reduction for this galaxy was mainly done by Violetta Impellizzeri from NRAO. The role of the author of this thesis for this galaxy was to assist the data reduction process.

nucleus and the maser disk (Figure 3.2) has a position angle of 107°. We cannot measure the inclination directly because no systemic masers were detected. As with the other megamasers, we assumed a flat, edge-on disk. Since no systemic masers were detected, we determined the position of the dynamical center by allowing it to be a free parameter when fitting the high-velocity masers with a Keplerian rotation curve (Fig. 3.4). In addition, we fixed the systemic velocity of the galaxy using an HI measurement (Lu et al. 2003). The resulting BH mass is $(8.5 \pm 0.2) \times 10^6 M_\odot$. With only five maser spots mapped, there is not sufficient data to demonstrate Keplerian rotation or even to show that the masers actually lie on a disk. We argue that it is likely they do because the radio continuum jet shown by Kukula et al. (1995) is nearly perpendicular to the line joining the blueshifted and redshifted masers. However, because of these uncertainties, the BH mass for NGC 4388 should be used with some caution until better data are obtained.

NGC 6264

At $\approx$ 139 Mpc, NGC 6264[3] (Figure 3.2) is the most distant object in our current sample. The disk is slightly warped and is consistent with a thin disk given the uncertainties in the position measurement. The disk has a position angle of $-85°$ and an inclination of $\approx 90°$. The inner and outer radii of the disk are 0.24 and 0.80 pc, respectively. In the $P-V$ diagram (Fig. 3.4), the high velocity masers beautifully trace the Keplerian rotation curve, and we obtain a BH mass of $(2.91 \pm 0.04) \times 10^7 M_\odot$.

---

[3] The analysis and results for this galaxy presented in this chapter were based the VLBI observations BB261F and BB261H. The observations BB261K and BB261Q were not included in the analysis because they were observed after the analysis shown here was done.

NGC 6323

NGC 6323 is a Seyfert 2 galaxy at a distance of $\approx$ 105 Mpc. The VLBI image (Fig. 3.2) shows a remarkably thin disk at a position angle of 10° and inclination of $\approx 89^\circ$. The disk is apparently warped, and the inner and outer radii are 0.13 and 0.3 pc, respectively. The rotation curve of the high-velocity masers (Figure 3.4) is Keplerian, and we obtain a BH mass of $(9.4 \pm 0.1) \times 10^6 M_\odot$.

3.2.4 Search For Continuum Emission

We searched for continuum emission from the vicinity of the supermassive BH (i.e., near the systemic masers) in our megamaser galaxies by averaging the line-free spectral channels in our data and imaging with natural weighting to maximize the detection sensitivity. We detected no continuum emission in all megamaser galaxies presented in this paper. The channels averaged, the center velocities of the bands used for averaging, and the continuum upper limits are listed in Table 3.2.

3.3 A Supermassive Black Hole or a Central Cluster of Stars or Stellar Remnants ?

The question[4] of whether the mass enclosed by an H_2O megamaser disk is dominated by a central point mass or a compact cluster of stars or stellar remnants was first addressed by Maoz (1995) & Maoz (1998). The main argument is that if the lifetime of a central cluster, limited by evaporation or collision timescales, is significantly shorter than the age of its host galaxy, then it is unlikely to persist, and a central

---

[4] The discussion in this section is mainly contributed by Jim Condon from NRAO. It is included here for the purpose of presenting a complete picture of our understanding of H_2O maser disks in this thesis.

supermassive BH would be required to account for the enclosed mass. Here, the evaporation timescale $\mathrm{t}_{\mathrm{evap}} \approx 136 t_{\mathrm{relax}}$ (t_{relax} is the half-mass relaxation timescale; Binney & Tremaine 2008) is considered to be the upper limit of the lifetime of any bound stellar system whereas the collision timescale is the characteristic timescale that a star suffers a physical collision (i.e. an inelastic encounter; Binney & Tremaine 2008).

To estimate the lifetime of the central cluster, we follow Maoz (1995) and assume that the central cluster has the Plummer density distribution (Plummer 1915):

$$\rho(r) = \rho_0 \left(1 + \frac{r^2}{r_{\mathrm{c}}^2}\right)^{-5/2} , \tag{3.4}$$

where ρ_0 is the central density and r_{c} is the core radius. (The reason for choosing the Plummer distribution is described in section 2.1 of Maoz (1998))

We constrain ρ_0 and r_{c} by fitting the position-velocity diagram of the megamaser disk with the rotation curve of a Plummer cluster:

$$v_{\mathrm{P}} = \left[\frac{G M_\infty r^2}{(r_{\mathrm{c}}^2 + r^2)^{3/2}}\right]^{1/2} , \tag{3.5}$$

where $M_\infty = 4\pi\rho_0 r_c^3/3$ is the total mass of the cluster. Here, M_∞ and r_{c} are fitted as free parameters. From these two parameters, we calculated $\rho_0 = 3M_\infty/4\pi r_c^3$. In all cases M_∞ is very close to the "enclosed" mass measured from the Keplerian rotation curve fit in Section 2, and the differences are less than $4-18\%$. In Figures 3.3 & 3.4, we show the fitted Plummer rotation curves along with the fitted Keplerian rotation curves.

Rather than using the method described above to constrain the core radius r_c, in some cases we could apply another approach that places even tighter constraints. We note that the Plummer rotation curve does not decrease monotonically with radius; instead the rotation curve turns over at a maximum rotation speed $v_{\rm max}$:

$$v_{\rm max} = \left(\frac{2GM_\infty}{3^{3/2} r_{\rm c}}\right)^{1/2} . \tag{3.6}$$

Having a maximum rotation velocity is not unique to a Plummer cluster. It is a general feature for clusters having the same form of density profile with the exponent smaller than $-3/2$.

The core radius $r_{\rm c}$ of a Plummer sphere having maximum rotation speed $v_{\rm max}$ is

$$r_{\rm c}^{(\rm max)} = \frac{2GM_\infty}{3^{3/2} v_{\rm max}^2} . \tag{3.7}$$

We used Equation 3.7 to estimate r$_c$ for the megamaser disks in NGC 1194, NGC 2273, NGC 2960 and NGC 4388. In these cases, we do not have very well-sampled or high quality rotation curves (see Figs. 3.3 & 3.4), so using $r_{\rm c}^{(\rm max)}$ from Equation 3.7 actually sets a tighter constraint on the core radius of the cluster than using rotation-curve fitting. For these four cases, we use the highest observed velocity in the PV diagram as an estimate (lower limit) of v_{max} and use it to calculate $r_{\rm c}^{(\rm max)}$ with M$_\infty$ from the Plummer rotation curve fitting from Equation 3.5. For UGC 3789, NGC 6323, and NGC 6264, we used r_c from rotation curve fits because they give tighter constraints on $r_{\rm c}$. In Table 3.1, we give the Plummer model parameters for all of our megamaser disks.

We constrained the lifetime of the Plummer cluster $T_{\rm age}$ by first requiring that the cluster not evaporate in a timescale less than the age of its host galaxy (≥ 10 Gyr if the galaxy has formed before $z = 2$). This requirement sets an upper limit to the mass of the constituent stars of the cluster because evaporation is unimportant so long as the mass of its stars satisfies the following equation:

$$\left(\frac{m_\star}{M_\odot}\right) \lesssim [\ln(\lambda M_\infty/m_\star)]^{-1}\left(\frac{r_{\rm h}}{0.01\,{\rm pc}}\right)^{3/2}\left(\frac{M_\infty}{10^8 M_\odot}\right)^{1/2} , \tag{3.8}$$

where $m_\star$ is the mass of each star, $\lambda \approx 0.1$ (Binney & Tremaine 2008), and $r_{\rm h}$ is the radius of half total mass ($r_{\rm h} \approx 1.305 r_{\rm c}$). We call the maximum $m_\star$ that satisfies the above equation $m_{\rm max}$ (Table 4) and use it to calculate the collision timescale of the Plummer cluster with the Plummer model parameters:

$$t_{\rm coll} = \left[16\sqrt{\pi} n_\star \sigma_\star r_\star^2 \left(1 + \frac{G m_{max}}{2\sigma_\star^2 r_\star}\right)\right]^{-1} , \tag{3.9}$$

where $n_\star = \rho_0/m_{\rm max}$ is the number density of stars, $\sigma_\star$ is the rms velocity dispersion of the stars, and $r_\star$ is the stellar radius (Maoz 1998; Binney & Tremaine 2008). If $t_{\rm coll}$ $<$ 10 Gyr, then $T_{\rm age}$ is constrained by $t_{\rm coll}$ and we can rule out the Plummer cluster as an alternative to the BH. If $t_{\rm coll} \geq$ 10 Gyr, we cannot rule out a cluster whether $T_{\rm age}$ is dominated by evaporation or collision.

For UGC 3789 we obtained an upper limit $m_{max} \approx 0.10 M_\odot$ to the mass of individual stars and a lower limit $N \gtrsim 1.0 \times 10^8$ to the number of stars in the cluster. The mass limit directly rules out neutron stars as the constituents of the cluster, and only brown dwarfs, very-low mass stars, or white dwarfs are possible. If the constituents of the cluster are brown dwarfs, the collision timescale for our Plummer model in UGC 3789 is $t_{\rm coll} < 3.9 \times 10^6$ years, much less than the age of a galaxy. The timescale is even shorter if the constituent stars are main-sequence stars. However, if the cluster is composed of white dwarfs, the collision timescale can be as long as 1.8×10^7 years, but this is still much shorter than the lifetime of a galaxy. Therefore, we conclude that a compact cluster is not likely to survive long, and the dominant mass at the center of UGC 3789 is a supermassive BH. For all other megamaser galaxies except NGC 1194 and NGC 6264, the lifetimes of the central clusters are also shorter than the age of a galaxy (Table 3.1). The constraints on lifetime weakly rule out massive clusters in NGC 4388 ($T_{\rm age} \approx 7 \times 10^9$ yr) but strongly rule out clusters in the others ($T_{\rm age} < 1.1 \times 10^9$ yr).

In summary, by setting tight constraints on the sizes and central mass densities of possible Plummer clusters, we have been able to strongly rule out clusters as the dominant central masses in UGC 3079, NGC 2273, NGC 6323, and NGC 2960 and weakly rule out the clusters in NGC 4388. We argue that supermassive black holes are the dominant masses in these megamasers. Together with the Milky Way Galaxy, NGC 4258, and M31 (Kormendy 2001), the number of galaxies with strong evidence to rule out a massive star cluster as the dominant central mass increases from three to seven.

Table 3.2. Upper limit on Continnum Emission from Megamaser Galaxies

Galaxy	$V_{\rm Center}$ (km s^{-1})	$V_{\rm Range}$ (km s^{-1})	$I_{2\sigma}$ (mJy)	Project Code
NGC 1194	3568	3489 - 3660	< 0.34	BB242B
NGC 2273	2800	2868 - 2909	< 0.18	BB261B
NGC 2960	5315	5296 - 5354	< 0.14	BB261C, BB261D
NGC 4388	2600	2881 - 2966	< 0.42	BB184C
NGC 6264	9710	9726 - 9776	< 0.16	BB261F, BB261H
NGC 6323	8100, 7650	8005 - 8200, 7556 - 7750	< 0.08	BB242M, BB242R, BB242S, BB242T

Note. — Col(1): Name of the galaxy; Col(2):The central Optical-LSR velocity of the bands used to search for continuum emission; Col(3) The velocity range corresponding to the selected channels. Note that the channels selected are chosen to be free of any maser lines except for NGC 2960. For this galaxy, we don't have line-free channels, and we averaged the bands centered at the systemic velocity of the galaxy and searched for continuum emission offset from the systemic maser emission; Col(4) The 2σ detection limit of the continuum emission; Col(5) The data used for continuum detection.

Table 3.3. Comparison of Maser BH Mass with Mass from Virial Estimation

Galaxy	maser BH (10^6 $M_\odot$)	virial BH (10^6 $M_\odot$)	R_{BLR} (light-days)	$V_{\rm FWHM}$ (km s^{-1})	Reference	L_X(2-10 kev) (10^{42} ergs s^{-1})	Reference
NGC 1068	8.6±0.3	9.0±6.6	4.6±3.0	2900	1	6.5, 2.6	5, 6
NGC 4388	8.5±0.2	7.1±4.9	2.0±1.2	3900	2	0.8, 0.9,1.9,1.0	7,8,9,10
NGC 2273	7.6±0.1	4.3±2.8	2.2±1.2	2900	3	1.0, 1.7	11,12
Circinus	1.7±0.3	4.8±3.2	1.9±1.1	3300	4	1.1, 1.0, 1.2	13,14,15

Note. — Col(1): Galaxy name; Col(2) BH mass measured from the megamaser technique. The BH mass of NGC 1068 is taken from Lodato & Bertin (2003) and Circinus from Greenhill et al. (2003). The BH masses of NGC 4388 and NGC 2273 are from this paper. Col(3): BH mass measured from the virial estimation method. Col(4): The size of the Broad Line Region (BLR) calculated using the $L_{(2-10kev)}-R_{BLR}$ correlation (Kondratko et al. 2005). Col(5): The full width at half maximum (FWHM) of the observed broad line (H_β for NGC 1068 and H_α for NGC 4388, NGC 2273, and Circinus). In NGC 2273, only the full width at zero intensity (FWZI) is given, so we estimate the FWHM "by eye". We assume the measurement uncertainty is 200 km s^{-1} in all cases. Col(6) Reference for the linewidth measurement. Col(7) Intrinsic hard X-ray (2-10 kev) luminosity. We used the average luminosity to calculate the size of the BLR. The error of the luminosity is taken to be the standard deviation of the adopted luminosities. Note that the distances used to calculate the intrinsic luminosities are 15.4, 19.0, 26.0, and 4.0 Mpc for NGC 1068, NGC 2273, NGC 4388, and Circinus, respectively. Col.(8) Reference for the adopted X-ray luminosities.

References – 1. Miller et al. (1991) 2. Ho et al. (1997) 3. Moran et al. (2000) 4. Oliva (1998) 5. Levenson et al. (2006) 6. Ogle et al. (2003) 7. Cappi et al. (2006) 8. Akylas & Georgantopoulos (2009) 9. Bassani et al. (1999) 10. Forster et al. (1999) 11. Terashima et al. (2002) 12. Awaki et al. (2009) 13.Yang et al. (2009) 14. Matt et al. (1999) 15. Smith & Wilson (2001)

3.4 Comparison With Virial BH Mass Estimates

It is important to compare results from different methods for measuring BH masses, because such comparisons can provide insight into potential systematic errors for each method (Siopis et al. 2009; Kormendy 2004; Humphrey et al. 2009; Greene et al. 2010). Comparing optically measured dynamical BH masses with those from the H_2O megamaser method is especially valuable, since the megamaser galaxies with Keplerian rotation curves provide the most direct and accurate BH mass measurements for external galaxies. These maser BH masses can be used to test the more commonly used BH mass measuring techniques in the optical, such as the stellar- or gas-dynamical methods.

One cannot meaningfully compare the stellar- or gas-dynamical BH masses with our maser BH masses unless the gravitational spheres of influence can be resolved. Otherwise, even if the optically determined dynamical masses agree with the maser BH masses within the errors, the uncertainty can be too large to tell the real accuracy of the stellar- or gas-dynamical method. The angular diameters of the spheres of influence of our maser BH masses, $2R_{\rm inf}$ (Table 3.1), range from $0\farcs006$ to $0\farcs06$. Among these megamasers, only the spheres of influence in NGC 4388 and NGC 1194 can be barely resolved by the HST (resolution $\approx 0\farcs07$ at $\lambda \approx 6500\mathring{A}$) or the Very Large Telescope (VLT) assisted with adaptive optics (resolution $\approx 0\farcs1$ at $\lambda = 2\,\mu$m). Therefore, of the galaxies here, stellar or gas dynamical measurements are feasible only for these two galaxies. We have obtained VLT time to measure the BH mass in NGC 4388, and we will apply the stellar dynamical method to this galaxy and compare the BH mass to the maser BH mass in the future.

Another commonly used BH mass measuring technique is the virial estimation method (Greene & Ho 2006; Kim et al. 2008; Vestergaard & Osmer 2009). We are able to compare this technique with the megamaser disk method in four galaxies, and this is the first time that the virial estimation method is directly tested. In this method, one estimates the BH mass as $M_{\rm BH} = f\,R_{\rm BLR}\sigma_{line}^2/G$, where f is an unknown factor that depends on the structure, kinematics, and orientation of the broad-line region (BLR), $R_{\rm BLR}$ is the radius of the BLR, σ_{line} is the gas velocity dispersion observed in the BLR, and G is the gravitational constant. Here, we adopt the latest empirically determined $\langle f \rangle = 5.2 \pm 1.3$ from Woo et al. (2010). Vestergaard (2009) suggests that the virial method is accurate to a factor of ≈ 4. Since we cannot directly detect the BLRs in megamaser galaxies that have Seyfert 2 nuclei, we estimated σ_{line} using the scattered "polarized broad lines" (PBL) from the hidden BLRs in those four megamaser galaxies with detected PBLs: NGC 1068, NGC 4388, NGC 2273, and Circinus. We estimated $R_{\rm BLR}$ via the $L_{(2-10kev)} - R_{\rm BLR}$ correlation (Kaspi et al. 2005). Table 3.3 shows the resulting virial BH masses for these four galaxies.

Under the assumption that the observed linewidth of broad H_α or H_β emission approximates the "intrinsic linewidth"[5], we find that for NGC 1068, NGC 2273, NGC 4388 and Circinus, the BH masses at the 1 σ level measured by the virial estimation method agree within a factor of 5 with the megamaser BH masses. So, while our comparison is so far limited to these four galaxies, the BH mass measured from the virial method matches the megamaser BH mass to about the expected accuracy.

The application of the virial method to megamaser galaxies is described in detail in the Appendix.

---

[5] By "intrinsic linewidth", we mean the linewidth one would measure if the BLRs were observed directly as in Type 1 AGNs

3.5 Maser BH masses and the $M - \sigma_\star$ relation

Table 4 shows the BH masses for all seven megamaser galaxies. Along with the previously published BH masses from megamaser observations, it is interesting to see that the maser BH masses, except in Circinus, are within a factor of 3 of $2.2 \times 10^7 M_\odot$, with the uncertainty of each BH mass $\leq$ 12%. This small range of masses is a selection bias. Disk megamasers are preferentially detected in Seyfert 2 spiral galaxies, and since the local active BH mass function for Seyfert 2 galaxies peaks at $M_{\rm BH} \approx 3 \times 10^7 M_\odot$ (Heckman et al. 2004), we are limited to BHs in this range of masses by analyzing disk megamasers.

Our new maser BH masses more than double the number of galaxies having dynamical BH masses $M_{\rm BH} \sim 10^7 M_\odot$. These measurements play a particularly important role in constraining the $M - \sigma_\star$ relation at the low-mass end of known nuclear BH masses. In a study that builds on the results of this thesis, Greene et al. (2010) find that the maser galaxies as a group fall significantly below the $M - \sigma_\star$ relation defined by more massive elliptical galaxies. As a result, the $M - \sigma_\star$ relation that fits later-type and lower-mass galaxies has both a larger scatter and lower zeropoint than the relation for elliptical galaxies alone. However, there is a potential caveat that measuring robust (well-defined) $\sigma_\star$ in late-type galaxies is challenging (Greene et al. 2010), and the contribution of systematic biases in $\sigma_\star$ to the deviation from the $M - \sigma_\star$ relation still needs to be explored in the future. With this caveat in mind, the observed deviations from the $M - \sigma_\star$ relation at low mass imply that the relation may not be a single, low-scatter power law as originally proposed.

In addition to our seven galaxies with maser BH masses, we currently have VLBI datasets for another four disk megamaser candidates, and we are monitoring the spectra of more than six disk megamaser candidates that are currently too faint to be observed with VLBI, but may flare up in the future. Along with these galaxies and more megamasers we may discover in the future with the GBT, we expect to obtain a larger sample of maser BH masses which could help to clarify the $M_{\rm BH}$-$\sigma_\star$ relation.

3.6 Summary

Our main conclusions from this chapter are the following:

1. The maser distributions in all seven megamaser galaxies are consistent with edge-on circumnuclear disks surrounding central massive objects in the active galactic nuclei. The inner radii of the disks are between 0.09 and 0.5 pc, similar to all previously published megamaser disks. The rotation curves of all seven megamaser disks are consistent with Keplerian rotation. Four of the megamaser disks reveal evidence for warps.

2. VLBI observations of circumnuclear megamaser disks are the only means to measure directly the enclosed mass and the mass density well within the radius of the gravitational sphere of influence of the central mass in these galaxies. The high central mass densities (0.12 to 60 $\times 10^{10} M_\odot$ pc^{-3} within the central 0.3 pc of the seven megamaser disks indicate that in all except two maser disks, the central mass is dominated by a supermassive BH rather than an extremely dense cluster of stars or stellar remnants. Although our current constraints are not strong enough to demonstrate that the BH is the dominant mass in two disks, it is most likely that this is the case.

3. The BH masses measured are all within a factor of 3 of $2.2 \times 10^7 M_\odot$ and the accuracy of each BH mass is primarily limited by the accuracy of the Hubble

constant. The narrow range of BH mass distribution reflects selection from the local active-galaxy BH mass function.

4. Stellar dynamics cannot be applied to the majority of the megamasers presented here to measure BH masses with high precision. The gravitational spheres of influence in all cases except NGC 1194 and NGC 4388 are too small to be resolved by current optical telescopes. Observations with the VLT for measuring the BH mass in NGC 4388 with stellar-dynamical modeling are in progress.

5. Under the assumption that the broad emission linewidths can be estimated from polarized scattered light, we have calibrated for the first time the BH mass determination by the virial estimation method based on optical observations. With the latest empirically determined $\langle f \rangle = 5.2 \pm 1.3$, the virial estimated BH mass is within a factor of 5 of the accurate BH mass based on megamaser disks in NGC 1068, NGC 2273, NGC 4388, and Circinus. This is comparable to the factor of 4 accuracy expected, given the uncertainty of the virial estimation method.

6. The accurate BH masses in the seven megamaser galaxies contribute to the observational basis for testing the $M - \sigma_\star$ relation at the low-mass end. The deviation of the $M - \sigma_\star$ relation defined mainly by large, elliptical galaxies from the mean relation of the several accurate maser BH masses suggests that the $M - \sigma_\star$ relation may not be a single, low-scatter power law as originally proposed, which has interesting implications for the universality of the $M - \sigma_\star$ relation (Greene et al. 2010).

Chapter 4

The Acceleration Measurement for H_2O megamasers in NGC 6264 and NGC 6323

4.1 Methods of Acceleration Measurement

Measuring accelerations of maser spots in an accretion disk can be a subtle and challenging task because of line blending, variability, and signal-to-noise (SNR) limitations. As explained in section 1.3 of chapter 1, one can measure the accelerations of masers by tracking how fast each maser line drifts with time. For spectra with each individual maser line well separated, one can just use the eye-balling fitting method to measure the acceleration reliably; for spectra with maser lines significantly blended, one will need to model the blending carefully in order to remove systematic bias. In the MCP team, we use a global least-square fitting program (GLOFIT) provided by Mark Reid from the Smithsonian Astrophysical Observatory to model the line-blending and variability, and measure the accelerations of maser lines. While this program has been successful for measuring the accelerations of masers in NGC 4258 (Humpreys et al. 2008, ApJ, 672, 800) and UGC 3789 (Braatz et al. 2010, ApJ, 718, 657), the joint effects of blending and low signal-to-noise in NGC 6264 and NGC 6323 make it challenging to apply the GLOFIT program directly. For these two galaxies, one may need to use the GLOFIT program in a different way in order to find reliable solutions. In this chapter, we will first use simulated spectra that have similar characteristics as the spectra for NGC 6264 to show what difficulties one might encounter with both the eye-balling and GLOFIT methods when line-blending and signal-to-noise limitations are significant issues. We will then discuss a new way to use the GLOFIT program so that we can overcome the difficulties and measure reliable accelerations for NGC 6264 and NGC 6323.

4.1.1 The Eye-balling Method

In the maser spectra of NGC 6264 and NGC 6323, the lines are often blended and the flux density usually varies on a timescale of a few months, and the features are nearly always broader than the typical linewidth (~ 2 km s^{-1}) for a single systemic maser line. To see how blending and the SNR limitation complicate and bias the acceleration measurement, we simulate a set of spectra (Figure 4.1a) that have similar flux density distribution, SNR, time variation, linewidth, and acceleration as the dominant maser clump in NGC 6264. In the synthetic spectra, we place nine spectral lines between 7845 km s^{-1} and 7861 km s^{-1} in the beginning of the simulated observations (epoch 0) with 2 km s^{-1} interval between two adjacent lines. We then allow the maser lines to drift with a constant acceleration $a = 1.0$ km s^{-1} yr^{-1}, and generate a spectrum every 30 days. In total, we have 24 epochs of synthetic spectra. We determine local velocity peaks from each spectrum by eye, and in Figure 4.1b (the time-velocity plot), we plot the velocities of the peaks in the synthetic spectra as a function of time. The measurements of the radial velocities are accurate to about one channel width (~ 0.3 km s^{-1}).

In the time-velocity plot, we can see that while the trend of redward drift is clear, only four lines can be identified clearly. The line-blending prevents one from distinguishing most spectral features and cause the velocities of maser peaks to be randomly scattered in the bottom half of Figure 4.1b. The two most distinct features in the time-velocity plot are the two dominant maser lines that last over the entire observational period. The best fit accelerations for these two lines are 1.10±0.05 (the top feature) and 1.08±0.06 (the bottom feature) km s^{-1} yr^{-1}. The line that has the highest velocity has an acceleration of 1.17±0.15 km s^{-1} yr^{-1}, and the acceleration of the line with the lowest velocity is 1.52±0.44 km s^{-1} yr^{-1}. Here, the acceleration errors are estimated to be the fitting error scaled down by the square root of χ^2.

What these measurements tell is that the eye-balling fitting method could provide good estimates for the lines that have sufficient SNR. However, since the blending effect prevents one from seeing the peaks of the majority of maser lines in the spectra, making accurate acceleration measurements for these lines with the eye-balling fitting is not possible. Although one can use the average acceleration (a =1.12±0.04 km s-1 yr^{-1}) of the four lines that can be identified by eye as an estimate, it may be difficult to claim this estimate is accurate and precise with such small number statistics. Therefore, in order to avoid bias and measure accelerations more accurately for all lines, one will need a global fitting program that can model the line-blending satisfactorily. To this end, we need the GLOFIT program.

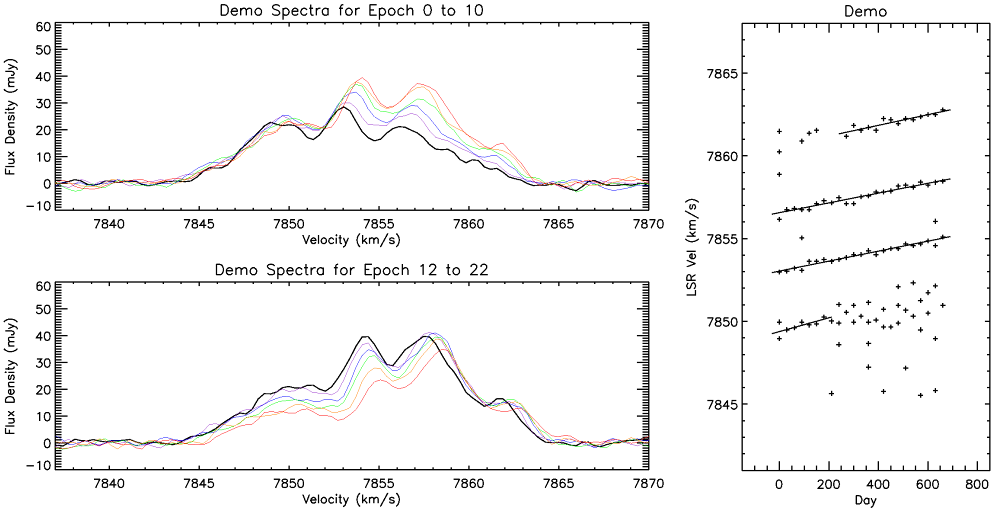

Fig. 4.1.— The left two plots (Fig. 4.1a) show the synthetic spectra that have similar flux density distribution, SNR, linewidth, time variation, and acceleration as the dominant maser clump in NGC 6264. A spectrum is generated once a month over two years. Therefore, we have 24 epochs of spectra in total. The top-left plot shows the spectra for epochs 0, 2, 4, 6, and 8 (black, purple, blue, green, orange, and red) and the bottom-left plot shows the spectra for epochs 10, 12, 14, 16, and 18 (black, purple, blue, green, orange, and red). One can see clearly the whole spectral pattern drifts toward higher velocity with time. The plot on the right (Fig. 4.1b) shows the best-fit accelerations from the eye-balling method plotted on top of the radial velocities of maser peaks as a function of time.

4.1.2 The GLOFIT Method

To fit maser accelerations, the GLOFIT program decomposes given sections of spectra from multiple epochs simultaneously into individual Gaussian line profiles. This is a nonlinear, multiple Gaussian-component least-squares χ^2 minimization routine. Each Gaussian component is represented by its amplitude, linewidth, central velocity at the reference epoch, and acceleration. All these parameters are allowed to vary with time, and the central velocity and acceleration can be held fixed when necessary. Since this routine usually fits hundreds of parameters at a time and therefore is very nonlinear, in order to prevent instability during the fitting process, the program only allows the fitted linewidths to be within a certain range around the *a priori* linewidths, which are usually $\sim$ 2 km s^{-1}, the expected maser linewidth for gas kinetic temperatures of 400 to 1000 K. To set the allowed range for fitted linewidth, one needs to tell the program the uncertainty for the *a priori* linewidths, and the program will find the solutions such that there is a 68% probability for the difference between the fitted and the *a priori* linewidths to be within the specified uncertainty. Typically, we start the fitting process by setting the *a priori* linewidths and their uncertainties to be 2.0 and 0.3 km s^{-1} yr^{-1}, and we will use these values for the demonstration in this section. In section 4.1.2.1, we will show that for different sections of spectra, it may be necessary to adopt different *a priori* linewidths to minimize the χ^2 of the fitting, and choosing appropriate *a priori* linewidths is important to obtain correct fitting results.

To apply the GLOFIT program to NGC 6264 and NGC 6323, we found it necessary to use a different strategy than in UGC 3789 (Braatz et al. 2010). The first issue with direct application of the GLOFIT program to these two galaxies is that it is not easy to find stable and converging solutions because of the joint effect of more significant blending and SNR limitations. In addition, even when we can reach a converging and stable fit for a given section of the spectra, we still feel uncertain about the accuracy of the solutions because they can easily change when we use different initial parameters for the program. Without sufficient external information such as the accelerations of the high SNR lines measured from the eye-balling method to constrain the solutions, it may be difficult to avoid systematic biases in the solutions. We use the simulated spectra described in section 4.1.1 to demonstrate this case.

We first fit the simulated spectra described in section 4.1.1 from epoch 12 through epoch 23 with the GLOFIT program. In the fitting, we use the expected accelerations and line velocities as the initial conditions, and Figure 4.2 shows examples of the fit. Note that we choose 11 spectra here because it is the minimum number of spectra that can allow a stable and converging fit. In the real data for NGC 6264 and NGC 6323, we usually have fewer spectra to use for any persistent spectral patterns. This means that finding stable solutions with a small number of relatively low SNR and blended spectra is not always possible, and this is one of main issues for these two galaxies when we use the standard GLOFIT technique.

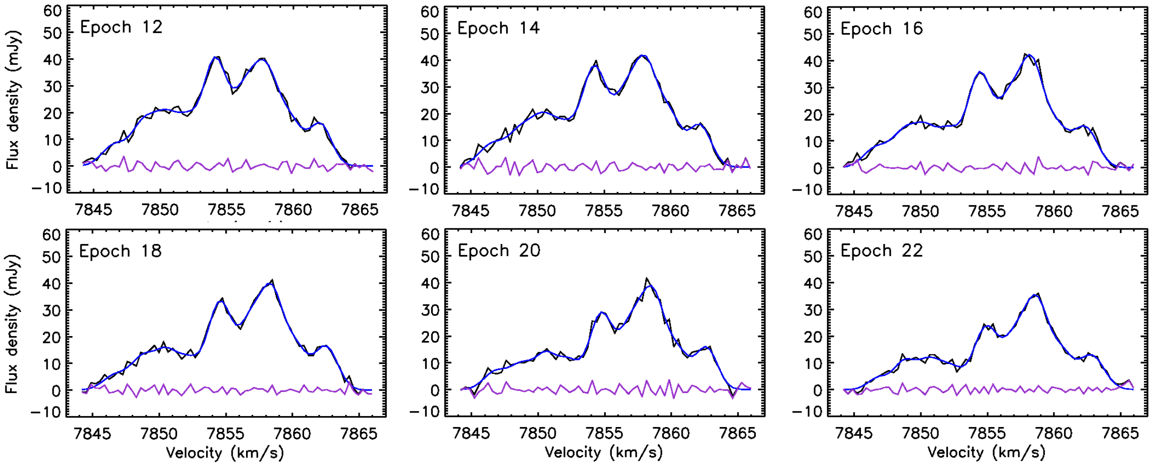

Fig. 4.2.— These six panels show the result of the global fitting for the synthetic spectra (described in section 4.1.1) from epochs 12, 14, 16, 18, 20, and 22. The black and blue curves represent the data and fitted model, respectively. The purple curves show the residuals of the fitting.

The general fitting quality seen in Figure 4.2 is quite good. The σ per degree of freedom (i.e. the square root of the reduced χ^2) of the fitting converges at 1.0571, and the residuals are consistent with the statistical noise. While the fitting quality seems satisfactory, the best fit accelerations and line-center velocities do not all agree with the expected values. In Figure 4.3a, we compare the fitted peak velocities and accelerations with the expected values. For the section of the spectra (V = 7853

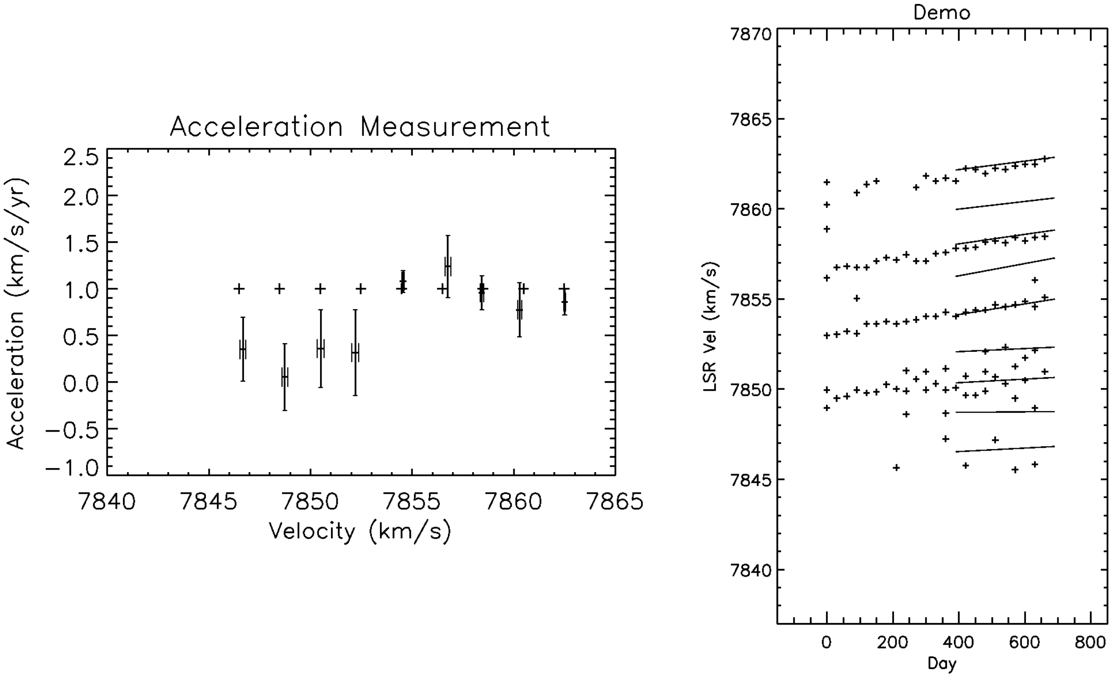

Fig. 4.3.— In Fig. 4.3a (the left panel) we compare the fitted peak velocities and accelerations of the model maser lines with the expected values. The x and y coordinates of the crosses show the expected values for the accelerations and velocities at the reference epoch (epoch 18). The data points that show error bars are the measurements from the GLOFIT program.; Fig. 4.3b (the right panel) shows the peaks of the synthetic maser spectra (the plus symbols) as a function of time. The line segments plotted on top of it correspond to the accelerations measured from the GLOFIT program. The offsets between the line segments and the average trends of the plus symbols are the result of line blending.

− 7865 km s^{-1}) that shows more distinctive peaks, the fitting results agree with expected values very well. For the section (V = 7845 − 7853 km s^{-1}) that are fainter and more blended, the fitted accelerations are obviously biased toward lower values. Therefore, without prior knowledge for their actual accelerations, the masers at the lower velocity range could be mis-regarded as lines coming from a different ring.

The biased measurements for the lines between V = 7853 − 7865 km s^{-1} in the synthetic spectra represent a limitation one would encounter when fitting blended lines using this least-square technique from low-SNR blended spectra (the SNR of the lines at this velocity range is $\sim$ 10). For such spectra, while the blending effect already makes different lines hard to distinguish, the low SNR further complicates the fitting by confusing the program between noise peaks and real features. We found that even if we already know the low SNR maser lines should have the same acceleration as the features with higher SNR, including the biased acceleration measurements for the low SNR lines into the calculation of average acceleration of all features would increase the uncertainty (i.e. rms scatter of the acceleration measurements) of the average acceleration by more than a factor of 2 compared to the uncertainty ($\sim$0.12 km s^{-1} yr^{-1}) calculated without including the low SNR lines. Because of the above issues, we may need a different way to apply the GLOFIT program to NGC 6264 and NGC 6323 in order to measure the accelerations of these lines more accurately and reliably.

Applying GLOFIT by Assuming Constant Acceleration

One way to improve the situation is to enforce all the maser lines in the velocity range of interest to drift at the same rate in the global fitting. This would be most appropriate if one has prior knowledge that they have the same acceleration (e.g. the masers show a linear trend in the position-velocity (P-V) diagram). This approach helps the program to reach convergence more efficiently and stably because the SNR of the fitting increases when we enfore a common acceleration. The SNR increases because we effectively use the drifting of the entire spectral pattern to measure the acceleration rather than using individual maser lines. In the following, we apply the GLOFIT program to the synthetic spectra from the previous section with the constant acceleration assumption, and demonstrate that one can indeed use this approach to measure reliable accelerations.

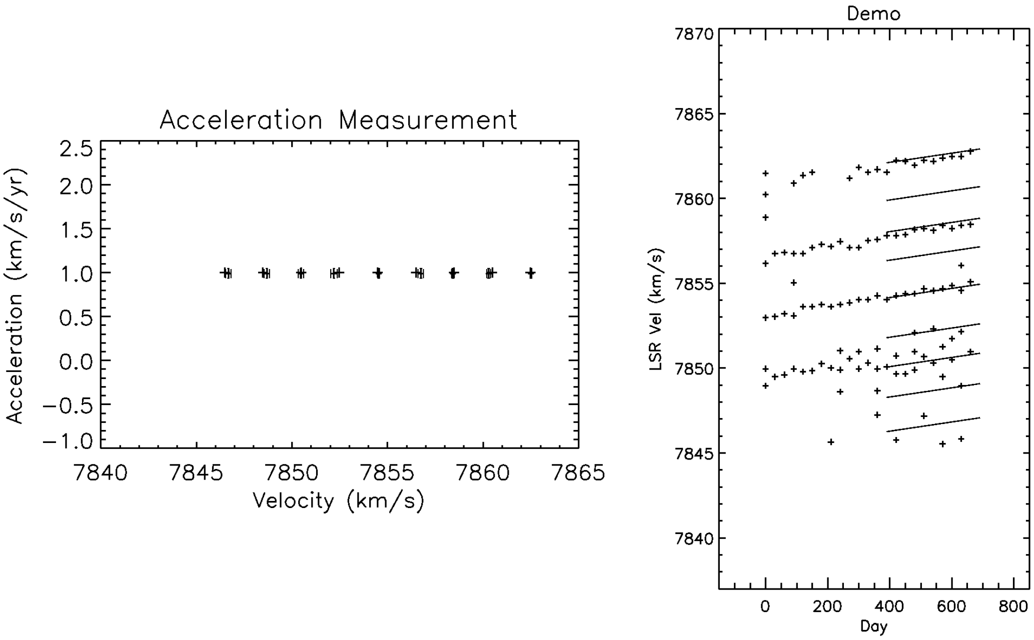

Fig. 4.4.— In Fig. 4.4a (the left panel) we compare the fitted peak velocities and accelerations of the model maser lines with the expected values. The x and y coordinates of the crosses show the expected values for the accelerations and velocities at the reference epoch (epoch 18). The data points that show error bars are the measurements from the modified GLOFIT program.; Fig. 4.4b (the right panel) shows the peaks of the synthetic maser spectra (the plus symbols) as a function of time. The line segments plotted on top of it correspond to the accelerations measured from the modified GLOFIT program.

After modifying the GLOFIT program to allow a constant acceleration for all maser lines, we run the modified program on the synthetic spectra from epochs 12 through 23 with the expected answers for the initial conditions. When we perform the fitting, we assume that all maser lines drift at the same rate[1]. In Figure 4.4, we

---

[1] Note that while the constant acceleration assumption is true for the synthetic data, one can imagine that this assumption will not be always valid in real situation. One critical way to check whether this assumption holds is to see whether one can get the reduced χ^2 close to 1.0 after the fitting. If not, then one may need to drop this assumption, and allow the acceleration to be a free parameter for each maser line. There will be more discussion on this point at the end of this section.

can see that the fitting result is quite good. The best fit acceleration is 0.99±0.05, consistent with the correct answer well within the error bar (Figure 4.4a). In addition, the fitted accelerations also agree well with the trends seen in the time-velocity plot (Figure 4.4b). The σ per DOF converges at 1.0585.

One nice feature of the modified GLOFIT technique is that one can still obtain stable and converging solutions even if the number of spectra used for fitting is small. We have tried to apply the modified GLOFIT program to only six spectra (Epoch 18 through 23), and the χ^2 of the fit converges at 1.06756 with the best fit acceleration of 0.95±0.13 km s^{-1} yr^{-1}. This is good news for masers in NGC 6264 and NGC 6323 because there are usually six or fewer spectra to use for any truly persistent patterns, and the unconstrained GLOFIT technique usually cannot give stable solutions.

While this new approach works well for the idealized synthetic data here, it may still require another minor modification in order to measure the accelerations effectively with real spectra. In NGC 6264 and NGC 6323, the spectra usually have larger variability in both flux density and linewidth than our synthetic spectra here, and we sometimes still cannot find stable solutions with the GLOFIT program easily even if we make the constant acceleration assumption. We found that an easy way to help the modified GLOFIT program find converging solutions more efficiently is to require the fitted velocity of the dominant maser line at the reference epoch ($V_{\rm fit}$) to be within a reasonable range around the most likely (true) value (V_0). Since the dominant maser feature in a clump of maser lines usually has the higher SNR in the clump and is not severely blended, it is reasonable to use the velocity ($V_{\rm peak}$) of the peak of the maser clump as an estimate of V_0, and require $V_{\rm fit}$ to be close to it.

To actually implement this idea in the fitting, we first fix $V_{\rm fit}$ at $V_{\rm peak}$ and fit the synthetic spectra from epoch 18 through 23 with the modified GLOFIT program until χ^2 of the fit reaches the minimum and converges. We record the minimum σ per DOF afterward. The same step is repeated for many times and each time we fix $V_{\rm fit}$ at a velocity slightly different from $V_{\rm peak}$ and measure the lowest σ per DOF. In Figure 4.5, we show the σ per DOF as a function of the fixed velocities in the fitting.

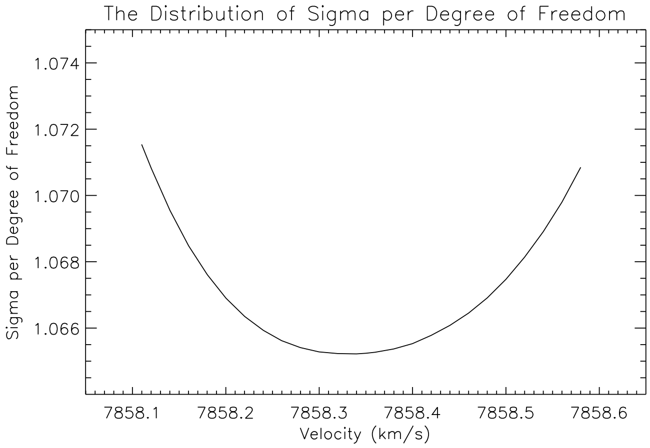

Fig. 4.5.— The σ per DOF (i.e. the square root of χ^2) as a function of the fixed velocities after fitting the synthetic spectra with the modified GLOFIT program.

In this figure, we see that the minimum χ^2 occurs at the velocity of 7858.34 km s^{-1}, which is 0.14 km s^{-1} away from $V_{\rm peak}$. The corresponding acceleration is 1.02±0.11 km s^{-1} yr^{-1}, consistent with the expected answer. We conclude that this method to constrain the fitting is a viable approach to find correct answers.

While the above method seems to be robust now, we discovered a surprising and unexpected feature of the modified GLOFIT program when testing the fitting with the synthetic data − the fitting result could depend sensitively on the *a priori* linewidths that one choose. When the *a priori* linewidths are set incorrectly, one could get a biased answer. For example, when we set the *a priori* linewidths to be 2.1 km s^{-1} and apply the modified GLOFIT program to the synthetic spectra from epoch 18 through 23 (without constraining $V_{\rm fit}$), the best fit acceleration is 1.15±0.12 km s^{-1} yr^{-1}. So the result increases by 20% and is now away from the correct value by more than 1 σ. When the *a priori* linewidths are 2.2 km s^{-1}, the best fit acceleration becomes 1.22±0.12, which is even farther away from the true value. When setting the *a priori* linewidths to be 1.9 km s^{-1}, the fitting does not converge.

Such a sensitivity of the fitting result on the *a priori* linewidths is perplexing because it doesn't seem clear what *a priori* linewidths would be the best. There is no clear reason why the *a priori* linewidths must be 2.0 km s^{-1} exactly. To understand what is the best *a priori* linewidth to use, we have done some experiments by changing the average linewidth of the synthetic maser lines to different values. We conclude that one must try a range of linewidths and use the one that gives the best χ^2.

We also examine whether or not the fitting result depends on the *a priori* linewidth *errors* sensitively with both synthetic and real data. The fitting with *a priori* linewidth errors between 0.3−0.5 km s^{-1} usually gives consistent results, and setting the *a priori* errors to be larger (e.g 0.5 km s^{-1}) can allow a better fit (i.e. lower reduced χ^2). However, when the *a priori* linewidth errors are set to be too large, usually $>$ 0.7 km s^{-1}, the fitting often becomes unstable. So, a good strategy to use the modified GLOFIT program would be to start with smaller *a priori* linewidth errors (0.3 km s^{-1}), look for the best values for the *a priori* linewidths, and finally use larger *a priori* linewidth errors (0.4 or 0.5 km s^{-1}) to enable better fits.

Finally, the applicability of the modified GLOFIT program depends critically on the assumption that masers within the selected range of spectra drift at the same rate. Therefore, to avoid systematic errors it is important to examine whether the chosen sections of spectra really satisfy this assumption. Here, we lay out a systematic way to find the masers that drift at the same rate and use the modified GLOFIT program to find reliable solutions:

1. Use the time-velocity plot from the eye-balling method to examine the general trends of accelerations. This can usually tell one the rough regions within which the masers might drift at the same rate.

2. For the regions in the spectra where the masers might have the same acceleration, one can check whether the spectral pattern formed by these masers remain consistent with time (i.e. the shape remains similar). If true, it is likely that the maser pattern as a whole drifts at the same rate, and one can apply the modified GLOFIT program and see if one can obtain a good fit. If one can obtain a reduced χ^2 close to 1.0, it is very likely that the constant acceleration assumption holds, and one can trust the solutions.

3. However, if the spectra within the velocity range of interest are heavily blended and appear to be very smooth with few distinct peaks, a good fit (i.e. $\chi^2 \sim 1.0$) with the modified GLOFIT program may not always indicate that the masers in the fitting indeed have the same acceleration. From our current experience, the program can fit a smooth pattern well even if some lines in this pattern have different accelerations. There are two ways to examine whether the assumption of constant acceleration really holds in this case: (1) if the pattern just appears to be smooth near the boundary, one can narrow the velocity range for the fitting and use smaller a number of Gaussian components to make the fit. If the result changes substantially, then it suggests that lines at the boundaries have different accelerations and thus bias the results; (2) One can also check the VLBI positions of these masers in the sky and in P-V diagram. If some maser spots have significantly divergent positions, or appear in unexpected regions in the sky, or do not show linear trends in the P-V diagram, it may mean that they come from different rings. In this case, one can just ignore these spots and use the masers with good VLBI positions and reliable acceleration measurement.

For the systemic masers in NGC 6264 and NGC 6323, we will follow these guidelines to measure accelerations with the modified GLOFIT program.

4.2 Acceleration Measurement for NGC 6264

We took 20 H_2O maser spectra with the GBT for NGC 6264 between 2008 November 21 and 2011 March 2. Except during the summer months when the humidity makes observations at 22 GHz inefficient, we took a spectrum on a monthly timescale. For these observations, we follow the same observing settings and data reduction procedures as in Braatz et al. (2010). Table 1 shows the observing date and sensitivity for each observation and Figure 4.6 shows a representative H_2O maser spectrum for NGC 6264.

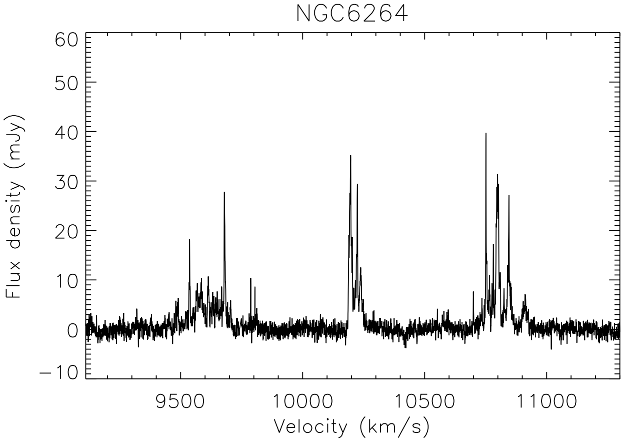

Fig. 4.6.— A representative spectrum for NGC 6264. This spectrum was observed on 2010 February 9.

For both NGC 6264 and NGC 6323, we take different approaches to measure the accelerations for the systemic and the high-velocity masers. For the systemic masers, we apply the modified GLOFIT program to perform multi-epoch spectral decomposition and determine precise accelerations for those maser components drifting at the same rate. For the high-velocity masers, we simply use the eye-balling method to measure the accelerations for those distinct and persistent lines and make a conservative estimate of their uncertainties without modeling variability and blending. The reason why we adopt two different approaches is that an accurate distance determination with the H_2O megamaser method depends primarily on systemic masers, and therefore we need the GLOFIT program to measure acceleration accurately. For the high velocity masers, an accurate acceleration measurement is less critical for distance determination as long as they are close to the mid-line of the accretion disk (which can be determined by rough estimate of accelerations) and follow Keplerian rotation.

4.2.1 High Velocity Masers

In Figure 4.7, we plot the radial velocities of NGC 6264 maser peaks measured by eye as a function of time. For the blueshifted and redshifted masers, we first identify lines that are persistent in time and then fit a straight line to the data to measure the acceleration directly. We estimate the uncertainty of the measurements by scaling the fitting error by the square root of reduced χ^2. In Table 4.2, we show the measured accelerations and uncertainties.

The weighted average accelerations of the redshifted and blueshifted masers are -0.06 and 0.01 km s^{-1} yr^{-1} respectively. The rms scatter of acceleration of the redshifted and blueshifted masers are both 0.11 km s^{-1} yr^{-1}. The small acceleration and rms scatter indicate that the high velocity masers are close to the mid-line of the accretion disk as expected. With these measurements and the scatter seen in the rotation curve of the high velocity masers, we can confidently infer that the majority of the high velocity maser spots must fall within ≈10 degrees from the mid-line of

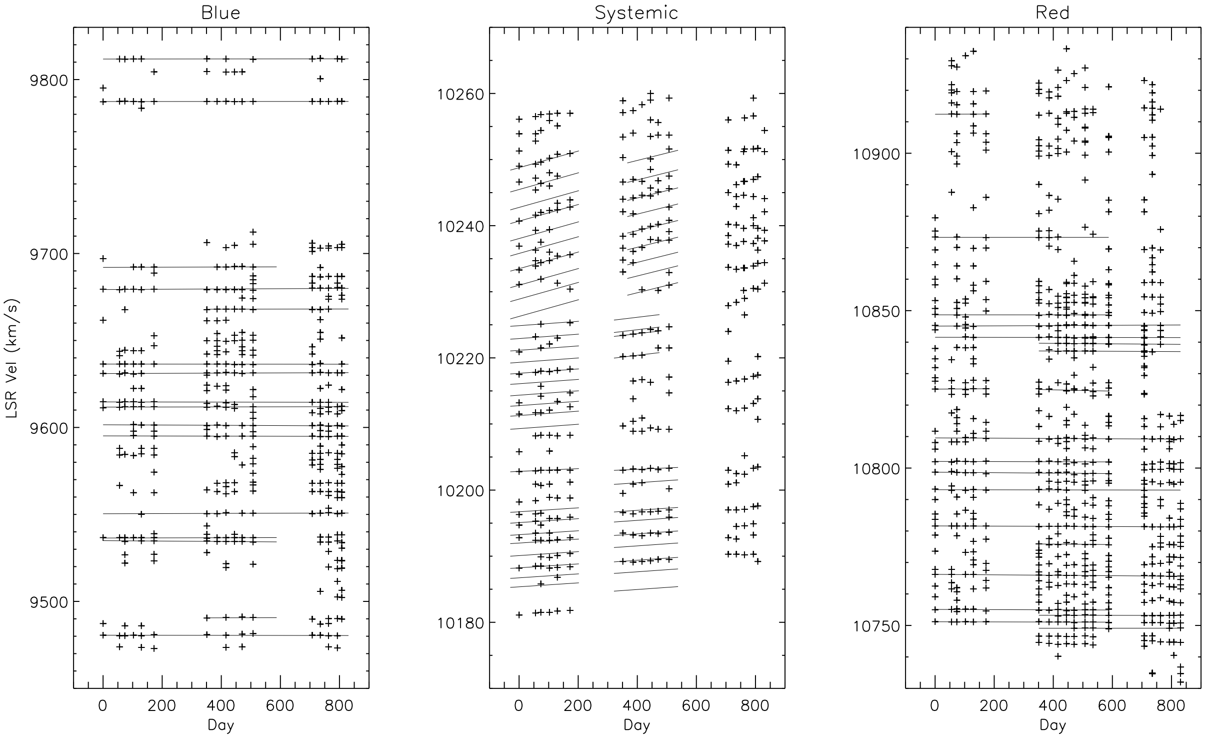

Fig. 4.7.— In this figure, we plot the radial velocities of NGC 6264 maser peaks as a function of time (the crosses) along with the fitting results from the eye-balling method (for the high velocity masers) or from the modified GLOFIT program (for the systemic masers).The data between Day 0 and 200 come from spectra taken in Period A; the data between Day 300 to 600 from spectra in Period B; and the data between Day 700 to 900 are from spectra in Period C.

the disk.

When assigning the measured accelerations to the corresponding channels in the VLBI datasets, we pay attention to whether the periods over which the accelerations are measured actually bracket the epochs of our VLBI observations. We have two tracks (BB261F & BB261H) of VLBI observations in Period A, two tracks (BB261K & BB261Q) in Period B and no good data in Period C. For those masers persisting over Periods A through C, we assign the measured accelerations to the corresponding VLBI channels from averaging all four tracks. For those masers that persist only during Period A or B, we assign the accelerations only to the VLBI channels from observations in the respective period. For maser spots without acceleration measurement from the eye-balling method, we assume their accelerations to be zero and assign them to the data from averaging all four tracks. For all the VLBI channels that we will use for distance determination with the 3-dimensional modeling program which will be described in Chapter 5, we adopt two times the rms scatter (0.22 km s^{-1} yr^{-1}) of the accelerations from the eye-balling method as their uncertainties. Since the uncertainties adopted here are just crude estimates, these numbers may need to be further adjusted in the 3-dimensional modeling program along with the uncertainties for the other types of data (e.g. maser positions on the sky) in order to make the final reduced χ^2 of the fitting close 1.0.

4.2.2 Systemic Masers

Figure 4.8 shows the maser spectra from Epochs 0 through 5 (Period A) and from Epochs 6 through 11 (Period B). We do not show the spectra from Period C because we currently do not have good VLBI observations at Period C and thus the acceleration measurement for Period C is not needed at this moment. Since both Periods A and B bracket two tracks of VLBI observations and the accelerations of systemic masers could change with time, we measure acceleration in Periods A and B separately. In cases where the accelerations measured in both periods within a certain velocity range are the same and the corresponding VLBI positions are consistent, we assume that the masers come from the same ring, and average the accelerations and VLBI positions. For those maser lines that only persist during one period, we only use the VLBI positions at this particular period for these masers in the distance measurement.

We follow the guidelines in section 4.1.2.1 to look for maser clumps that drift at the same rate and apply the modified GLOFIT program to measure their accelerations. We break the spectra into distinct velocity ranges, as indicated in Figure 4.8, and analyze each range individually.

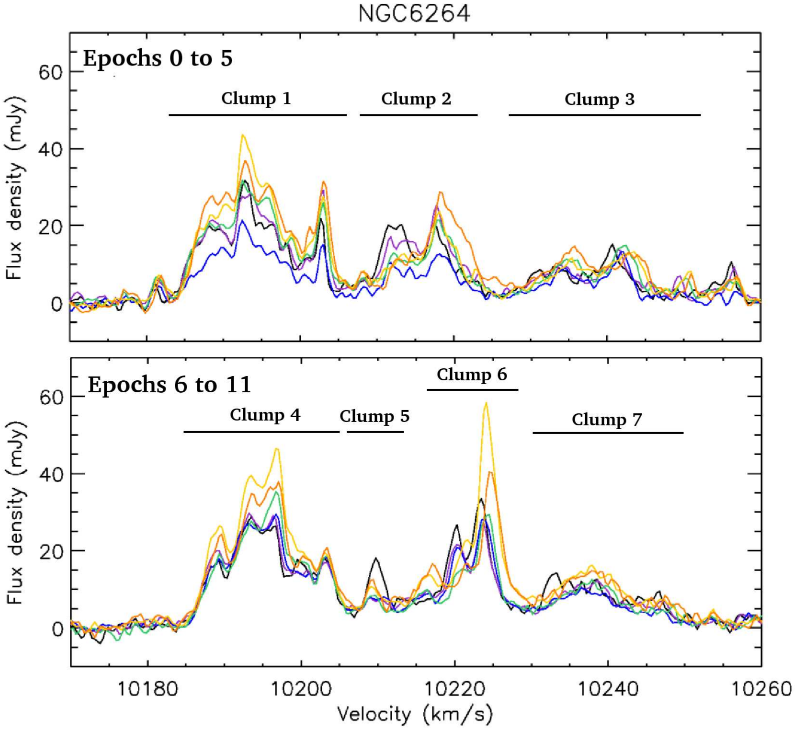

Fig. 4.8.— The upper panel shows the spectra from epoch 0 through 5 (purple, blue, green, yellow, and orange), and the bottom panel shows the spectra from epoch 6 through 11 (purple, blue, green, yellow, and orange). The whole velocity ranges of the systemic masers in Period A and B are divided into 7 clumps for the convenience of acceleration measurement.

Clump 1

The results from the eye-balling fitting suggest that the maser lines at V $\sim$ 10202.8 km s^{-1} have significantly smaller acceleration (a $\sim$ 0.6 km s^{-1} yr^{-1}) than the rest of the masers (a $\sim$ 1.2 km s^{-1} yr^{-1}). Therefore, to measure the acceleration with the constant drifting rate assumption, we divide Clump 1 into two velocity sections: 10183.0 to 10200.2 km s^{-1} and 10200.2 to 10203.5 km s^{-1}, where V = 10200.2 km s^{-1} is at the local minimum that divides the two sub-clumps.

For the maser lines of Clump 1 within 10183.0 to 10200.2 km s^{-1}, we could not find a model to make a stable fit unless we narrow the velocity range to 10183.0 to 10197.7 km s^{-1}. This suggests that maser lines between 10197.7 and 10200.2 km s^{-1} have different accelerations than the other lines in the fitted velocity range, and this is supported by the VLBI position at this velocity range. Since we cannot give a good constraint on the accelerations of these lines, we do not include them in the distance determination. For lines between 10183.0 and 10197.7 km s^{-1}, we successfully fit 8 Gaussian components to the spectra and obtain an acceleration of 1.04± 0.14 km s^{-1} yr^{-1}. The reduced χ^2 for this fit is 1.144 (the degrees of freedom is 153). For the maser lines between 10200.2 to 10203.5 km s^{-1}, we fit two Gaussian components and obtain an acceleration of 0.75±0.1 km s^{-1} yr^{-1}. We overplot the acceleration measurements in this and the following subsections on top of the time-velocity plot for the systemic masers (the middle plot of Figure 4.7) and list the results in Table 4.3. We also show an example of the result of the Gaussian decomposition in the acceleration fitting with the masers in Clump 1 in Figure 4.9.

Clump 4

The maser lines in Clump 4 reside within the same velocity range as Clump 1 and the situation is similar. So we perform the fitting in two velocity sections: 10184 to 10201.6 km s^{-1} and 10201.6 to 10205.5 km s^{-1}, where V = 10201.6 km s^{-1} is at the local minimum that divides the two sub-clumps. For masers lines between 10184 to 10201.6 km s^{-1}, we successfully fit 9 Gaussian components to the data and obtain an acceleration of 1.12±0.18 km s^{-1} yr^{-1} with reduced χ^2 of 1.009. For the masers between 10201.6 to 10205.5 km s^{-1}, we could not find a reliable fit because of severe blending. The fitted acceleration can even be negative, which is unlikely based on the apparent acceleration measured by the eye-balling fitting and the position of the corresponding maser spot in the position-velocity diagram. By comparing the maser spectra from Period A and Period B, we argue that since the line structure remains similar over Periods A and B at this velocity range, we are seeing the same maser lines that appear at slightly different velocities because of the acceleration. The reason we couldn't measure a reliable acceleration for these ($\sim$ 2) lines in Period B is the severe blending. This idea is further supported by the fact that the VLBI position of the masers at this velocity range from Periods A and B are very well consistent with each other. For these reasons, we assume these masers have the same acceleration (a = 0.75±0.1 km s^{-1} yr^{-1}) as the masers in Clump 1 at the similar velocity range.

Clump 2

The maser lines in Clump 2 are apparently drifting and the general pattern of the clump seems to persist with time. Therefore, we might suppose that the masers in this clump drift at the same rate. However, we couldn't find a good model to fit the data. The best reduced χ^2 we can achieve is 1.44, and the fitted acceleration is 1.2±0.3 km s^{-1} yr^{-1}. Although the result is consistent with the fitted acceleration from the eye-balling fitting for the strongest line in this clump (a =1.55±0.23 km s^{-1} yr^{-1} at V$\sim$10218 km s^{-1}), the result is unreliable because the probability to achieve a reduced χ^2 of 1.44 for a system with 144 degrees of freedom is nearly zero. The situation does not improve when we only fit subsets of this clump. In fact, the VLBI positions of the masers in this clump do not lie on a straight line, and this further supports the idea that the masers in this clump have different accelerations and our constant acceleration assumption does not hold. Therefore, for masers in this clump, we only use the VLBI channel at V=10218.11 km s^{-1} in the distance determination because it is the only line for which we have an acceleration measurement from the eye-balling fitting for this clump.

Clump 5 and 6

Clump 5 covers a velocity range between 10207 to 10212 km s^{-1} and the lines within this velocity range do not show a clear sign of drifting. In addition, the line structure changes substantially over the course of time and we found it difficult to measure a reliable acceleration for this clump. We can measure significantly different accelerations, ranging from 0.4 to 4.2 km s^{-1} yr^{-1}, by removing just one epoch of the spectra in the fit. Such large differences when using different sets of spectra indicate that we are seeing different lines at different epochs. Since this violates the main assumption in our model, we cannot measure the acceleration for Clump 4 reliably. Along with the fact that the VLBI positions for masers in this clump have relatively large error bars, we decide not to include these masers in the distance determination.

The acceleration measurement for masers in clump 6 is also not trivial. We couldn't achieve a converging fit with spectra from epochs 6 through 11. The line structure changes substantially at epoch 10. By inspecting the spectra in Period B along with those in Period C, we discovered that the line at V $\sim$ 10224.1 km s^{-1} starts to drift at a much higher rate ($a > 7$ km s^{-1} yr^{-1}) after epoch 9. This may be caused by newly arising lines from smaller radii of the disk. Because of this complexity, we only use the spectra from epochs 6 through 9, during which the line shapes appear to be persistent, to measure the acceleration. We fit four Gaussian components with an average linewidth of 2.3 km s^{-1} to the masers between 10218.9 to 10226.8 km s^{-1}. We obtain an acceleration of 1.79±0.36 km s^{-1} yr^{-1} with reduced χ^2 of 1.12 (52 degrees of freedom).

Clump 3 and 7

Maser lines in Clump 3 have the largest acceleration among the systemic masers in NGC 6264. The acceleration is so large that the drifting of the whole clump can be seen clearly in Figure 4.8. We fit ten Gaussian components with an average linewidth of 2.4 km s^{-1} to the masers between 10226.0 to 10252.3 km s^{-1}. The measured acceleration is 4.43 ± 0.36 km s^{-1} yr^{-1} with a reduced χ^2 of 1.006 (314 degrees of freedom).

The masers in Clump 7 cover nearly the same velocity range as Clump 6, but the drifting of the whole maser pattern becomes much less clear because of both severe blending and reduced SNR. The blending causes the line structure to become very smooth and there are only two lines that can be seen to drift clearly in the time-velocity plot (Figure 4.7). The smooth line structure is an issue for the modified GLOFIT program because the program can easily find a solution to fit a smooth clump even if some lines in the clump do not really drift at the same rate as the other. Therefore, we need additional information to judge whether the lines in this clump do have the same acceleration.

For Clump 7, we fit nine Gaussian components with an average linewidth of 2.3 km s^{-1} to the masers between 10230.5 to 10250.5 km s^{-1}. The measured acceleration is 3.96 ± 0.59 km s^{-1} yr^{-1} with a reduced χ^2 of 1.075 (180 degrees of freedom). While these masers reside in the same velocity range as Clump 6 and the measured accelerations are consistent, we found that only the dominant lines ($V \sim 10235$ to 10243 km s^{-1}) in this clump have consistent VLBI positions as Clump 6. This suggests that lines at other velocities may come from different rings. Therefore, in the distance determination we will exclude the masers having inconsistent VLBI positions and only use the maser spots between $V \sim 10235$ to 10243 km s^{-1}.

4.3 Acceleration Measurement for NGC 6323

We took 35 H_2O maser spectra with the GBT for NGC 6323 between 2003 December 16 and 2009 May 19. For the purpose of distance determination, we will only use the spectra from 21 epochs between 2006 October 30 and 2009 May 19 that bracket our VLBI observations. We break the whole observing period into three parts − Periods A, B, and C. These three periods are separated by summer months and we have four or five VLBI tracks within each period. As with NGC 6264, we attempt to measure accelerations for masers in each individual period rather than using all spectra at once because many maser lines flare and decay on timescales shorter than the whole period of our observation. In addition, maser lines at the same velocity range could have different accelerations at different periods. In Table 4.4 we show the observing dates and sensitivities for each of the spectra we use for acceleration measurement and in Figure 4.10 we show a representative H_2O maser spectrum for NGC 6323.

4.3.1 High Velocity Masers

In Figure 4.11, we plot the radial velocities of NGC 6323 maser peaks as a function of time. Similar to NGC 6264, we first identify the lines that are persistent in time and then fit a straight line to the data to measure the accelerations directly. We estimate the uncertainty of the measurements by scaling the fitting error by the square root of reduced χ^2 and conservatively increase the uncertainty by a factor of 2 to account for possible bias caused by blending. In Table 4.5, we show the measured accelerations and uncertainties.

The weighted average accelerations of the redshifted and blueshifted masers are -0.28 and -0.01 km s^{-1} yr^{-1} respectively. The rms scatter of acceleration of the redshifted and blueshifted masers are 0.23 and 0.20 km s^{-1} yr^{-1}. The small acceleration and rms scatter indicate that the high velocity masers are close to the mid-line of the accretion disk as expected. With the acceleration measurements and the scatter seen in the rotation curve of the high velocity masers, we can infer that the majority of the high velocity maser spots must fall within $\approx$15 degrees from the mid-line of the disk.

When assigning the measured accelerations to the corresponding channels in the VLBI datasets, we pay attention to whether the periods over which the accelerations are measured actually bracket the epochs of our VLBI observations. We have four tracks (BB231E, BB231F, BB231G, BB231H) of VLBI observations in Period A, five tracks (BB242F, BB242E, BB242G, BB242H, and BB242J) in Period B, and four tracks (BB242M, BB242R, BB242S, and BB242T[2]) in Period C. For those masers persisting over Periods A through C, we assign the measured accelerations to the corresponding VLBI channels from averaging all twelve tracks. For those masers that persist only one or two periods, we assign the accelerations only to the VLBI channels from data in the respective periods. For maser spots without acceleration measurements from the eye-balling method, we assume their accelerations to be zero and assign them to the data from averaging all twelve tracks. We adopt two times the rms scatter (0.46 and 0.40 km s^{-1} yr^{-1} for the redshifted and blueshifted masers) of the accelerations from the eye-balling method as their uncertainties.

---

[2] BB242T is not actually combined with other datasets because the systemic masers in this observation are rather weak. Combining this track with the other datasets decreases the signal-to-noise ratio for systemic masers. Although the high velocity lines still have decent sensitivity, we do not combine the high velocity part of this dataset with the others just for making the whole data combination easier. We only lose negligible signal-to-noise for the high velocity masers by ignoring this track.

4.3.2 Systemic Masers

The acceleration measurement for the systemic masers in NGC 6323 has been quite challenging mainly because of the joint effect of line blending and low signal-to-noise ratio of the spectra. As we can see in Figure 4.12, except for the masers in Period B (epochs 4 to 14), the masers at other epochs have flux densities lower than 15 mJy (i.e. $\sim 9\ \sigma$). For such blended spectra with substantial variability, only a few σ detections do not allow us to measure accurate and reliable accelerations for masers in Period A and C, and we only manage to measure accelerations for the more distinct and persistent maser lines or clumps in Period B. For the convenience of acceleration measurement, we divide the maser spectra of Period B into four clumps, and apply the GLOFIT program to measure accelerations with the assumption of constant drifting rate when possible.

Clumps 1 and 2

Clump 1 covers the velocity range from 7849.0 to 7851.0 km s^{-1}, and the drifting of the narrow maser line in this clump can be clearly seen in Figure 4.11. Its apparent acceleration measured by the eye-balling method is 1.74±0.17 km s^{-1} yr^{-1}. To deal with the variability in both flux density and linewidth more accurately, we fit one Gaussian component to this velocity range with the GLOFIT program. We obtain an acceleration of 1.64±0.17 km s^{-1} yr^{-1}, consistent with the result from the eye-balling fitting. The reduced χ^2 of the fit is 1.107 (30 degrees of freedom). We list the results of the measurement in Table 4.6.

The maser lines in Clump 2 cover the velocity range from 7852.3 to 7860.3 km s^{-1}. While the lines at this velocity range look relatively distinct and the blending issue does not seem serious, we do not successfully obtain a reliable fit for this clump.

We have attempted to fit five Gaussian components without assuming constant acceleration to this clump and the lowest reduced χ^2 we can obtain is 1.315. For a system of 81 degrees of freedom, the probability to achieve a reduced χ^2 of 1.315 is less than a few percent. In addition, the measured accelerations range from 2.11 to 4.42 km s^{-1} yr^{-1} with typical error bar $\sim$ 0.8 km s^{-1} yr^{-1}. For accelerations as high as these values, we expect to see clear line drifting in the spectra and in the time-velocity plot by eye directly. However, when we inspect all spectra from epoch 4 through 14 together carefully, we do not see the expected line drifting. What we actually see instead is that the line structure varies substantially with time. The maser lines rise and decay on a timescale of just a few months, and the newly arising lines are probably not the flare of the decayed lines appearing at different velocities because of different accelerations. It is possible that such high variability confuses our GLOFIT program to think that these maser lines drift with high accelerations. Judging by eye, it appears that the majority of the maser lines in Clump 2 cannot drift faster than $\sim$1.5 km s^{-1} yr^{-1}. Since we cannot obtain reliable accelerations for the masers in this clump, we will ignore these masers in the distance determination.

Clump 3

The maser lines in Clump 3 are clearly more blended. However, since the shape of the pattern of Clump 3 remains persistent and the clump clearly drifts toward high velocity with time, we can use the whole pattern to constrain the acceleration. We fit four Gaussian components to the masers between 7864.0 to 7873.0 km s^{-1} by assuming that all components have the same acceleration. The best fit reduced χ^2 is 0.991, and we obtain an acceleration of 1.40 ± 0.16 km s^{-1} yr^{-1}.

Clump 4

Clump 4 covers the velocity range between 7873.8 to 7883.8 km s^{-1} and consists of two sub-clumps. The major clump resides in the velocity range between 7876.5 to 7883.8 km s^{-1} and the minor clump resides between 7873.8 to 7876.5 km s^{-1}. When applying the modified GLOFIT program to the masers in Clump 4, we assume both the major and minor clump have the same acceleration, which is suggested by the measurements from the eye-balling method. We fit five Gaussian components to the spectra and obtained an acceleration of 0.53 ± 0.16 km s^{-1} yr^{-1}. The reduced χ^2 we achieve is 1.001 (166 degrees of freedom). To check whether both sub-clumps really have the same acceleration, we have measured the acceleration for each individual sub-clump and the results are consistent. Therefore, we are confident on our constant acceleration assumption for Clump 4.

Table 4.1. Observing dates and sensitivities for NGC 6264

Epoch	Date	Day Number	T_{sys} (K)	rms Noise (mJy)	Period
0	2008 November 21	0	30.9	1.7	A
1	2009 January 16	56	28.2	1.3	A
2	2009 February 3	74	35.9	1.3	A
3	2009 March 4	103	31.9	1.2	A
4	2009 March 31	130	37.8	1.4	A
5	2009 May 13	172	41.5	1.7	A
6	2009 November 7	351	44.3	1.7	B
7	2009 December 12	386	27.4	1.5	B
8	2010 January 11	416	26.3	1.1	B
9	2010 February 9	445	39.0	1.5	B
10	2010 March 7	471	28.3	1.5	B
11	2010 April 13	507	36.8	2.2	B
12	2010 May 10	534	28.2	1.2	B
13	2010 July 2	588	40.3	2.2	B
14	2010 October 30	708	40.2	1.7	C
15	2010 November 26	735	38.4	1.5	C
16	2010 December 24	763	30.3	1.5	C
17	2011 January 23	793	31.4	1.2	C
18	2011 February 7	808	42.7	1.4	C
19	2011 March 2	831	39.0	2.3	C

Note. — The sensitivities are calculated without performing Hanning smoothing to the spectra and are based on 0.33 km s^{-1} channels. We label Period A, B, and C to those times when we have continuous observations in a monthly timescale. These periods are separated by summer months during which the humidity makes observations inefficient.

Table 4.2. Acceleration Measurements for the High Velocity Masers in NGC 6264

Velocity (km s^{-1})	Acceleration (km s^{-1} yr^{-1})	σ_{accel} (km s^{-1} yr^{-1})
10749.05	0.02	0.14
10751.24	−0.07	0.04
10753.28	−0.03	0.08
10755.20	−0.10	0.10
10766.50	−0.26	0.03
10776.50	−0.30	0.42
10781.77	−0.13	0.02
10793.18	−0.05	0.10
10798.96	−0.27	0.11
10802.19	−0.09	0.08
10809.58	−0.17	0.06
10824.78	0.27	0.34
10826.46	−0.75	0.73
10837.53	−0.16	0.08
10840.21	−0.27	0.06
10841.58	−0.04	0.05
10845.09	0.16	0.06
10848.68	0.00	0.11
10873.30	0.00	0.16
10912.41	0.11	0.60
9480.57	−0.09	0.07
9490.42	0.14	0.55
9536.46	0.15	0.420
9534.93	−0.44	0.17
9550.39	0.19	0.12
9595.16	−0.13	0.08
9601.54	−0.28	0.08
9611.70	0.11	0.10
9614.70	−0.12	0.06
9630.99	0.23	0.08
9636.43	−0.04	0.07
9667.88	0.09	0.10
9679.29	0.29	0.08
9692.04	0.17	0.10
9787.36	0.02	0.03
9811.77	0.05	0.06

Note. — The acceleration measurements for the high velocity masers. The components having velocity higher than 10745 km s^{-1} are redshifted masers whereas those having velocity lower than 9815 km s^{-1} are blueshifted masers

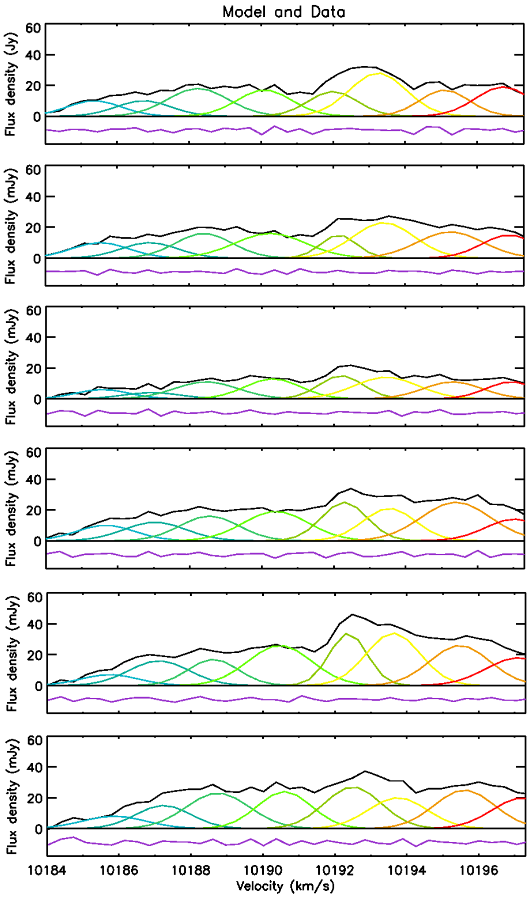

Fig. 4.9.— An example of the Gaussian decomposition for the acceleration measurement. In this example, we fit the masers between 10183.0 and 10197.7 km s^{-1} in the spectra. The panels from top to bottom show the spectra (lines with black color) from epoch 0 through 5. Each of the eight Gaussian components fitted to the data are represented by different colors. The purple curves at the bottom of each panel are the residuals from the fit.

Table 4.3. Acceleration Measurements for the Systemic Masers in NGC 6264

Clump	Velocity Range (km s^{-1})	Epochs	Num. of Components	Linewidth (km s^{-1})	Acceleration (km s^{-1} yr^{-1})	σ_{accel} (km s^{-1} yr^{-1})	χ^2_ν	d.o.f.
1	10183.0 − 10197.7	0 − 5	8	1.9	1.04	0.14	1.144	153
1	10200.2 − 10203.5	0 − 5	2	1.9	0.75	0.10	0.966	40
2	10184.0 − 10201.6	6 − 11	9	2.0	1.12	0.18	1.009	183
3	10209.1 − 10228.0	1 − 5	11	1.7	1.55	0.23	1.440	144
5	10218.9 − 10226.8	6 − 9	4	1.7	1.79	0.36	1.126	52
6	10226.0 − 10252.3	0 − 5	10	2.4	4.43	0.36	1.006	314
7	10230.5 − 10250.5	7 − 11	9	2.3	3.96	0.59	1.075	180

Note. — Col(1): The clump number; Col(2) The velocity range for acceleration measurement; Col(3) The epochs of the spectra used for fitting; Col(4) The number of Gaussian components that fit the data; Col(5) The average linewdith of fitted lines; Col(6) The best fit acceleration; Col(7) The uncertainty of the acceleration; Col(8) The reduced χ^2 of the fit; Col(9) The number of degrees of freedom of the fit.

Table 4.4. Observing dates and sensitivities for NGC 6323

Epoch	Date	Day Number	T$_{sys}$ (K)	rms Noise (mJy)	Period
0	2006 October 23	192	42.4	2.2	A
1	2006 December 2	225	36.0	1.4	A
2	2007 February 22	307	44.0	2.2	A
3	2007 April 6	350	35.9	1.8	A
4	2007 October 29	556	34.3	1.4	B
5	2007 November 28	586	35.7	1.6	B
6	2007 December 26	614	55.0	2.9	B
7	2008 February 2	652	39.3	1.5	B
8	2008 February 29	679	44.0	1.7	B
9	2008 March 25	704	34.2	1.3	B
10	2008 April 24	734	56.5	1.8	B
11	2008 May 6	746	41.1	2.4	B
12	2008 May 29	769	49.4	2.0	B
13	2008 September 29	892	47.7	2.2	C
14	2008 October 31	924	43.5	1.7	C
15	2008 November 28	952	35.9	1.1	C
16	2008 December 29	983	35.2	1.3	C
17	2009 January 30	1015	33.8	1.1	C
18	2009 March 4	1048	31.5	1.2	C
19	2009 March 31	1075	38.2	1.3	C
20	2009 May 19	1124	35.3	1.5	C

Note. — The sensitivities are calculated without performing Hanning smoothing to the spectra and are based on 0.33 km s^{-1} channels. We label Period A, B, and C to those times when we have continuous observations on a monthly timescale. These periods are separated by summer months during which the humidity makes observations inefficient.

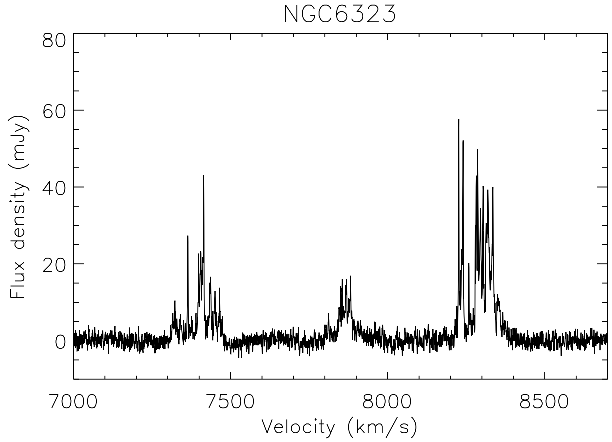

Fig. 4.10.— A representative spectrum for NGC 6323. This spectrum was observed on 2008 May 29.

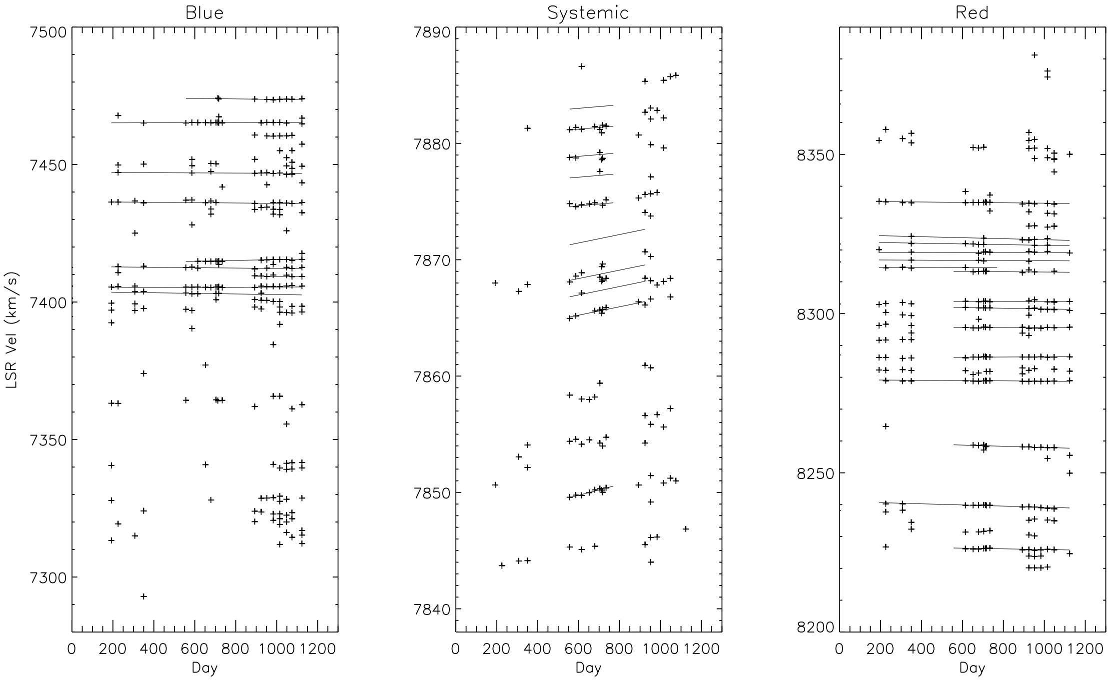

Fig. 4.11.— In this figure, we plot the radial velocities of NGC 6323 maser peaks as a function of time (the crosses) along with the fitting results from the eye-balling method (for the high velocity masers) or from the modified GLOFIT program (for the systemic masers).The data between Day 0 and 400 come from spectra taken in Period A; the data between Day 400 to 800 from spectra in Period B; and the data between Day 800 to 1200 are from spectra in Period C.

Table 4.5. Acceleration Measurements for the High Velocity Masers in NGC 6323

Velocity (km s^{-1})	Acceleration (km s^{-1} yr^{-1})	σ_{accel} (km s^{-1} yr^{-1})
8335.94	−0.22	0.10
8326.44	−0.58	0.28
8323.69	−0.40	0.30
8319.39	−0.04	0.28
8317.24	−0.11	0.28
8314.17	0.07	0.34
8313.99	−0.17	0.34
8304.12	−0.06	0.20
8303.64	−0.38	0.30
8295.83	−0.04	0.14
8285.81	0.11	0.06
8279.68	−0.16	0.08
8261.80	−0.68	0.12
8242.88	−0.66	0.16
8228.13	−0.40	0.32
7475.58	−0.34	0.20
7464.98	0.05	0.08
7447.45	−0.11	0.08
7437.15	−0.22	0.22
7412.49	0.52	0.16
7413.63	−0.25	0.36
7411.38	−0.37	0.70
7404.73	0.13	0.20
7404.93	−0.39	0.34

Note. — The acceleration measurements for the high velocity masers. The components having velocity higher than 8000 km s^{-1} are redshifted masers whereas those having velocity lower than 7500 km s^{-1} are blueshifted masers

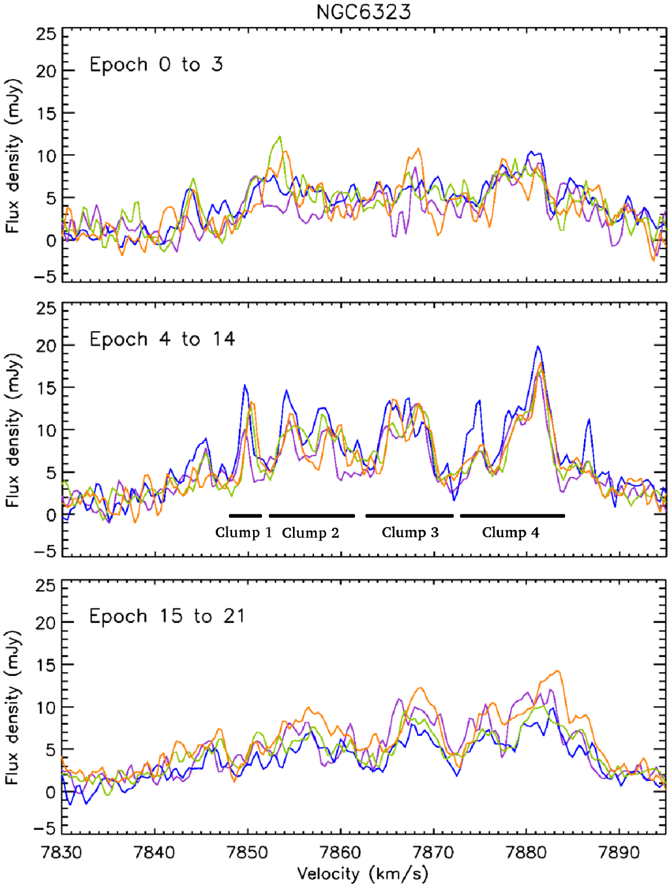

Fig. 4.12.— The upper panel shows the spectra from epochs 0 through 3 (purple, blue, green, and orange), the middle panel shows the representative spectra (epoch 4/purple, 6/blue, 8/green, 10/orange) from epochs 4 to 14, and the bottom panel shows the representative spectra (epoch 13/purple, 15/blue, 17/green, 19/orange) from epochs 15 through 21. Because of both severe blending and low signal-to-noise, we only manage to measure the accelerations for masers between epochs 4 and 14. We divide the velocity range of interest into four sections for the convenience of acceleration measurement.

Table 4.6. Acceleration Measurements for the Systemic Masers

Clump	Velocity Range ($\mathrm{km\ s^{-1}}$)	Epochs	Num. of Components	Linewidth ($\mathrm{km\ s^{-1}}$)	Acceleration ($\mathrm{km\ s^{-1}\ yr^{-1}}$)	σ_{accel} ($\mathrm{km\ s^{-1}\ yr^{-1}}$)	χ^2_ν	d.o.f.
1	7849.0 − 7851.0	4 − 12	1	1.6	1.64	0.17	1.107	30
3	7864.0 − 7873.0	4 − 14	4	2.0	1.40	0.16	0.991	161
4	7873.8 − 7883.8	4 − 12	5	2.1	0.53	0.16	1.001	166

Note. — Col(1): The clump number; Col(2) The velocity range for the acceleration measurement; Col(3) The epochs of the spectra used for fitting; Col(4) The number of Gaussian components that fit the data; Col(5) The average linewdith of fitted lines; Col(6) The best fit acceleration; Col(7) The uncertainty of the acceleration; Col(8) The reduced χ^2 of the fit; Col(9) The number of degrees of freedom of the fit.

Chapter 5

The Determination of the Angular-Diameter Distance for NGC 6264 and NGC 6323

In chapter 1 we described how one can determine the angular-diameter distance to a megamaser galaxy by measuring four orbital parameters of a H_2O maser disk which exhibits Keplerian rotation:

$$D = \frac{V_0^2}{a\ \Delta\theta}\ sin\ i\ , \tag{5.1}$$

where V_0 is the orbital velocity observed along the line-of-sight, $\Delta\theta$ is the angular radius of an orbit, and a is the observed acceleration of the systemic masers on the orbit. In principle, V_0, $\Delta\theta$, and i can be inferred from the rotation curve of the accretion disk (see section 1.3) and a can be measured with H_2O maser spectra from multi-epoch monitoring. However, in practice V_0 and $\Delta\theta$ are not measured from the rotation curve directly, and it is more convenient to re-express Equation 5.1 in terms of the observables of the rotation curve:

$$D = a^{-1}\ k^{2/3}\ \Omega^{4/3}\ . \tag{5.2}$$

In this equation, k is the curvature parameter from the Keplerian rotation curve fit to the high velocity masers : $v = k(\theta - \theta_0)^{-1/2} + V_{sys}$, where θ_0 is the position of the dynamical center of the disk, and v_{sys} is the recession velocity of the galaxy; $\Omega \equiv dv/d\theta$ is the slope of the line traced by the systemic masers in the position-velocity (P-V) diagram.

This simple approach to measuring distance has been quite successful for the poster child maser galaxy NGC 4258, and the simple extension of this method to a two-ring model also provided a good maser distance to UGC 3789 (Braatz et al. 2010). However, for the two main galaxies in this thesis, NGC 6264 and NGC 6323, this method is not the best approach. As we have seen in chapter 4, the systemic masers in NGC 6264 and NGC 6323 have several different accelerations, and this means that different masers reside at different radial distances from the black holes. In addition, for each group of masers that reside in a particular ring, we only have at most five VLBI data points in the P-V diagram. Therefore, even if a group of masers show a clear linear trend in the P-V diagram, the fitting error is large if only one group of maser spots is used in the fit.

As an example, in Figure 5.1 we show the P-V diagram of the systemic masers in NGC 6264. The maser spots are color-coded to indicate different groups of masers. We assign a unique color to those maser spots residing in the same ring and having the same acceleration. The accelerations of the five groups of masers range from 0.74 to 4.43 km s^{-1} yr^{-1}. Clearly, we cannot apply the simple approach adopted for NGC 4258 and UGC 3789 to NGC 6264 directly. In this P-V diagram, only the purple maser group shows a linear trend. If we only use this group of masers to fit Ω, we can achieve a distance measurement accurate to only ~30%. The situation in NGC 6323 is even worse because there are fewer data points and none of the maser groups show clear trends. So, it is apparent that using a one- or two-ring model is not sufficient to measure precise distances for these two galaxies.

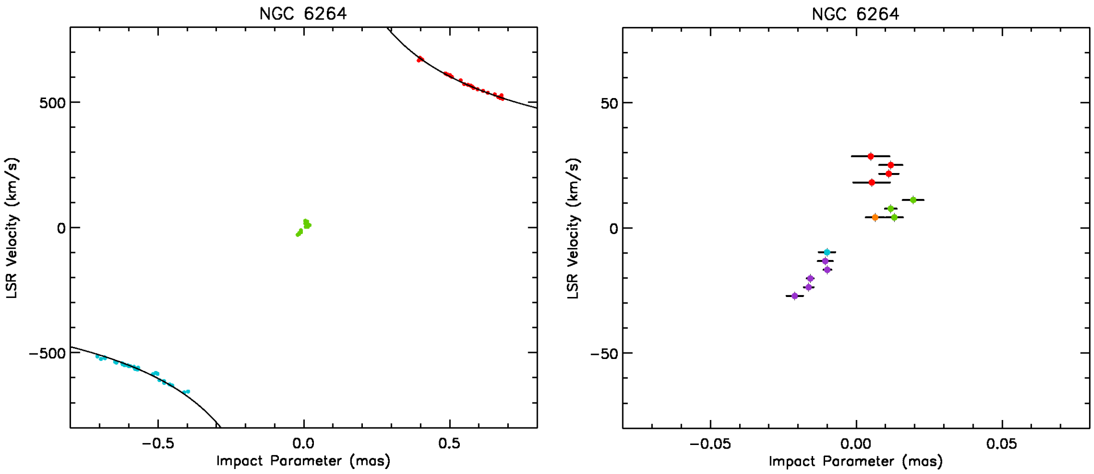

Fig. 5.1.— The left panel shows the Position-Velocity (P-V) diagram for the maser disk in NGC 6264. The red, green, and blue colors assigned to the maser spots indicate the redshifted, systemic, and blueshifted masers, respectively. The right panel shows the P-V diagram only for the systemic masers. We assign a unique color to maser spots from each ring, with each maser ring having its own acceleration : 1.07 km s^{-1} yr^{-1} for purple, 0.74 km s^{-1} yr^{-1} for blue, 1.79 km s^{-1} yr^{-1} for green, 1.55 km s^{-1} yr^{-1} for orange, and 4.43 km s^{-1} yr^{-1} for red.

To deal with this complicated situation, we apply two methods to make use of all maser spots with different accelerations to constrain the distances. In the method of *ensemble fitting*, we obtain the distance by fitting the P-V diagram of the systemic masers with a multiple-ring model, whereas in the method of *Bayesian fitting*, we fit the maser disk in three dimensions based on Bayesian analysis using both high-velocity and systemic masers.

5.1 Method 1: Ensemble Fitting

5.1.1 The Method

If one knows the position of dynamical center (θ_0) and the recession velocity of the galaxy (v_{sys}), in principle one can determine the maser distance with just *one* maser spot (call it p_1). Assuming that the impact parameter of this maser spot is θ_1 and its velocity is v_1, one can measure the "slope" of this maser spot with

$$\Omega = (v_1 - v_{sys})/(\theta_1 - \theta_0). \tag{5.3}$$

Given the acceleration measurement for this maser spot and k measured from the rotation curve of the high velocity masers, one can directly determine the distance (D_1) with Equation 5.2.

Conversely, one can predict the position of a systemic maser spot on the P-V diagram with its observed velocity and acceleration if one knows θ_0, v_{sys}, and D (assuming the k parameter from fitting the high velocity masers has been measured). Therefore, if one has a number of systemic maser spots with good acceleration measurements, one can in principle measure the distance by fitting the P-V diagram of the systemic masers with a model computed from the fitting parameters (θ_0, v_{sys}, D). We explain the details as follows.

Suppose that we have an accretion disk with maser spots residing in n different rings. For the masers residing at the i-th ring of the disk, one can predict their impact parameters in the P-V diagram by re-writing Equation 5.3 as

$$\theta_{ij}^{(m)} = \frac{(v_{ij} - v_{sys})}{\Omega_i} + \theta_0 \ , \tag{5.4}$$

where $\theta_{ij}^{(m)}$ denotes the model impact parameters for the j-th maser spot at the i-th ring, v_{ij} is its observed velocity, and Ω_i is the slope of the i-th ring in the P-V diagram. Based on Equation 5.2, one can express Ω_i in terms of D_*, k, and the observed acceleration of the i-th ring a_i:

$$\Omega_i = \left(\frac{a_i\, D_*}{k^{2/3}}\right)^{3/4} . \tag{5.5}$$

Since the error δa_i of the acceleration measurement a_i is usually nonnegligible, these uncertainties will introduce errors in the model impact parameters:

$$\delta\theta_{ij}^{(m)} = \frac{3}{4}\,(\theta_{ij}^{(m)} - \theta_0)\,\frac{\delta a_i}{a_i}. \tag{5.6}$$

In the fitting, we add the error in the model impact parameter $\delta\theta_{ij}^{(m)}$ to the measurement error $\delta\theta_{ij}^{(d)}$ in quadrature to obtain the total error in the impact parameter $\delta\theta_{ij}$.

With the above equations, we can write the χ^2 of the fit as

$$\chi^2 = \Sigma_{ij}\frac{(\theta_{ij}^{(d)} - \theta_{ij}^{(m)})^2}{\delta\theta^2} , \tag{5.7}$$

where $\theta_{ij}^{(d)}$ is the impact parameter of the j-th maser spot at the i-th ring from the real data.

When one has external constraints on θ_0 and v_{sys}, one can impose these constraints to the fitting by adding the respective χ^2 to Equation (5.7):

$$\chi^2 = \Sigma_{ij}\frac{(\theta_{ij}^{(d)} - \theta_{ij}^{(m)})^2}{\delta\theta^2} + \frac{(\theta_0 - \theta_{ext})^2}{\delta\theta_{ext}^2} + \frac{(v_{sys} - v_{ext})^2}{\delta v_{ext}^{\,2}} , \tag{5.8}$$

where θ_{ext} and v_{ext} are the position of the black hole and recession velocity of the galaxy from external constraints, and $\delta\theta_{ext}$ and δv_{ext} are the corresponding uncertainties.

Finally, we minimize the χ^2 to find the best (θ_0, v_{sys}, D) that fit the data.

5.1.2 Distance to NGC 6264

Before applying the ensemble fitting method to measure the distance to NGC 6264, we first rotated the coordinate system to make the disk horizontal and used the fitted horizontal line that passes through the high velocity masers as the zero point of the y-coordinate of the dynamical center. The zero point of the x-coordinate is defined to be the unweighted average θ_{x} of the systemic masers. The impact parameter of each maser spot is defined as the angular distance of the maser in the x-axis from the zero point. Note that the zero point of the x-coordinate may not be the same as the position of the dynamical center in the x-axis, and one needs to include the actual x-position of the dynamical center (θ_0) as a fitting parameter in the distance determination. We plot the rotated maser disk in NGC 6264 in the left panel of Figure 5.2.

In the right panel of Figure 5.2, we show the detailed distribution of the systemic maser spots. All the systemic masers except masers in ring 3 have very similar y offset, and this indicates that their inclinations should be similar. These masers have an average y offset of -0.008 mas, and we adopt this value to estimate their orbital inclinations with Equation (1.15):

$$i \;=\; cos^{-1}(\frac{y}{\Delta\theta}) \;=\; cos^{-1}(\frac{y\sqrt{aD}}{k}) \;. \tag{5.9}$$

With the acceleration measured for each ring and assuming D = 139.4 Mpc, the estimated inclinations of Ring 1, 2, 4, and 5 are 89.1°, 89.3°, 88.9°, and 88.2°, respec-

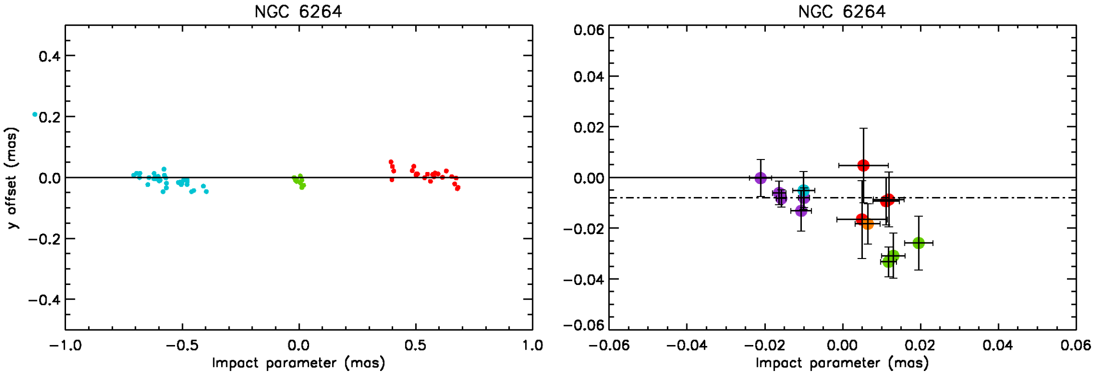

Fig. 5.2.— The left panel shows the rotated maser disk in NGC 6264. The red, green, and blue colors assigned to the maser spots indicate the redshifted, systemic, and blueshifted masers, respectively. Here, we adopt the convention that the redshifted masers have positive impact parameters. The right panel shows the distribution of the systemic masers in the rotated disk. We assign colors to the systemic masers as in Figure 5.1. In the following discussion, we call the ring at which the masers with purple color reside ring 1. We call ring 2 for the masers with blue color, ring 3 for green, ring 4 for orange, and ring 5 for red.

tively. Note that since the inclinations are close to 90°, and the line-of-sight velocities ($V_{\|}$) of the systemic maser spots observed in the local frame are less than 35 km s^{-1}, the inclination corrections for the observed velocities $V_{\rm obs}$ of the systemic masers are negligible:

$$\Delta V_{\rm obs} = V_{\|}\ (1 - sin\ i) \sim 0.0002\ V_{\|} < 0.007 \text{ km s}^{-1}. \tag{5.10}$$

Therefore, the impact of the orbital inclinations of the systemic masers on the distance determination can be ignored.

As a group, the masers in ring 3 have a substantially larger y offset (-0.030 mas), which suggests that the ring has an inclination of ~ 85.7 °. Therefore, ring 3 has the largest offset from being edge-on among all of the systemic rings. This is puzzling because base on the acceleration of the masers in this ring we can infer that the radius of ring 3 should be close to the median value of the radii of the other rings.

Since the inclination/warping angle should a smooth function of the radius of the disk if the disk warping is caused by a single mechanism, ring 3 should have a y offset similar to other rings, but this is not the case. Therefore, this suggests that either our acceleration measurement is wrong[1], or there may be other reasons for ring 3 to have a larger y offset. To avoid systemic error in the distance determination, we exclude the masers in ring 3 in our analysis.

So, for NGC 6264 we model the systemic masers as a 4-ring system, and fit the model to the data with three free parameters (θ_0, v_{sys}, D). The zero point of the x-coordinate is recalculated by excluding masers from ring 3. The application of the ensemble fitting method gives a distance of 150.5±33.6 Mpc (22% accuracy). The corresponding Hubble constant is H_0 = 66.7±14.7 km s^{-1} Mpc^{-1}. The best fit position of the black hole and the recession velocity of the maser disk are 0.0102±0.0039 mas and 10217.6±7.8 km s^{-1}, respectively. The reduced χ^2 of the fit is 0.46 (8 degrees of freedom).[2] We show the fitting of the systemic masers in Figure 5.3.

While the measured distance to NGC 6264 is close (∼8%) to the expected value 139.4 Mpc estimated from the current best H_0, the 22% uncertainty is still too large to measure a precise H_0. It is possible to improve the distance precision significantly if we have good *a priori* information for x_0 and v_{sys}. A possible way to constrain (x_0, v_{sys}) is to fit the rotation curve of the high velocity masers with x_0 and v_{sys} as free parameters. In principle, the symmetry of the Keplerian rotation curve with respect to the center of the P-V diagram should give a tight constraint on (x_0, v_{sys}).

---

[1] An incorrect acceleration measurement is possible for ring 3 because of the significant changes in the maser pattern at different epochs and the apparent sudden increase of the acceleration at later epochs in our observation (see section 4.2.2.4 in Chapter 4). These complexities could imply that the actualy behaviour of the maser lines is more complicated than our model that fits the spectra, and if this is the case, there could be significant systematic error in our acceleration measurement.

[2] The probability to get a reduced χ^2 of 0.483 for a 8 degree-of-freedom system is $\sim$ 13%. Although a low reduced χ^2 usually suggests that the uncertainties are overestimated, we take a conservative approach to use the *unscaled* distance uncertainty to include any unaccounted systematic errors.

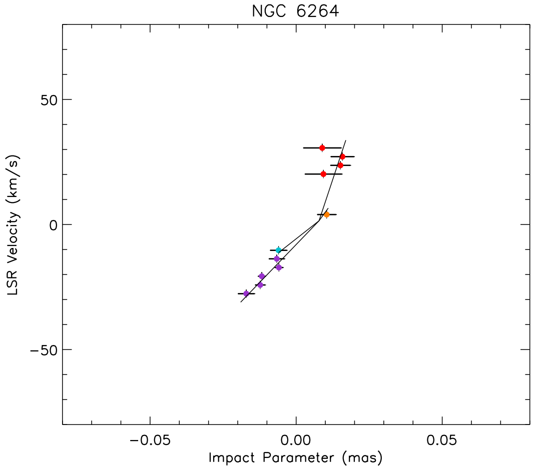

Fig. 5.3.— In this figure, we plot the results (the solid lines) from ensemble-fitting on the position-velocity diagram of the systemic masers in NGC 6264. The best fit distance to NGC 6264 is 150.8±32.8 Mpc (22% accuracy).

However, since the high velocity maser spots are generally not located on the mid-line of the disk exactly, the deviations introduce extra scatter in the observed rotation curves. Because of this extra scatter, we usually can only achieve a reduced χ^2 of ∼10, which limits the accuracy we can achieve for x_0 and v_{sys} to ∼20 μarcsec and ∼10 km s^{-1}, respectively. Therefore, the constraints from the high velocity rotation curve fitting are insufficient to improve the distance measurement with the ensemble-fitting method. A better way to obtain tighter constraints on x_0 and v_{sys} is to model the maser disk in three dimensions. This will allow us to model the deviations of the high velocity masers from the mid-line and give a more accurate measurement of (x_0, v_{sys}). We will explore this possibility in section 5.2.

5.1.3 Distance to NGC 6323

We follow the same approach to define the coordinate system and impact parameter as in NGC 6264. The maser distribution in the disk is shown in the left panel of

Figure 5.4. In the right panel, one can see that the systemic masers are apparently located above the plane defined by the high velocity masers and have a positive y offset of 0.13 mas. Because the signal-to-noise ratio is relatively poor, we use the average maser radius to estimate the inclination of the orbits even though we know that different systemic masers may reside at different radii. The average inclination is 91.7°, and the corresponding velocity correction is less than 0.013 km s^{-1}, which is negligible for distance determination.

While there are 13 systemic maser spots available for the distance fitting, we actually use only 7 of them because the other 6 do not have reliable acceleration measurements. The extremely faint systemic masers in this galaxy have made accurate acceleration measurements difficult, and prevent us from achieving precise VLBI astrometry for distance measurement. By applying the ensemble fitting method to NGC 6323, we get a distance of 60.0±70.0 Mpc with a reduced χ^2 of 0.5 (4 degrees of freedom). We show the fitting result in the left panel of Figure 5.5.

While the ensemble-fitting method is not successful for measuring a good distance to NGC 6323, it may be better to just use the average velocity gradient and average acceleration of the systemic to estimate the distance to zero-th order. We use the average velocity gradient (Ω = 821.4±239.8 km s^{-1} yr^{-1}) of these masers and their (weighted) average acceleration (a =1.06±0.08 km s^{-1} yr^{-1}) to measure the distance with Equation (5.1), and we obtain a result of 65.5±26.0 Mpc (40% accuracy). So, to the zero-th order, the maser distance is consistent with the expected distance (D ∼106 Mpc) from the current best Hubble constant to ∼1.5 σ. However, the current distance uncertainty is still too large to achieve an accurate Hubble constant measurement, and therefore we will need to continue to improve the sensitivity and angular resolution of our observations on this galaxy in order for a better Hubble

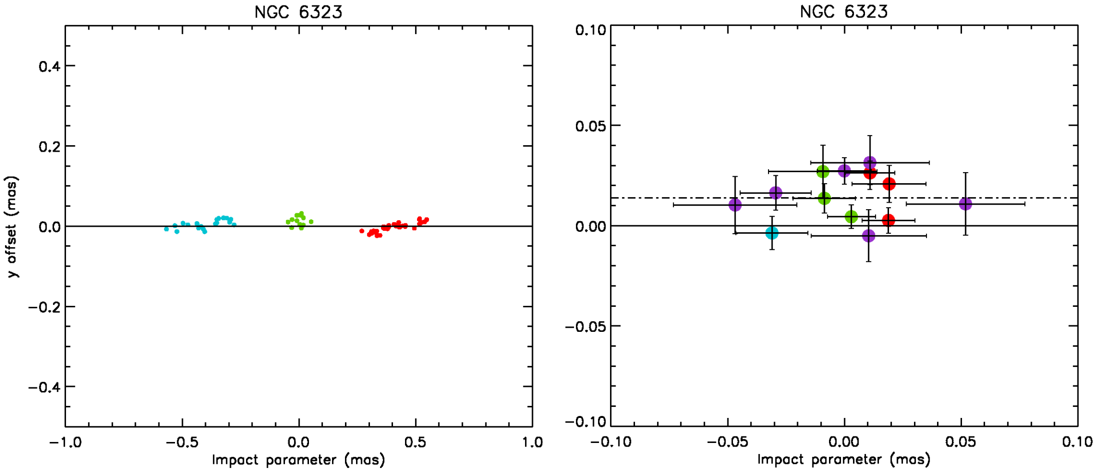

Fig. 5.4.— The left panel shows the rotated maser disk in NGC 6323. The red, green, and blue colors assigned to the maser spots indicate the redshifted, systemic, and blueshifted masers, respectively. Here, we adopt the convention that the redshifted masers have positive impact parameters. The right panel shows the distribution of the systemic masers in the rotated disk. The red spots represent the masers with an acceleration of 0.53±0.16 km s^{-1} yr^{-1}, the greens have an acceleration of 1.40±0.16 km s^{-1} yr^{-1}, the blue has an acceleration of 1.64±0.17 km s^{-1} yr^{-1}, and the purples are the maser spots without reliable acceleration measurements.

constant determination.

5.2 Method 2: Bayesian Fitting

In the Bayesian fitting method, we fit the maser disk in three dimensions by using all information available for both high-velocity and systemic masers. Although less intuitive, this approach is better than the ensemble-fitting method for measuring the distance to a maser galaxy because not only can it model the orbital parameters (e.g. warping and inclination angles) better and measure the impact parameters more precisely, modeling the maser disk in three dimensions can also help place tight constraints on the position of the black hole and the recession velocity of the galaxy,

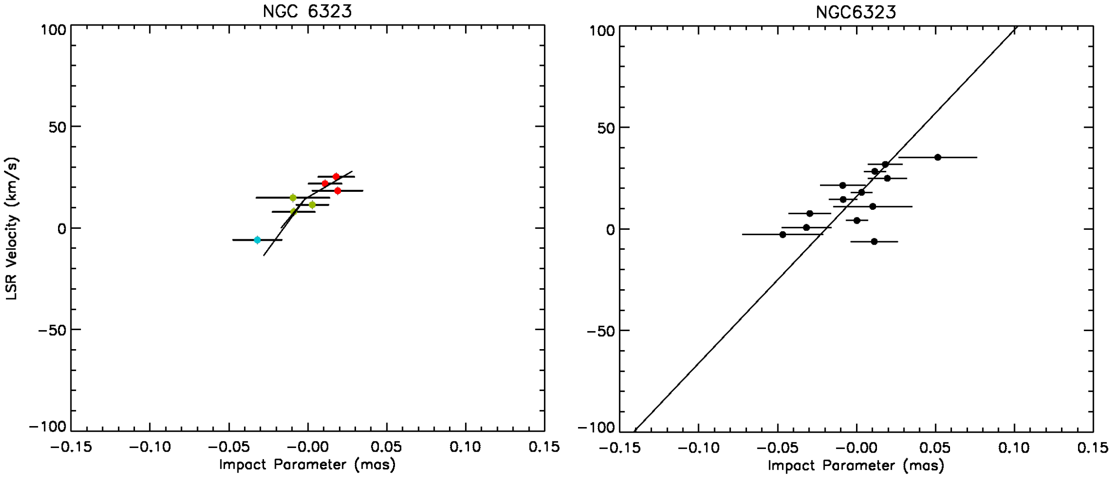

Fig. 5.5.— The left panel shows the P-V diagram of the systemic masers with good acceleration measurements in the ensemble-fitting for NGC 6323. We only adopt the data from Period B in the fitting because there is no reliable acceleration measurements for the data taken in Period A & C. The right panel shows the P-V diagram of the systemic masers including the spots with no reliable acceleration measurements. We use the average velocity gradient (Ω = 821.4±239.8 km s^{-1} yr^{-1}) of these masers and their average acceleration (a =1.06 km s^{-1} yr^{-1}) to make an zero-th order estimate of the maser distance to NGC 6323.

both of which are very useful for obtaining a precise maser distance. In addition, the Bayesian analysis allows one to use all prior information for the model parameters to constrain the fitting more easily, and this can help guide the fitting to find the most likely solutions efficiently and reliably. Furthermore, rather than seeking a single (best) solution and formal uncertainties, the Bayesian approach can directly probe the probability distribution of parameters without the assumption that the uncertainties follow the Gaussian distribution. Finally, one can more easily model the eccentricity of the disk in three dimensions, and directly measure its impact in the distance determination with the H_2O megamaser method.

The fitting program we are currently using was provided by Mark Reid. In this program, one constructs the model of the maser disk by placing each maser spot at radius r and disk azimuth angle ϕ (with $\phi \approx 0°$ for systemic masers and $\phi \approx 90°$ for redshifted masers) on an elliptical orbit about a point of mass M at the distance D. The center of the maser disk on the sky is (x_0, y_0), and its recession velocity is v_{sys}. Given a set of model parameters including D, M, x_0, y_0, v_{sys}, and parameters for disk warping and eccentricity, the program adjusts r and ϕ to best fit the data. The disk can be warped in two dimensions: the inclination warp $i(r)$ and the position-angle warp $\alpha(r)$, each of which is specified by 3 parameters:

$$i(r) \; = \; i_0 \; + \; i_i r \; + \; i_2 r^2 \; , \tag{5.11}$$

$$\alpha(r) \; = \; \alpha_0 \; + \; \alpha_i r \; + \; \alpha_2 r^2 \; , \tag{5.12}$$

where r is the radius of the orbit in milli-arcsec. In the fitting, one can choose how many of these parameters one should actually use depending on the degree of warping.

The program adopts a Markov chain Monte Carlo (McMC) approach (e.g. Geyer 1992; Gilks, Richardson & Spiegelhalter 1996) to obtain the probability distribution function of the model parameters. In this approach, one fits the data in a "brute force" manner by randomly trying a large number of model parameter values. Because of the "Markov chain" nature of the parameters, the $i^{th} + 1$ trial parameter values are dependent on, and close to, the i^{th} values. In particular, this program uses the Metropolis-Hastings algorithm (e.g. Metropolis et al. 1953; Hastings 1970; Chib & Greenberg 1995; Gelman, Gilks, & Roberts 1997) to choose the Markov-chain trial parameters. This algorithm has the property that the distribution of the trial parameter values is equal to the desired probability distribution function of the parameters.

5.2.1 Distance to NGC 6264 with the Circular Orbit Assumption

To apply the Bayesian fitting program to NGC 6264, we first assume the maser orbits to be circular and set the eccentricity parameters to be zero. We adopt *flat* priors for all parameters except for distance and recession velocity of the galaxy. The prior for the recession velocity of the galaxy, 10177±28 km s^{-1}, is taken from an optical observation by Beers et al. (1995). We deliberately increase the uncertainty of the recession velocity by a factor of 2 as an estimate of the systematics. In order to measure the distance independently from other observations, we adopt a weak prior assumption that there is a 68% probability for the H_0 to be between 50 to 100 km s^{-1} Mpc^{-1}, and use this assumption to constrain the distance with the Hubble law in the Bayesian fitting. With this prior, we determine the distance to NGC 6264 to be 149.2±19.8 Mpc (13.2%). The corresponding Hubble constant is 67.3±9.1 km s^{-1} Mpc^{-1} (assuming the peculiar velocity of the galaxy is 300 km s^{-1}), consistent with the current best H_0 measured in the optical. We show the best fit parameters and their uncertainties in Table 5.1, and present the probability distribution of the distance in Figure 5.6. We show the model maser distribution in Figure 5.7.

To make a distance measurement totally independent of any knowledge of H_0, we also tried to use a flat prior for the distance in the fitting. The distance we obtain is 150.0±21.0 (15%), and the probability distribution for distance is similar to that in Figure 5.6. So, except that the uncertainty increases by 2%, the distance measurement is nearly the same as the result from weak prior.

Finally, as we discussed in the previous section, it is possible to obtain a more accurate distance with the ensemble-fitting method if one has tighter constraints on x_0 and v_{sys}. In Table 5.1, we can see that the 3-dimensional Bayesian modeling

Table 5.1. The Best Fit Model Parameters for NGC 6264

D (Mpc)	M$_{BH}$ (10^7 $M_\odot$)	v_{sys} (km s^{-1})	x$_0$ (μarsec)	y$_0$ (μarsec)	i_0 ($^\circ$)	i_1 ($^\circ$/mas)	α_0 ($^\circ$)	α_1 ($^\circ$/mas)	α_2 ($^\circ$/mas^2)
149.2±19.8	3.13±0.42	10210.9±1.1	5±2	7±3	89.0±2.4	1.1±3.7	84.5±4.1	16.5±11.2	1.1±7.1

Note. — Col(1): The distance to NGC 6264; Col(2) The black hole mass; Col(3) The recession velocity of the galaxy; Col(4) The position of the dynamical center in the RA coordinate; Col(5) The position of the dynamical center in the DEC coordinate; Col(6)−(7) The parameters for the inclination warp ; Col(8)−(10) The parameters for the position-angle warp. Note that we do not include the i_2 term in the fitting because as we have inferred in section 5.1.2, all the four rings in the fitting have very similar inclinations. This implies that the degree of the inclination warp is small and therefore including the i_2 term is not necessary.

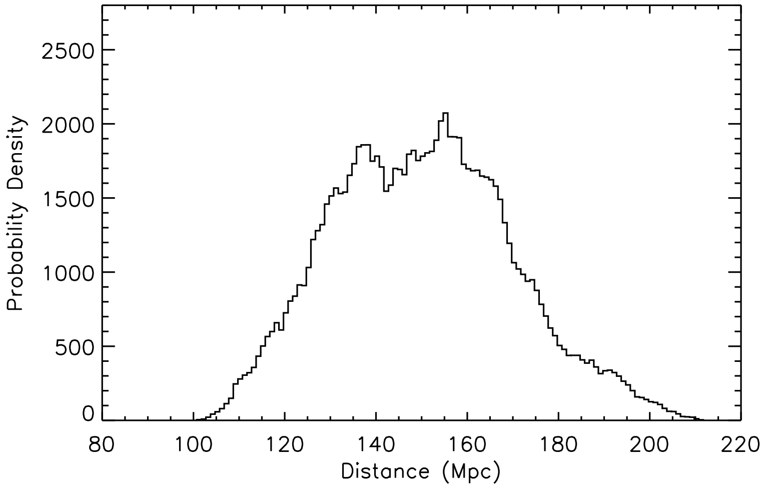

Fig. 5.6.— The probability distribution of the distance to NGC 6264 from the Bayesian fitting program. The x-axis shows the distance in Mpc, and the y-axis shows the relative probability density of the distance. The highest probability occurs at D =154.6 Mpc, and the 68% confidence range centers at 149.2 Mpc with an uncertainty of 19.8 Mpc. The non-Gaussian distribution is the result of the Bayesian analysis without imposing a strong Gaussian prior. This shows the power of the Bayesian approach to explore the real probability distribution of the data.

program gives very accurate measurements on x_0 and v_{sys}. With these values as the constraints in the ensemble-fitting, we obtain a distance of 133.7±15.6 Mpc (11.6%). The corresponding Hubble constant is 75.1±9.0 km s^{-1} Mpc^{-1} (12.0%), consistent with the value from the Bayesian fitting within the 68% uncertainty.

5.2.2 Distance to NGC 6264 by Allowing Eccentric Orbits

With a time-dependent linear theory model of an eccentric disk, Armitage (2008) studies the evolution of a thin initially eccentric disk under conditions appropriate to sub-pc scales in Active Galactic Nuclei. In his model, the evolution of the eccentric disk is controlled by a combination of differential precession driven by the disk potential and propagating eccentricity waves that are damped by viscosity. A

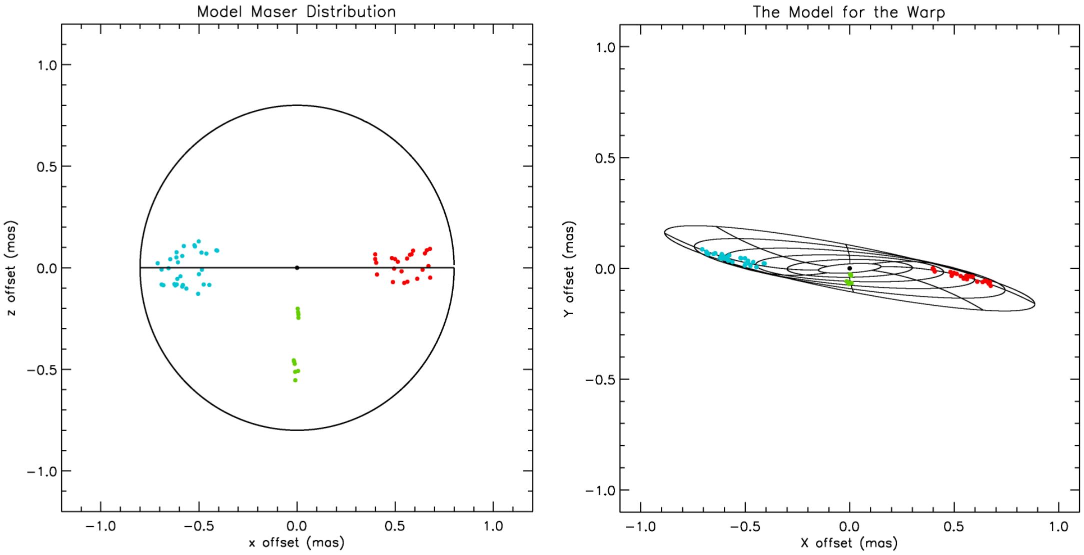

Fig. 5.7.— The left panel shows the model maser distribution in NGC 6264 from the overhead perspective. The right panel shows the best-fit warp from the observer's perspective with model maser spots plotted on top of it. We deliberately decrease the disk inclination by ∼5° to show the degree of disk warping more clearly.

simple estimate yields a circularization timescale of $\tau_{circ} \sim \eta \times 10^7$ (r/0.1 pc)$^{5/6}$ yr, where η is a coefficient of order of unity. Armitage (2008) concludes that while it is plausible that enough time has elapsed for the eccentricity of masing disks to have been substantially damped, it may not be justied to assume vanishing eccentricity. In addition, he predicts that during the damping phase the pericenter of the eccentric orbits describes a moderately tightly wound spiral with radius (see Figure 2 in Armitage (2008)).

To explore the impacts of the eccentricity of the maser orbits on the distance determination for NGC 6264, we turn on the eccentricity parameters including the eccentricity e, the azimuthal angle of the pericenter ϖ_0, and dϖ/dr which describes how ϖ changes with r:

$$\varpi = \varpi_0 + \frac{d\varpi}{dr} r \ . \tag{5.13}$$

For simplicity, we first assume dϖ/dr = 0. This assumption implies that the precession rates of all the orbits in the disk are the same, and the masers follow confocal, aligned Keplerian orbits. Since we do not have any prior information for e and ϖ, we simply use flat priors for these two parameters in the Bayesian fitting. With these priors, we obtain an eccentricity distribution that peaks at e =0.06 (see Figure 5.8). The 68% confidence range of the distribution is 0.04 to 0.17 and the center of this range is 0.10. While the eccentricity is not negligible, its impact on the distance to NGC 6264 is small. The distance we obtain is 152.3±16.2 Mpc, which only changes by 2.1%. Surprisingly, allowing the eccentricity into the fit improves the distance uncertainty from 13.2% to 10.6%. With the best fit v_{sys} (10194.9 km s^{-1})[3], we determine a H_0 to be 65.8±7.2 km s^{-1} Mpc^{-1} (11.0%).

To see whether differential precession suggested by Armitage (2008) would affect the distance measurement, we turn on dϖ/dr in our fitting and adopt a flat prior. We obtain an eccentricity e to be 0.13±0.09, similar to the previous result. We get a pericenter azimuth of $\varpi = 32.8^\circ \pm 27.0^\circ$. The d$\varpi$/dr from the fit is -53.7±31.5 degree/mas. Similar to the previous case, the distance does not change much, but the uncertainty increases by about 40% : D =156.1±22.8 Mpc (14.6%). The corresponding Hubble constant is 64.3±9.6 km s^{-1} Mpc^{-1} (14.9%).

---

[3] This velocity is measured in terms of the optical convention. We apply relativistic corrections to this velocity before calculating the Hubble constant.

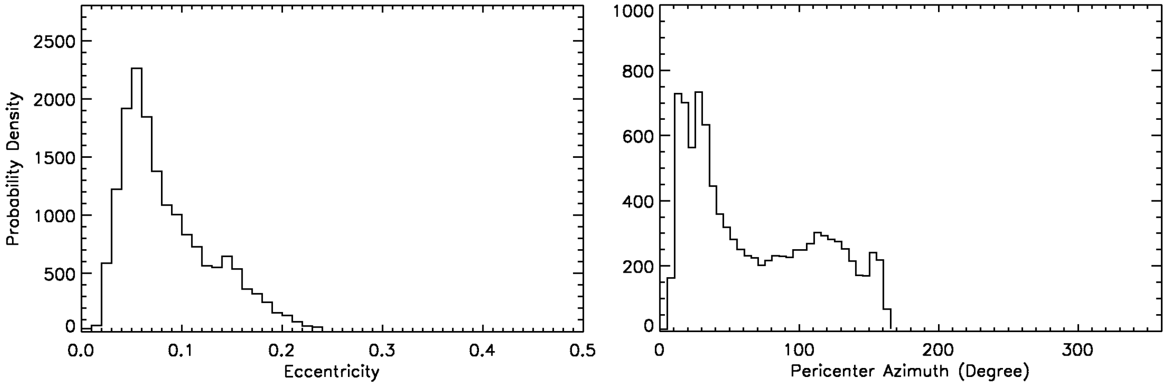

Fig. 5.8.— The left panel shows the probability distribution of the eccentricity of the maser orbits. For the eccentricity distribution, the highest probability occurs at e =0.06. The 68% confidence range of the distribution centers at 0.10 with an uncertainty of 0.06. It is interesting to notice that the probability for the maser orbits to be circular is nearly zero, and the non-vanishing eccentricity may have important implications for how the maser disk formed and evolved with time. The right panel show the probability distribution for the pericenter azimuth. The distribution peaks at $\varpi = 15.3°$, with the 68% confidence range centering at 75.3° (uncertainty=60.0°).

5.3 Systematic errors

In the H_2O megamaser method for distance determination described in Chapter 1, we have two basic assumptions : 1. the masing gas follows circular, Keplerian motion; and 2. the observed accelerations of the masers in the disk are caused by gravity of the central BH. If there are any deviations from these two assumptions for our maser disks, there will be systematic errors in our distance measurements. In the past, the eccentricity of the maser orbits has been the biggest source of systematic uncertainty. Now, with the powerful Bayesian 3-dimensional modeling program which allows eccentric orbits in the modeling, the character of orbital eccentricity has changed from being a systematic to a random uncertainty, and this makes our distance measurement more robust.

There are several other important sources of systematics that could bias our distance measurement. These include non-gravitational acceleration, imperfect model of disk warping, the effect of radiation pressure, finite disk mass, and the hypothesis that the H_2O megamaser as a wave phenomenon. The effect of the finite disk mass has been explored in depth in Herrnstein (2005) and we will not repeat it again here. For the other sources of systematics, since detailed investigations of these sources are beyond the scope of this thesis, we will just mention them briefly here.

5.3.1 Non-gravitational Acceleration

As mentioned in Chapter 1, shocks due to spiral density waves in a maser disk, if they exist, can cause non-gravitational acceleration for the masing gas (Maoz & McKee 1998). In addition, the local gravity of over-dense regions of the spiral waves can also introduce additional acceleration for masing gas in the disk (Humphreys et al. 2008). If these extra accelerations do exist and are not accounted for in the distance determination, there will be additional systematic errors. One may need a good theoretical model for the density waves in the maser disk to estimate the magnitude of the non-gravitational acceleration and understand its impact on the distance measurement.

5.3.2 Disk Warping

Disk warping could introduce an error in the distance determination when the warping model in our fitting is different from how the disk really warps. Currently, we prescribe the warp in terms of Equation (5.10) and (5.11), but this prescription is purely phenomenological and does not have a firm physical basis. In principle, we can explore the effects of an inaccurate warping model in a phenomenological way by applying our Bayesian fitting program to a synthetic dataset in which the warp is simulated based on an entirely different warping model, but the best approach would be to understand the physical mechanism of disk warping better and construct a warp model with a firmer physical basis. In addition to this purely geometrical effect, the disk warping could also introduce a systematic error by changing the dynamics of the masing gas and causing non-circular orbits. However, exploring this possibility would require a deep understanding of the actual warping mechanism for our maser disks, and this needs to be investigated more in the future.

5.3.3 Radiation Pressure

The radiation pressure can be a cause of systematic error when its strength is comparable to the gravitational force of the central BH. When the radiation pressure is significant, the gas will move slower than it would otherwise. If the effect of radiation pressure is not accounted for, one will underestimate the BH mass and distance. However, it would be hard to distinguish the effect of radiation pressure from the gravity of the BH because both forces have $1/\mathrm{r}^2$ dependence. We will need to do some theoretical calculation of the contribution of the radiation pressure on the dynamics of the masing gas with available X-ray data and estimate its impact on the distance measurement.

5.3.4 H_2O Masers as a Wave Phenomenon

Finally, one may suspect that the H_2O maser in an accretion disk is just a *wave phenomenon* in the sense that it does not really trace the orbital motion of the gas in the disk, but just follows the bulk motion of the density waves in the disk. That is, the observed velocities of the masers are group velocities, rather than phase velocities.

If this is true, an H_2O megamaser cannot be used to determine the distance to a galaxy reliably. The strongest counterargument can be found in NGC 4258, where the distance measured based on the accelerations of the masers is in excellent agreement with that based on the proper motions of the masing gas. Such a good agreement is very unlikely if what we observed are just the bulk motions of density waves. However, all other maser galaxies are too distant to measure the proper motion of their systemic masers accurately, and therefore the same argument cannot be applied.

Chapter 6

Conclusion

6.1 The Contributions to the Methodology of the MCP

In the Megamaser Cosmology Project, we bypass the Extragalactic Distance Ladder by using the H_2O megamaser method to measure direct angular-diameter distances to galaxies in the Hubble flow. While this method seems to be well-established with the study of NGC 4258 and thus the path to applying this method to other megamaser disks seems straightforward, we have encountered several new challenges when applying this method to more distant galaxies as the MCP proceeds. The work in this thesis is part of the effort to face these challenges and to develop new methods to make sensitive VLBI imaging and accurate distance determination possible. I illustrate the main contributions of this thesis to the MCP as follows.

The first key contribution of this thesis is the development of a new, simple way to perform VLBI self-calibration , which is important for imaging maser disks sensitively and efficiently. When the MCP first started, in order to correct for the atmosphere phase, we usually needed to rely on phase-referencing or the old-style way of doing self-calibration. After some experiences in applying these methods to the distant megamaser galaxies in the MCP, we found that these two methods have many limitations. The phase-referencing method requires a very close-by ($< 1^\circ$) luminous quasar for phase-calibration, and such quasars are often not available for our maser galaxies. In addition, the phase-referencing technique is not efficient for imaging our distant, faint megamasers, and would require more than 100 hours of VLBI observations to achieve sufficient signal-to-noise for precise distance determination for several of our galaxies. The old-style self-calibration method is $\sim$4 times more efficient than the phase-referencing method in terms of the amount of observing time to achieve a certain signal-to-noise, but requires the maser disk to have lines brighter than $\sim$100 mJy. With the new self-calibration technique developed in this thesis, we have been able to perform self-calibration in megamasers with flux densities of only $\sim$30 mJy. This enabled us to obtain sensitive images for maser disks which are too faint to be imaged efficiently with the traditional ways of phase-calibration.

The second important contribution of the work in this thesis is the thorough investigation of the reliability and accuracy of the methods for acceleration measurements, and an innovation to improve the GLOFIT method (Chapter 4). Reliable and accurate acceleration measurements are an essential part of the distance determination. However, it was unclear at the beginning of this thesis how accurately one could really measure the accelerations in distant, faint megamasers, given the relatively low signal-to-noise and high degree of line-blending. In this thesis, I conducted an extensive investigation on the accuracy and reliability of our acceleration-measuring methods with various kinds of simulated spectra. I found that the current acceleration-measuring methods have limitations under some circumstances that can be common for many megamasers, and thus we need new methods to surpass these limitations. This thesis provides a new way to use the GLOFIT program, and this new approach helped obtain stable solutions for the accelerations which were difficult to measure with the unmodified GLOFIT program.

The third contribution made in this thesis is a new method to measure the distance to a megamaser system when its systemic masers reside at different radii. At the beginning of the MCP, only NGC 4258 had been studied in detail, and the systemic masers in that galaxy all lie in a single orbital ring, leading to a linear trend in the P-V diagram. The linear trend of the systemic features is essential to distance determination because it makes the measurement easy. However, after we study more maser disks in depth, we found that it is not uncommon for the systemic masers in other megamasers to reside in multiple rings, and this makes the original simple method for distance determination difficult to apply. This thesis provides a simple "ensemble" approach to overcome this challenge by using all systemic masers in multiple rings to constrain the distance. This ensemble approach has been successfully for measuring a good distance to NGC 6264, in which the systemic masers reside in at least four different rings. Although this method is less general than the 3-dimensional Bayesian program subsequently written by Mark Reid, it is intuitive, and can provide a consistency check for the result from the Bayesian analysis.

In short, the efforts in this thesis have successfully overcome several new challenges encountered in the MCP. While the process was quite difficult, the new ideas and methods have helped produce fruitful and important scientific results.

6.2 Summary of the Main Scientific Results

For the first time we measure a direct *angular-diameter* distance to a galaxy beyond 100 Mpc in a single step without any local calibration. We apply two different methods to measure the distance to NGC 6264. With an ensemble-fitting method that fits the P-V diagram of the systemic masers with a multi-ring model, we achieve a distance of 150.8±32.8 Mpc (22% accuracy). By using a Bayesian fitting program that fits the maser disk in all three dimensions with a weak Gaussian prior on H_0 (50 km s^{-1} Mpc^{-1}< H_0 < 100 km s^{-1} Mpc^{-1} with 68% probability) to constrain the distance in the fitting, we obtain a distance of 149.2±19.8 Mpc (13.2%), with the corresponding H_0 of 67.3±9.1 km s^{-1} Mpc^{-1}.

We explore the impact of eccentricity on distance determination by applying the Bayesian-fitting program to the maser disk in NGC 6264 with eccentricity (e) and pericenter azimuth as free parameters (i.e. flat priors). We found that the eccentricity distribution peaks at 0.06 with nearly zero probability for $e = 0.0$, and this suggests that it is likely that the maser disk is eccentric. Nonetheless, the orbital eccentricity has only a negligible impact on the distance, and amazingly improves the accuracy from 13.2% to 10.6% (D =152.3±16.2 Mpc) when using the weak prior on H_0.

The current uncertainty in the distance to NGC 6264 is dominated by statistical error. Therefore, we could improve the distance accuracy with more observations in the future. It is possible that we can reduce the uncertainty from 10.6% to ∼8% by taking four more tracks of VLBI observations on this galaxy. While there is still room to improve the distance accuracy, given the fact that this galaxy is ∼20 times more distant and ∼60 times fainter than NGC 4258, the ∼11% distance to a galaxy beyond 100 Mpc is already an unprecedented result.

In this thesis, I also present a VLBI map of the megamaser disk in NGC 6323.

This map is derived from 13 tracks of VLBI observations (∼150 hours) that included the VLBA, the GBT, and the Effelsberg telescope, making it the most sensitive VLBI map ever observed for an H_2O megamaser. Although we have an exquisitely sensitive map, we do not obtain a comparably precise measurement of the distance to NGC 6323 because the extremely low flux densities of the systemic masers prevent us from measure accurate accelerations for many maser spots, and the maser disk is oriented in the direction in the sky where the angular resolution is the poorest.

With the Keplerian rotation curves of six megamaser galaxies (NGC 1194, NGC 2273, NGC 2960 (Mrk 1419), NGC 4388, NGC 6264 and NGC 6323), plus a seventh previously published, we determine accurate enclosed (presumably BH) masses within the central ~ 0.3 pc of these galaxies. The maser distributions in all seven megamaser galaxies are consistent with edge-on circumnuclear disks surrounding central massive objects in the active galactic nuclei. The inner radii of the disks are between 0.09 and 0.5 pc, similar to all previously published megamaser disks. Four of the megamaser disks reveal evidence for warps. The high central mass densities (0.12 to 60 $\times 10^{10} M_\odot$ pc^{-3}) (within the central ∼0.3 pc) of the seven megamaser disks indicate that in all except two maser disks, the central mass is dominated by a supermassive BH rather than an extremely dense cluster of stars or stellar remnants.

The BH masses measured are all within a factor of 3 of $2.2 \times 10^7 M_\odot$ and the accuracy of each BH mass is primarily limited by the accuracy of the Hubble constant. The narrow range of BH mass distribution mirrors selection from the local active-galaxy BH mass function. The accurate BH masses in the seven megamaser galaxies contribute to the observational basis for testing the $M - \sigma_\star$ relation at the low-mass end. The deviation of the $M - \sigma_\star$ relation defined mainly by large, elliptical galaxies from the mean relation of the several accurate maser BH masses suggests that the

$M - \sigma_\star$ relation may not be a single, low-scatter power law as originally proposed, which has interesting implications for the universality of the $M - \sigma_\star$ relation (Greene et al. 2010). MCP observations continue and we expect to obtain more maser BH masses in the future.

Appendix A Applying The Virial Estimation Method to Megamaser Galaxies

The virial estimation method for measuring BH masses in AGNs (e.g. Greene & Ho 2006; Kim et al. 2008; Vestergaard & Osmer 2009) uses the broad-line region (BLR) gas as a dynamical tracer. It is usually applied only to Type 1 AGNs, where the BLRs can be observed directly. In this method, one estimates the BH mass with the following equation:

$$M_\bullet = \frac{f R_{\rm BLR} \sigma_{\rm line}^2}{G} \ , \tag{A.1}$$

where f, $R_{\rm BLR}$, and $\sigma_{\rm line}$ have been defined in section 3.5. Since one can directly detect light from the BLRs in Type 1 AGNs, $\sigma_{\rm line}$ can be measured from the broad line spectra and one can use the continuum luminosity $\lambda L_\lambda(5100\mathring{A})$ to estimate $R_{\rm BLR}$ via the $\lambda L_\lambda(5100\mathring{A}) - R_{\rm BLR}$ correlation (e.g. Kaspi et al. 2000 & 2005).

In a Type 2 AGN, including the megamaser galaxies we study here, our line-of-sight to the BLR is blocked by heavy dust extinction, so one cannot directly measure $\lambda L_\lambda(5100\mathring{A})$ and $\sigma_{\rm line}$. Instead, one can probe the BLRs in megamaser galaxies with polarized scattered light and hard X-rays. Among all the megamaser galaxies with measured BH masses, polarized scattered light from the BLRs has been detected in NGC 1068, NGC 4388, NGC 2273, and Circinus (see Table 3.6), and X-ray measurements are also available for these four galaxies.

We can estimate $\sigma_{\rm line}$ from the relation $\sigma_{\rm line}/V_{\rm FWHM} = 2.09 \pm 0.45$ from Woo et al. (111), where $V_{\rm FWHM}$ is the FWHM width of polarized scattered light in the broad H_α line (NGC 2273, NGC 4388, and Circinus) or H_β line (NGC 1068). The major concern with these linewidths is that the observed values may not be the same as the linewidth one would measure if the BLRs could be observed directly. We identify two effects that can induce such a difference from the well-studied case NGC 1068 (74). First, the broad H_β lines in the polarized flux spectra can contain a contribution from the narrow H_β lines. Without completely removing the contribution from narrow lines, the BLR linewidth may be underestimated by ∼20-30% in NGC 1068. Second, the polarized emission from AGNs may originate from light being scattered by electrons with a temperature a few times 10^5 K, which results in significant thermal broadening (∼50%) of the spectral lines. Because of these two effects, there will be systematic errors in $\sigma_{\rm line}$ if one directly uses the observed linewidth of the polarized lines to estimate $\sigma_{\rm line}$. Among the four megamaser galaxies we consider here, only NGC 1068 has been studied in enough detail to correct for these two effects. Luckily, the two effects change the linewidth in opposite directions, and hence could offset each other to a certain extent. In NGC 1068, if no correction is made for these two effects, the systematic error will be only ∼10%, just slightly larger than the measurement error. Without knowing the actual contributions of these two effects for the other three galaxies, we assume that the two effects cancel each other to the same extent as in NGC 1068 and use the observed linewidths as the approximations for the intrinsic widths.

In this work, $R_{\rm BLR}$ was estimated from the “intrinsic” $L_{(2-10{\rm keV})}$ of the nuclear region via the $L_{(2-10{\rm keV})} - R_{\rm BLR}$ correlation (54). Since three (NGC 1068, NGC 2273, and Circinus) of the four megamaser galaxies considered here are Compton-thick (i.e.

the X-ray absorbing column density is $> 10^{24}$ cm^{-2}), we paid particular attention to how the $L_{(2-10\mathrm{keV})}$ were measured. The Compton thick nature of these AGNs is a problem because the intrinsic radiation is mostly suppressed and the X-ray spectrum is dominated by the reflected or scattered components. It is difficult to measure the actual absorbing column density and it is very likely that the intrinsic hard X-ray luminosity is severely underestimated, e.g. Levenson et al. (64); Bassani et al. (7). Therefore, we excluded those measurements that did not consider the Compton-thick nature of these sources and failed to give the absorbing column density in the expected range. We mainly considered those measurements from either data with appropriate modeling or from observations with instruments capable of directly measuring the transmission components of X-ray above 10 keV. We took at least two different measurements for each galaxy from the literature and used the average value to calculate R$_{BLR}$ from the correlation in Kaspi et al. (54).

Given R_{BLR} and σ_{line}, we estimated the BH masses using Equation A1 with the empirically determined $\langle f \rangle = 5.2^{+1.3}_{-1.3}$ from Woo et al. (111). The resultant BH masses were compared with the maser BH masses in section 5.

References

[1] Akylas, A., Georgantopoulos, I. 2009, A&A, 500, 999

[2] Argon, A. L., Greenhill, L. J., Reid, M. J., Moran, J. M., Humphreys, E. M. L. 2007, ApJ, 659, 1040

[3] Armitage, P. J. 2008, arXiv:0802.1524

[4] Awaki H., Terashima Y., Higaki Y., Fukazawa Y. 2009, PASJ, 61, 317

[5] Barth, A. J.; Sarzi, M.; Rix, H.-W.; Ho, L. C.; Filippenko, A. V.; Sargent, W. L. W. 2001, ApJ, 555, 685

[6] Barth, A. J. Carnegie Observatories Astrophysics Series, Vol. 1: Coevolution of Black Holes and Galaxies, 2003 ed. L. C. Ho (Pasadena: Carnegie Observatories)

[7] Bassani L., Dadina M., Maiolino R., Salvati M., Risaliti G., Della Ceca R., Matt G., Zamorani G. 1999, ApJS, 121, 473

[8] Beers, T. C.; Kriessler, J. R.; Bird, C. M.; Huchra, J. P. 1995, AJ, 109, 874B

[9] Binney, J., & Tremaine, S. 2008, "Galactic Dynamics" (Princeton University Press)

[10] Blandford, R. D.; McKee, C. F. 1982, ApJ, 255, 419

[14] Braatz, J. A., Reid, M. J., Humphreys, E. M. L., Henkel, C., Condon, J. J., & Lo, K. Y. 2010, ApJ, 718, 657

[12] Braatz, J. A.; Gugliucci, N. E. 2008, ApJ, 678, 96

[13] Braatz, J., Condon, J., Reid, M., Henkel, C., Lo, K. Y., Kuo, C. Y., Impellizzeri, C., Hao, L. The Megamaser Cosmology Project Large Proposal, submitted to NRAO June 1, 2009

[14] Braatz, J. A.; Reid, M. J.; Humphreys, E. M. L.; Henkel, C.; Condon, J. J.; Lo, K. Y. 2010, ApJ, 718, 657

[15] Braatz et al. 2011, in prep.

[16] Cappi M. et al. 2006, A&A, 446, 459

[17] Carroll SM, Duvvuri V, Trodden M, Turner MS. 2004. Phys. Rev. D 70:043528

[18] Chabrier, G., & Baraffe, I. 2000, ARA&A, 38, 337

[19] Chib, S., Greenberg, E. 1995, The American Statistician, Vol. 49, No. 4

[20] Cretton, N.; van den Bosch, F. C. 1999, ApJ, 514, 704

[21] Croton, D. J. et al. 2006, MNRAS, 365, 11

[22] Deffayet C. 2001. Phys. Lett. B502:199

[23] Dvali G. R., Gabadadze G., Porrati M. 2000 Phys. Lett. B485:208

[24] Forster K., Leighly K. M., Kay L. E. 1999, ApJ, 523, 521

[25] Ferrarese, L. & Merritt, D. 2000, ApJ, 539, 9

[26] Ferrarese, L., Ford, H. 2005 SSRv 116 523

[27] Freedman, W. L. et al. 2001, ApJ, 553, 47

[28] Freedman, W. L.; Madore, Barry F. 2010, ARA&A, 48, 673

[29] Frieman, J. A., Turner, M. S., Huterer, D. 2008, ARA&A, 46, 385

[30] Gebhardt, K. et al. 2000, AJ, 119, 1157

[31] Gebhardt, K. et al. 2000, ApJ, 539, 13

[32] Gebhardt, K. et al. 2003, ApJ, 583, 92

[33] Green, J. E., Ho, L. C. 2006, ApJ, 641, 21

[34] Gebhardt K.; Thomas J. 2009, ApJ, 700, 1690

[35] Geyer, C. J. 1992 Practical Markov chain Monte Carlo, Statistical Science 7, 473

[36] Markov Chain Monte Carlo in Practice (Chapman & Hall/CRC Interdisciplinary Statistics)

[37] Greene, J. E., Peng, C. Y., Kim M., Kuo, C.-Y., Braatz J. A.,Impellizzeri, C. M. V., Condon, J.,Lo, F., Henkel C. 2010, ApJ, in press

[38] Greenhill, L. J.; Moran, J. M.; Reid, M. J.; Menten, K. M.; Hirabayashi, H. 1993, ApJ, 406, 482

[39] Greenhill,L.J., Gwinn,C.R., Antonucci,R., Barvainis,R. 1996, ApJ, 472, 21

[40] Greenhill, L. J., Moran, J. M., Herrnstein, J. R. 1997, ApJ, 481, 23

[41] Greenhill,L.J. et al. 2003, ApJ, 590, 162

[42] Gültekin, K. et al. 2009, ApJ, 698, 198

[43] Heckman T. M., Kauffmann G., Brinchmann J., Charlot S., Tremonti C., White S. D. M. 2004, ApJ, 613, 109

[44] Henkel, C.; Braatz, J. A.; Greenhill, L. J.; Wilson, A. S. 2002, A&A, 394, 23

[45] Herrnstein, J. R., Moran, J. M., Greenhill, L. J., Diamond, P. J., Inoue, M., Nakai, N., Miyoshi, M., Henkel, C., Riess, A. 1999, Nature, 400, 539

[46] Herrnstein, J. R.; Moran, J. M.; Greenhill, L. J.; Trotter, Adam S. 2005, ApJ, 629, 719

[47] Ho L. C., Filippenko A. V., Sargent W. L. W., and Peng C. Y. 1997, ApJS, 112, 391

[48] Hu, W., Fukugita, M., Zaldarriaga, M., & Tegmark, M. 2001, ApJ, 549, 669

[49] Hu, W. 2005, ASPC, 339, 215

[50] astings, W. K. 1970, Monte Carlo sampling methods using Markov chains and their applications. Biometrika. 57, 97-109.

[51] Humphrey, P. J., Buote, D. A., Brighenti, F., Gebhardt, K., Mathews, W. G. 2009, ApJ, 703, 1257

[52] Humphreys, E. M. L., Reid, M. J., Greenhill, L. J., Moran, J. M., Argon A. L. 2008, ApJ, 672, 800

[53] Kaspi, S., Smith, P. S., Netzer, H., Maoz, D., Jannuzi, B. T., Giveon, U. 2000, ApJ, 533, 631

[54] Kaspi, S., Maoz, D., Netzer, H., Peterson, B. M., Vestergaard, M., Jannuzi, B. T. 2005, ApJ, 629, 61

[55] Kim, M., Ho, L. C., Peng, C. Y., Barth, A. J., Im, M., Martini, P., Nelson C. H. 2008, ApJ, 687, 767

[56] Kondratko,P.T., Greenhill,L.J., Moran,J.M. 2005, ApJ, 618, 618

[57] Kondratko,P.T., Greenhill,L.J., Moran,J.M. 2008, ApJ, 678, 87

[58] Kormendy J., Cargnegie Observatories Astrophysics Series, Vol. 1: Coevolution of Black Holes and Galaxies ed. L. C. Ho (Cambridge: Cambridge Univ. Press

[59] Kormendy, J., Gebhardt, K. 2001, AIPC, 586, 363

[60] Kormendy, J. 2004, cbhg.symp, 1

[61] Kormendy, J., Richstone, D. 1995, ARA&A, 33, 581

[62] Kukula, M. J., Pedlar, A., Baum, S. A., O'Dea, C. P. 1995, MNRAS, 276, 1262

[63] Kuo, C. Y., Braatz, J. A., Condon, J. J., Impellizzeri, C. M. V., Lo, K. Y., Zaw, I., Schenker, M., Henkel, C., Reid, M. J., Greene, J. E. 2011, ApJ, 727, 20

[64] Levenson N. A., Heckman T. M., Krolik J. H., Weaver K. A., Życki P. T. 2006, ApJ, 648, 111

[65] Lo, K. Y. 2005 ARA&A 43 625

[66] Lodato G., Bertin G. 2003, A&A, 398, 517

[67] Lu, N. Y., Hoffman G. L., Groff T., Roos T., Lamphier C. 1993, ApJS, 88, 383

[68] Magorrian, J.; Tremaine, S.; Richstone, D.; Bender, R.; Bower, G.; Dressler, A.; Faber, S. M.; Gebhardt, K.; Green, R.; Grillmair, C.; Kormendy, J.; Lauer T. 1998, AJ, 115, 2285

[69] Maoz, E. 1995, ApJ, 455, 131

[70] Maoz, E. 1998, ApJ, 494, 181

[71] Mamyoda, K., Nakai, N., Yamauchi, A., Diamond, P., Huré, J.-M. 2009, PASJ, 61, 1143

[72] Matt, G. et al. 1999, A&A, 341, 39

[73] etropolis, N., Rosenbluth, A.W., Rosenbluth, M.N., Teller, A.H. & Teller, E. (1953). Equations of state calculations by fast computing machines. J. Chem. Phys. 21, 1087-92.

[74] Miller J. S., Goodrich R. W., Mathews W. G. 1991, ApJ, 378, 47

[75] Mioduszewski, A., Kogan, L. 2000, AIPS Memo 110, http://www.aips.nrao.edu/aipsmemo.html

[76] Moran, E. C., Barth, A. J., Kay, L. E., Filippenko, A. V. 2000, ApJ, 540, 73

[77] Miyoshi, M.; Moran, J.; Herrnstein, J.; Greenhill, L.; Nakai, N.; Diamond, P.; Inoue, M. 1995, Nature, 373, 127

[78] Netzer, H. 1990 in Active Galactic Nuclei, ed. T. J.-L. Courvoisier and M. Major (Berlin, Springer), 57

[79] Ogle P. M., Brookings T., Canizares C. R., Lee J. C., Marshall H. L. 2003, A&A, 402, 849

[80] Oliva1 E., Marconi A., Cimatti A., and di Serego Alighieri S. 1998, A&A, 329, 21

[81] Onken, C. A., Ferrarese, L., Merritt, D., Peterson, B. M., Pogge, R. W., Vestergaard, M., Wandel, A. 2004, ApJ, 615, 645

[82] Page, L. et al. 2003, ApJS, 148, 233

[83] Perlmutter et al. 1999, ApJ, 517, 565

[84] Peterson, B. M. et al. 2004, ApJ, 613, 682

[85] Plummer, H. C. 1915, MNRAS, 76, 107

[86] Reid,M.J., Braatz,J.A., Condon,J.J., Greenhill,L.J., Henkel,C., Lo,K.Y. 2009, ApJ, 695, 287

[87] Reid, M. J., Menten, K. M., Brunthaler, A., Zheng, X. W., Moscadelli, L. & Xu, Y. 2009, ApJ, 693, 397

[88] Riess et al. 1998, AJ, 116, 1009

[89] Riess, A. G.; Macri, L.; Casertano, S.; Sosey, M.; Lampeitl, H.; Ferguson, H. C.; Filippenko, A. V.; Jha, S. W.; Li, W.; Chornock, R.; Sarkar, D. 2009, ApJ, 699, 539

[90] Riess, A. G.; Macri, L.; Casertano, S.; Lampeitl, H.; Ferguson, H. C.; Filippenko, A. V.; Jha, S. W.; Li, W.; Chornock, R. 2011, ApJ, 730, 119

[91] Richstone, D. et al. 1998, Nature, 395, A14

[92] Roberts, G. O., Gelman, A., & Gilks, W. R. 1997, Ann. Appl. Probab. Vol. 7, No. 1, 110

[93] Russell, D. G. 2002, ApJ, 565, 681

[94] Sandage, A. R. 1961, ApJ, 133, 355

[95] Sandage, A. R. 1970, Phys. Today, Vol. 23, No. 2, p. 34 - 41

[96] Sandage, A., Tammann, G. A., Saha, A., Reindl, B., Macchetto, F. D., Panagia, N. 2006, ApJ, 653, 843

[97] Sargent, W. L. W.; Young, P. J.; Lynds, C. R.; Boksenberg, A.; Shortridge, K.; Hartwick, F. D. A. 1978, ApJ, 221, 731

[98] Sarzi, M.; Rix, H.; Shields, J. C.; Rudnick, G.; Ho, L. C.; McIntosh, D. H.; Filippenko, A. V.; Sargent, W. L. W. 2001, ApJ, 550, 65

[99] Siopis, C. et al. 2009, ApJ, 693, 946

[100] Smith D. A. & Wilson A. S. 2001, ApJ, 557, 180

[101] Song Y. S., Hu W., Sawichi I. 2007, Phys. Rev. D 75:044004

[102] Terashima Y., Iyomoto N., Ho L. C., Ptak A. F. 2002 ApJS 139 1

[103] Tonry, J. L. 1984, ApJ, 283, 27

[104] van den Bosch, R. C. E. & de Zeeuw, P. T. 2010, MNRAS, 401, 1770

[105] van der Marel R. P. 1994, ApJ, 432, 91

[106] van der Marel R. R.; Cretton, N.; de Zeeuw, P. T.; Rix, H.-W. 1998, ApJ, 493, 613

[107] Vestergaard, M. 2009 arXiv0904.2615

[108] Vestergaard, M., Osmer, P. S. 2009, ApJ, 699, 800

[109] Walker, C. & Chatterjee, S., 2000, VLBA Scientific Memo 23, http://www.vlba.nrao.edu/memos/sci/

[110] Weinberg, S. 1987 Phys. Rev. Lett. 59: 26072610

[111] Woo, J.-H. et al. 2010, ApJ, 716, 269

[112] Young, P. J.; Westphal, J. A.; Kristian, J.; Wilson, C. P.; Landauer, F. P. 1978, ApJ, 221, 721

[113] Yang, Y., Wilson, A. S., Matt, G., Terashima, Y., Greenhill, L. J. 2009, ApJ, 691, 131